Study on Diamond Detector to Develop Its Numerical Model and Charge Amplification Structure

Dissertation

For Doctoral Program

Department of Particle and Nuclear Physics

School of High Energy Accelerator Science

The Graduate University for Advanced Studies (SOKENDAI)

M. Jauhar Kholili

Tsukuba 2019

Acknowledgements

During my doctoral program, I receive supervisions, supports, and helps from many people. I want to express my sincere gratitude to all of them.

The first, I would like to thank my supervisor, Prof. Manobu Tanaka who relentlessly and patiently teaches me about many new knowledges that I need to comprehend for my research works. Prof. Tanaka guidance started even before my doctoral program start, to decide my doctoral research topic and also to find financial support. Without his advice and support, this research work would not even be started. Thank you very much Tanaka-sensei.

The second, I want to express my gratitude to my colleagues in KEK and collaborators from other institutions who gave me support and advices that are really useful for my research work. I want to thank to Asuka Hara-san who taught me a lot about the experiment methods while dealing with diamond crystal characterization. I also want to thank to Ryutaro Hamasaki-san who gave precious guidance about Sentaurus TCAD simulation in the beginning stage of my research work. I also want to thank to Masayoshi Shoji-san who gave many supports especially if I had problems with the electronic test board. I also want to thank to Prof. Masaya Miyahara who teched me about the design of CMOS amplifier. I want to thank to our collaborators Prof. Satoshi Koizumi and Takehiro Shimaoka-san from Diamond group in NIMS Tsukuba who gave me precious advices and suggestions to understand the characteristic of diamond crystal and its metal contact. I also want to thank to Prof. Masayuki Hagiwara who lent me his excellent diamond detector to be evaluated, therefore the mesurement results completed my data set of diamond characteristic evaluation. I also want to give my gratitude to the member of board committee for my doctoral thesis, Prof. Toshiya Sanami and Prof. Satoshi Mihara who gave advice for revising my dissertation and research work. I want to thank to all other colleagues whom I cannot mention one by one from Electronic System (ESYS) group in KEK for the supports during the period of my doctoral degree.

The third, I want to thank the secretary of our ESYS group, Moiyoko Ushioda-san, who helps me a lot when dealing with documents. I also want to thank all administration staffs of KEK-SOKENDAI office who also gave me support in the administrations-related matters. I also want to thank the supportive staffs in KEK user office who helped dealing with the

List of Presentations

Some parts of this thesis were presented in the listed conferences and workshops below.

I. M.J. Kholili, Takehiro Shimaoka, Asuka Hara[A,B], Tetsuichi Kishishita[B], Satoshi Koizumi[D], Aboulaye Traoré[D], Toshiharu Makino[C], Satoshi Yamazaki[C], Yuki Fujii[B], Hajime Nishiguchi[B], Manobu Tanaka, **"New Type of Diamond Particle Detector"**. JPS Autumn Meeting, Utsunomiya University, Utsunomiya, Japan Sept 12 - 15, 2017.

II. M. J. Kholili, **"New Type of Diamond Particle Detector TCAD Simulation"**. ISRD 2018. High Energy Accelerator Research Organization (KEK), Tsukuba, Japan, Jan 23-26, 2018.

III. M. J. Kholili, A. Hara, B, T. Shimaoka, T. Kishishita, S. Koizumi, A. Traoré, T. Makino, S. Yamasaki, Y. Fujii, H. Nishiguchi, M. M. Tanaka, **"Comparison of Experimental Data and TCAD Simulation of Diamond-Based Particle Detector and Proposal of 3D-Contact Diamond Detector"**, JPS Autumn Meeting. Shinshu University, Matsumoto, Japan, Sept 14-17, 2018.

IV. M. J. Kholili, A. Hara, T. Shimaoka, S, Koizumi, M. Shoji, M. M.Tanaka. **"Transient-Current Technique Characterization of Diamond Detector and Proposal of Signal Amplification in Diamond"**. EMRS Fall Meeting, Warsaw University of Technology, Warsaw, Poland. Sept 16-19, 2019

Table of Content

Chapter 1

Introduction

1.1 Motivation

The plan to upgrade the luminosity of future high-luminosity (HL) and high-energy (HE) colliders will require an inner-tracking detector system that withstands flows of particles with fluence $\geq 10^{16}$ /cm^2 [Bru07, Mos05, Vel08]. Currently, silicon detector is the selected material that installed as detector system at Inner Tracking System (ITS) in the major large particle detector facilities. Silicon is material of choice because the technology is widely used in other popular applications, therefore it is considered a proven technology.

Under the HL-HE condition, a radiation-hard detector material with faster response is required. Charge mobility of silicon is indeed not the best among semiconductor material. Thus, room of improvement is available to select better detector material with a higher carrier mobility. Another problem will also occur due to the large energy deposition in that heavily irradiated environment. Silicon detector shows high dark current and low charge collection efficiency in a heavily irradiated environment [Bru07]. Hence, the current silicon detector technology cannot endure a long-term operation in future detector system. Silicon performance is also sensitive to the temperature variation. In HL-HE condition, silicon detector system requires a thermal management system to maintain its temperature to perform optimally. Compared to silicon, prior study indicates wide-gap semiconductor, especially diamond [Bru07], give advantages of good radiation hardness and a low dark current under a high fluence condition at room temperature.

A large particle detection system has multilayer detectors with different material to precisely detect specific type of particle. However, certain particles are created in the innermost of detector system, but dedicated detectors for them are located at outer layers of detector system. Thus, improvement of detection precision can be achieved by minimizing the total mass of inner tracking detector system to reduce multiple scattering between those particles and the extensive material of detector system. Therefore, introducing a better material that has better thermal conductance and performs better at high temperature, the extra material for the cooling system can be reduced.

Generally, diamond is excellent material to be detector in high-energy physics application. However, it has significant drawback of low signal generation compare to that of silicon. In order to resolve the problem, understanding the main properties of diamond is indispensable to develop new type of diamond particle detector. Unfortunately, there is no a comprehensive model that is capable to explain the complete experimental data related to charge-carrier transport mechanism with a set of parameters in a single model. Therefore, evaluating of the characteristic is desired for high-quality diamond crystal. A set of parameters in a model should be extracted from experimental data. The methods to extracting the parameters is shown in figure 1-1. With the knowledge of the parameters and the high field breakdown characteristic, a diamond detector that capable to generate Carrier Multiplication Effect (CME) can be designed. The realization of diamond detector with CME can overcome the problem of low amplitude signal of diamond detector.
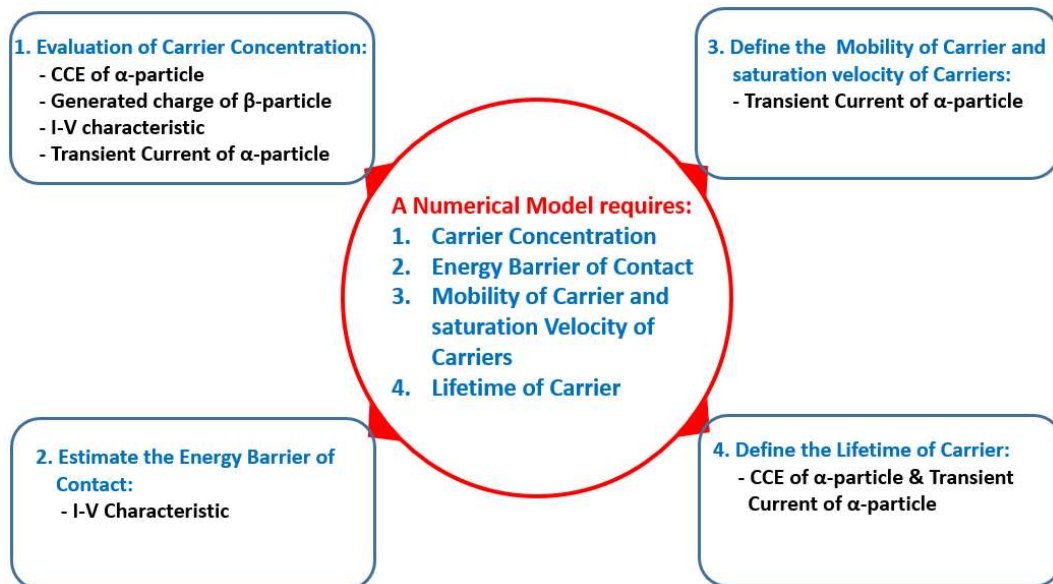
Figure 1-1 The important parameters to built a model for diamond detector and the related experiments.

In order to develop comprehensive model for diamond detector, the references about prior evaluation about diamond detector need to be studied. However, such references are very limited. Only three authors evaluate diamond for particle detector application, they are Pernegger in 2005 [Per05], Pomorski in 2005 [Pom05] and Kasel in 2016 [Kas16]. Fortunately, other branch of electronic technology also starts to study the substitution of the widely used silicon material to widegap material for some applications. The most common development is application of diamond for diode for high power switch [Ras06, Bre07, Naw13]. The

development also helps to boost the improvement of fabrication process that eventually makes high quality substrates of diamond available. Furthermore, some prior works also report the availability of high-quality diamond crystal which can be used to detect particle with an excellent ($\approx$100%) Charge Collection Efficiency (CCE) [Pom05, Vel08, Kas16, Shi18].

Beside the detector, another aspect of detection particle system is the front-end electronic. To detect signal from particle with high count rate, a fast read-out system is required. The commercially available fast amplifiers are not suitable due to high power consumption. In a multichannel detector system, high power consumption is closely related to excessive thermal dissipation that also affect the performance of the detector system. Therefore, designing a new fast amplifier with cutting edge technology is desired for the shake of energy efficiency and to avoid the thermal management problem. For that purpose, an Application-Specific Integrated Circuit (ASIC) amplifier with a new design is realized in a 65 nm Taiwan Semiconductor Manufacturing Company (TSMC) Complementary Metal Oxide Semiconductor (CMOS) technology.

1.2 Contribution of this Work

The main contribution of this research is a comprehensive study of the Metal-Intrinsic-Metal (MIM) diamond device by characterizing diamond detector and constructing a model that is capable to reproduce the characterized data. The characterizations include measurement of I-V, C-V, Charge Collection efficiency (CCE), the depth of depletion layer and transient signal measurement. By those measurements, sufficient information is obtained about main characteristics and parameters of diamond bulk.

Utilizing the parameters, a solid model is constructed based on experimental data. The model is used to study a possible design to improve the performance of diamond detector. For the viewpoint of signal magnitude, diamond performance is worse than that of silicon detector. One of the most promising method to improve the performance of diamond detector is carrier amplification. Due to a high electric field breakdown point of diamond, a new diamond detector design is proposed to overcome the main drawback of diamond detector.

Previous works that develops a model for diamond device do not discuss comprehensively about all of their applied parameters. The first problem is the vague definition of carrier concentration. Brezeanu [Bre07], Rashid [Ras08] and Morozzi [Mor16] define the intrinsic carrier concentration (n_h) of 10^{11} /cm^3 due a practical reason of easier numerical calculation

compared to application of lower carrier concentration. The second problem is the overestimation of carrier mobility for intrinsic crystal. The applied carrier mobility value at room temperature in Brezeanu, Rashid, Morozzi and Nawawi [Naw13] model is 4500 cm^2/V.s and 3800 cm^2/V.s for electron and holes, respectively. These reports cite the carrier mobility values reported in a paper [Isb02] which the values can be reproduced by more recent data by Time-of-Flight (TOF) or Hall-Effect measurement [Pom05, Nes08, Gab10, Per10].

This study is the first, to the best of author knowledge, report comprehensive study about the main parameters of diamond detector that also include the construction of a numerical model. All of the important numerical parameters are based on the measurements to the existing device. Therefore, the values of those parameters are relevant with the present diamond crystal and experimental setup.

The author successfully designs and evaluates a multi-channels fast Transimpedance Amplifier (TIA) based on Flipped Voltage Follower (FVF) configuration for frond-end read-out electronic of diamond detector. The design is implemented in the form of ASIC amplifier based on the cutting-edge technology of the 65 nm CMOS transistor. Unlike the commercially available fast amplifiers for diamond, the TIA amplifier has power consumption of 7.2 mW. This power consumption is two orders of magnitude lower than those of commercially available fast amplifier. The TIA amplifier also has a wide dynamic range up to ±40 fC with a reasonable noise level. The simulation shows that TIA is a fast amplifier with a wide bandwidth of 2.7 GHz and large transimpedance gain. The evaluation of the TIA test-board confirms the excellent transimpedance-gain and excellent maximum conversion-gain of 79.6 dBΩ and 8.4 mV/fC, respectively.

1.3 Organization of Thesis

This thesis has seven chapters. Chapter 1 contains the motivation of conducting a research on building a simulation model for diamond detector and designing a fast amplifier for diamond detector, contribution of this work and the organization of this thesis.

Chapter 2 explains about the advantage of using diamond as a particle detector, the structure of the detector and the fabrication of the diamond sample. The properties of diamond give advantages for building next generation of detector due to a better charge carrier mobility, more radiation hard and higher electric field breakdown point than those of silicon detector. Samples

used for developing the simulation model is MIM structure. To grow the high quality single crystalline diamond, the Chemical Vapor Deposition (CVD) is employed as the deposition method. On the other hand, metal contacts are fabricated either by resistive thermal deposition method or electron beam vapor deposition method.

The methodology for conducting this research is discussed in chapter 3. Simulation method by using Technology Computer-Aided Design (TCAD) is the tool to evaluate the properties of diamond sample. On the other hand, to design a fast current-amplifier an Electronic Computer-Aided Design (ECAD) is utilized. The simulation results are validated by realization of the sample design and evaluation the performance in laboratory.

A detail characterization setup for diamond detector and discussion on the characterization results are explained in chapter 4. The chapter explains the setup for measuring I-V characteristic, CCE and fast transient current from particle detection. The measurement results are utilized to extract the important parameters of diamond crystal.

In chapter 5, the parameters extracted from chapter 4 are applied in TCAD simulation. The experimental data are compared to the simulation results. The I-V characteristic data, CCE and transient from the simulation is evaluated. By application of suitable physical and mathematical model in simulation, the experimental data are reproduced successfully.

Chapter 6 contains a discussion about a new structure of diamond detector. A significant drawback of selecting diamond detector upon silicon detector is a lower signal amplitude. Due to high electric field breakdown point in diamond, the multiplication effect is a possible option to improve the signal performance. The diamond with small needle-like structure is evaluated by simulation to improve the electric field in the diamond detector. The high electric field confinement in small dimension needle-like structure is expected to generate the multiplication effect.

Discussion about a new design of a fast amplifier for diamond detector is the content of chapter 7. The amplifier is categorized as Transimpedance Amplifier (TIA). The motivation of selecting the Common-Gate design upon Common-Source design for input part of the amplifier is explained in detail. The performance of amplifier is evaluated by simulation with Spectre simulation by Candence. The performance of the test board of the amplifier is compared to the prediction of the simulation.

Finally, the last part is the conclusion of this thesis.

Chapter 2

Diamond Particle Detector and Its Preparation

2.1. Introduction

Interaction of charged particles with the detector material is occurred due to the Coulomb forces. The particle influences the electrons within the absorber atoms, so that if the energy is sufficient, the charged particle allows a valence electron free from the atom. The pair of the excited electron and the positively-charge atom is called electron-hole (ehp) as shown in figure 2-1. The process is the basic principle of detector operation when the removed electrons can be drift to the electrode and detected by an electronic system [Kno00]. The main characteristic of the detector material and the design of the detector determine the performance of the detector to produce high resolution signal and high counting efficiency.
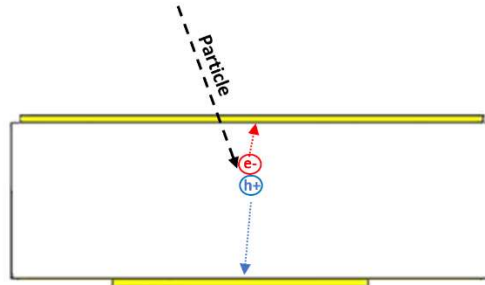

Figure 2-1. A particle creates e-h pairs in a solid-state detector bulk

Based on the previous ideal characteristics, diamond generally has better characteristics than those of silicon as shown in table 1. The only major drawback is high ehp creation energy. However, this disadvantage does not prevent diamond to be an ideal particle detector. Some methods are developed to compensate the creation energy problem of diamond-based particle detector [Sku16, Mus17]. Moreover, some single-crystal Chemical-Vapor-Deposition (scCVD) Diamond sensors have been installed in the Large Hadron Collider (LHC) at CERN as Beam Monitoring detector since last decade [Vel08]. The installation is an evidence of the

highly reliable wide-gap semiconductor in application of high energy particles detector. In this work, the issue of large ehp creation energy is addressed in detail on chapter 6.

Table 2-1. Properties of silicon and diamond [Kas17, Ras08]

Property	Silicon	Diamond
Bandgap (eV)	1.12	5.47
Maximum Electric Field (MV/cm)	0.41	20
Electron Mobility (cm^2/V.s)	1450	1900 - 4500
Hole Mobility (cm^2/V.s)	480	1800 - 3800
Saturation Velocity (x10^7 cm/s) at 300 K	0.86	2.7
Thermal Conductivity (W/cm.K)	1.5	20
Relative Dielectric Constant	11.7	5.7
Displacement Energy (eV)	13-20	43
e/h-pair Creation Energy (eV)	3.62	11.6-16

2.2 The Advantages of Wide-Gap-Energy Semiconductor

A material with some specific properties is classified as an ideal choice to perform well as particle detector under an intense radiation condition [Nov08]. First, large band gap is main characteristic for achieving a small leakage current under high electric field and high temperature condition. Low leakage current is necessary for generating low noise during detector operation. Second, low dielectric constant results in a low capacitance of the particle detector that reduces the series noise. Third, a material with low defect density and low unintentional doping concentration is desired. The property is required to optimize the charge collection, minimize leakage current and result in a better energy resolution. Forth, material with a long carrier life time is desirable. The life time indicates the maximum time of charge carriers before the carriers are trapped by atoms or defects. Sufficient life time period is necessary to achieve good charge collection efficiency. Fifth, atomic displacement energy is the minimum amount of kinetic energy transferred by the impinging particle to create a defect in the detector lattice structure. Defect induced by the radiation of particles can act as trapping

centers for the charge carriers. Abundant trapping centers prevents excellent charge collection and high energy resolution. Seventh, maintaining temperature of the solid-state detector is one method to increase its radiation hardness. With a better thermal conductivity, the heat transfer from the detector occurs more efficiently. Finally, a material requires a certain minimum energy to create electron–hole pair that is called pair creation energy (ε). A high signal-to-noise ratio (SNR) can be easier to be achieved if the generation energy is low. Thus, number of created ehp by an ionizing particle can be large compare to the noise level. However, the energy tends to be proportional with the value of band-gap.

A high energy particle with high fluence can increase detector temperature significantly. The wide-gap material maintains its performance at a very high-temperature environment when silicon already failed [Nav08]. Diamond also shows at least two orders of magnitude lower leakage current than that of silicon [Bru08]. Silicon can still maintain its energy resolution at +30 ^{0}C or lower [Nav08]. However, practically the temperature of silicon detector is kept cold below 0 ^{0}C to suppress the excessive noise from the dark current [Nav08]. Consequently, the additional cooling system is utilized for maintaining silicon detector optimum performance. The additional mass results in higher probability of particle scattering. Moreover, the front-end electronic system is often in contact or integrated to the detector bulk. Therefore, the higher thermal conduction of diamond is crucial to better control of the system operational temperature.

The high breakdown field of diamond permits its operation under higher electric field condition. High field allows the detector to work in the regime of charge-carriers saturated velocity. This condition minimizes the charge collection time while it excites the ehp in detector crystal.

The penetration of particles from the collider deposits a significant energy that can break the detector atomic structure. The higher radiation dose results in a more significant degradation detector performance [Bru07]. Diamond detector that has significantly higher threshold of displacement energy is more capable of working under larger energy deposition than silicon-based detector. The better mechanical robustness of diamond is resulted from stronger binding energy of its atoms.

The main property for a wide energy-bandgap material is that it requires higher energy to activate free carriers. The higher activation energy results in significantly a lower leakage current. Furthermore, the small dielectric constant of diamond crystal result in small capacitance. Those factors generate significantly less leakage current and lower noise level.

Therefore, it gains better signal-to-noise ratio (SNR). The typical leakage current of the diamond particle detector in normal operational condition is 0.1 nA/cm^2, whereas that of silicon is 10 nA/cm^2, about two orders of magnitude larger than it. However, using diamond also has a significant drawback as particle detector because energy required to excite ehp are significantly higher. It requires 13 eV for diamond compared to 3.62 eV for Silicon. Thus, the energy resolution of diamond is about three times smaller than that of silicon. To overcome this problem, diamond detector capable of generating carrier amplification in its active layer is designed.

Another fact about diamond is that it has deep activation energy for currently known doping. It is often considered as the main drawback of diamond as a material for electronic devices. The two shallowest doping are boron that acts as main positive-type doping and phosphor acts as main negative-type doping which requires activation energy 0.37 eV and 0.57 eV respectively. Those energies are significantly higher than the activation energy of the shallowest doping in silicon i.e. 0.045 eV for Boron. This results in some difficulties to use the diamond to transmit high current in some applications. However, for particle detector application, this is not a problem because the device is only expected to work on a reversed bias and generate as low leakage current as possible.

For matching the performance of silicon's energy resolution, carriers in diamond should be multiplied at least by a factor of three. In generating carrier amplification, it requires high electric field. Some experimental data indicate that diamond can withstand very high electric field up to 20 MV/cm [Lan93]. On the other hand, some references that calculate the value of ionization coefficient by Monte Carlo calculation nor measurement from diamond device do not agree about the minimum electric field required to generate multiplication effect in the active layer of the diamond. However, the range of the minimum electric field is between 0.3-1.1 MV/cm. In this study, the threshold field of 0.3 MV/cm is used as the reference for developing the future device. Then 0.3 MV/cm field will be called as threshold field for later discussion.

Two research groups claim that they succeeded to generate charge multiplication effect in their diamond device. The first approach is using an extremely thin diamond active layer with 3.2 μm thickness [Sku16]. By using a thin layer, the high electric field could be reached by biasing the device with a reasonably low bias voltage. The second approach is using a small diameter metal contact on a surface of the diamond device. The smallest one is 20 μm in diameter

[Mus17]. Those small electrodes focus the electric field in a small area under its interface. In this work, those two approaches that are claimed to be capable of generating carrier multiplication are evaluated. Furthermore, others method that might be suitable to enhance electric field in the diamond's active area such as 3D contact [Oh13] and etch-pit structure [Tsu16] on the surface of the diamond are evaluated. However, the most suitable structure that improve electric field significantly and efficiently is a diamond crystal with a needle structure. Further discussion about the structure is written in chapter 6.

2.3 Diamond Synthesis and Surface Termination

The main method for synthesize a high-quality diamond crystal is Chemical Vapor Deposition (CVD). Two variants of CVD diamond crystal are poly-crystalline (pcCVD) and single-crystalline CVD (scCVD) diamond. In theory the scCVD diamond performs better as detector compared to the pcCVD diamond. The pcCVD diamond inherently has significant number of trap levels due to the existence of crystal grain boundaries. Therefore, scCVD diamond is preferable for the detector application with more intricate process to manufacture as the trade-off.

In the CVD process, precursor gas chemically reacts to the surface of a solid substrate to form covalent band. The deposition process is initiated by exposing the substrate with carbon gas that is diluted in hydrogen. A widely used precursor gas is a high purity CH_4 (methane) gas activated by high temperature or electrical discharge [Pom08]. The high temperature is also applied to the substrate to improve the formation of thin film diamond on the substrate. One of the most common substrates to grow CVD diamond is High-Pressure High Temperature (HPHT) diamond substrate.

Passivation of the diamond surface is an important process in fabrication of diamond crystal after the growing process of diamond film finish. On the surface of CVD diamond film, the carbon atom has a dangling bond. The surface property of diamond is crucial for determining the quality of diamond device. Two stable termination process is commonly conducted on the surface of CVD diamond crystal. Those are oxygen termination and hydrogen termination. Due to the abundant hydrogen atom in CVD process, the surface CVD diamond is terminated by hydrogen in the end of Diamond CVD process. However, the standard method to fabricate the H-termination on diamond surface is exposing the surface of CVD diamond to a flow of high temperature hydrogen (H_2) plasma [Neb06, Wil04]. The hydrogenated surface has variation of

surface resistant in ambient air and in vacuum condition. The resistance increases significantly at vacuum [Neb06]. The second variant of stable termination is Oxygen-terminated surface. Exposing diamond surface to oxygen plasma or submerging diamond sample to a high temperature strong acid solution converts the dangling-bonds on the diamond surface to be an oxygen-terminated surface [Liu09]. The oxygen atom can form two covalent bonds; therefore, a single oxygen atom binds covalently to two dangling-bonded carbon atoms. The MIM diamond sample used to evaluate the characteristics of diamond is oxygen-terminated type.

2.4 Preparation and Deposition of Metal Contact

Preparation of cleaning the contamination on diamond surface and metal contact deposition is needed because the diamond crystals were purchased without metal contacts. Prior to metal contact deposition, possible contaminations on the surface diamond crystal need to be removed by a chemical process. The cleaning is conducted with a mixed-acid H_2SO_4 and HNO_3 solution with a ratio of 3:1. The crystal is submerged in the solution for 70 minutes at 450 ^{0}C. The step is followed by decreasing the temperature slowly for about 30 minutes. The final cleaning step is immersing the crystal in pure water for 5 minutes then dry the crystal with paper towels.

Two types of metal contacts are deposited on the diamond detector, the first is aluminum contact, and the second is Titanium/Platinum/Gold (Ti/Pt/Au)) contact. The aluminum contact is deposited by a resistive thermal evaporation method. Inside a vacuum chamber, the diamond is covered by a mask to create a desired metal contact geometry. The crystal is exposed to aluminum vapor. The vapor is produced by flowing a high electric current about 10 A through aluminum-coated tungsten wire. The high current increases the temperature and transform the solid aluminum to vapor. Higher current results in higher deposition rate. After deposition of few tens of nanometers thick on the diamond surface, the aluminum depositions can be eliminated. This process normally produces a Schottky contact on the diamond device. On the other hand, the Ti/Pt/Au contact is deposited by electron beam vapor deposition. The process is similar with the resistive thermal deposition, except the metal vapor is produced by collision of a high energy electron beam with a metal target. Each layer of metal is deposited from different metal target. The titanium is intended to be ohmic contact. To align the fermi level of diamond and titanium, a high temperature annealing process is conducted. Due to high reactivity of titanium, the additional platinum and gold layer is added, therefore the annealing process does not introduce the oxide layer to the diamond/titanium interface.

Chapter 3

Methodology

In this work diamond detector was evaluated by simulation, measurement of signal and analytical calculation. To understand the transport properties of the diamond, a Schottky-contact diamond detector with a basic geometry was characterized. By extracting the basic properties from the experiment, a model was constructed to explain whole data. The model will be implemented in an analytical calculation to understand clearly the effect of each parameter. For detail understanding, the Sentaurus TCAD simulation is utilized. By constructing a model that satisfies the experimental data, the model is used for designing new diamond device, which could be used to solve the main drawback of diamond detector i.e. low energy resolution.

3.1 Simulation

For designing and optimizing the particle detector device, a computer simulation program is utilized. Computer simulation is a very effective, economical and faster method of designing and evaluating a complete system before building a prototype. Two level of main simulation program that can be used for designing and evaluation process are Sentaurus TCAD by Synopsys and Spectre by Cadence.

3.1.1. Technology Computer-Aided Design (TCAD)

In this work, a finite element simulation is used to screen the possible technology that could be applied to enhance electric field in a diamond device. The variant of the program currently operated is Sentaurus TCAD by Synopsys. This software is capable of simulating properties of wide range semiconductor devices set up in 2D or 3D [9]. Furthermore, TCAD is capable to simulate electrical responses of the semiconductor device toward external inputs such as voltage biasing, change of temperature and penetration of particles. With limitations of some fabrication processes, TCAD can be used to optimize the design of the future diamond device, so that the design can generate the desired properties.

Unfortunately, diamond is a new material uncommon for electronic purposes. Therefore, it is not available in Sentaurus TCAD standard library. Thus, essential properties of diamond material should be inserted manually in TCAD customization files. In the development of new detector designs, the reliability of TCAD simulation should be tested. For that purpose, experimental data of the MIM diamond detector was compared to the results of TCAD simulation.

TCAD simulation is used to optimize the geometry and structure of the detector. TCAD are capable of evaluating comprehensively a design and structure of semiconductor device. This program allows us to simulate some essential properties of the detector device such as doping concentration, geometry, type of material, the position of contact, defects and so on. Furthermore, TCAD can simulate complex structure of guard rings, punch-trough of space charge region (SCR), static characteristic and dynamic transient profile of voltage and current during the detection process of particle [Lut10, Ben]

The workflow of TCAD simulation is started by describing the geometry of the detector, the type of material, the type of contact and the concentration of doping. A meshes structure is implemented to divide the geometry to be many smaller sections that makes vertices at the intersections of the sections' boundaries. By solving diffusion and transport equations for each discrete vertex, TCAD simulator checks the convergences of the calculation in each vertex. If the calculations are converged, the simulator calculates the next input values. Otherwise, the simulator repeats the measurement with different arithmetical step. The complete parameter values and distribution are generated after the simulation calculation results in a set of convergent parameter values.

3.1.2. Electronic Computer-Aided Design (ECAD)

For evaluation the signal generated by the particle detector, a readout system of Application-Specific Integrated Circuit (ASIC) need to be developed. ECAD is a widely-used for analyzing and designing electronic circuit. In this case, study the circuitry of the readout system and development of ASIC are conducted by using Cadence Simulation. ECAD uses numerical techniques to analysis a complex circuit. By specifying textual command of the circuit, a graphical output is displayed for running the simulation. All of the circuit components are cover in ECAD libraries such as passive and active devices, transmission line, and dependent/independent sources. Furthermore, ECAD can perform linear A.C, non-linear DC

and non-linear transient analysis [Mas]. By these complete functions, the detail arrangement of components in readout ASIC could be designed to result in an optimum signal for the particle detection application.

3.2 Characterization Method

After a detector is fabricated, the device should be characterized to evaluate its performance. Parameters that describe the performance of semiconductor detectors are the dark current as a function of bias voltage, the Charge Collection Efficiency (CCE) and shape of transient signal.
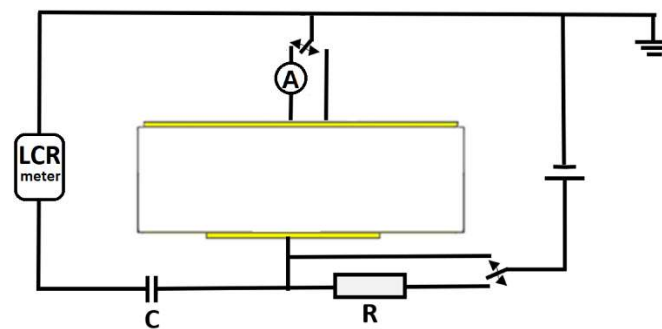
Fig 3-1. Schematic drawing set up for dark current and capacitance measurements. The measurements are conducted between the upper and lower contact. The two switches allow to choose between I-V and C-V measurement mode. I-V characteristic is simply conducted by measuring the current flow to the amperemeter. To measure the C-V characteristic, the LCR meter supplies a few millivolts AC voltage to the device while measuring amplitude and phase shift of the AC current [Bec10].

3.2.1 Current versus Voltage (I-V) Characterization

I/V measurements are carried out by applying a certain DC voltage to the device and measuring the Direct Current (DC). For detecting purpose, the device normally works in reverse bias condition. The reverse bias condition is expected to produce as low as possible leakage current to result in a high-quality signal for energy spectroscopy. These measurements are then used to qualitatively determine the dark current for a certain range of applied voltage value that is possibly used during the detector operation (figure 3-1). The measurement of I-V characteristic is carried out without the exposure of particles.

3.2.2 Capacitance versus Voltage (C-V) Characterization

For characterizing the capacitance as a function of voltage, the sensor is biased with two voltage sources simultaneously, a DC and an AC voltage source. In order to characterize the detectors capacitance, the AC current is integrated as the stored charges in the device (ΔQ). Then, the integrated current is divided by the change of voltage (ΔV) as shown in equation:

$$C \equiv dQ/dV$$

(3.1)

The ramping up DC voltage give information about the capacitance as function of the bias voltage. The change of the capacitance is caused by the increasing the DC voltage extends the depth of depletion layer. Ideally, the measurement of charge carrier concentration of the detector crystal also can be carried out by linear relation of C^{-2}-V as shown in equation [Zey06]:

$$C^{-2} \equiv \frac{2(V_0 - V)}{q \varepsilon_s n_h A^2}$$

(3.2)

with V_0 is the intersect of the extrapolated linear line of C^{-2}-V plot with V-axis at $C^{-2} = 0$, q is the charge of each carrier, ε_s is the permittivity of the material, n_h is charge carrier concentration, and A is area of the metal contact.

3.2.3 Charged particle spectroscopy

Charged particle spectroscopy is a standard technique to evaluate basic transport parameters for particle detectors. This characterization method is based on the measurement of the current or the charge generated by the ionization of incident particle. The shape of the generated signal of induced charge reflects the charge carrier transport properties of the detector that can be used to analyze the structure of the material. Two advantages of this method are to characterize the transport parameters of a complete detector system and the read-out system, the penetration power of high-energy particles allows studying the profile of deep active layers of the device.

The parameters that were studied mainly the dark current, the CCE and the transient signal of particles. Characterization of those basic parameters is carried out by using Minimum Ionizing Particle (MIP), β-particle from a nuclear isotope Strontium-90 (^{90}Sr) and α-particle from nuclear isotope Americium-241 (^{241}Am).

The CCE value can be derived from the ratio between collection length (L_C) and dimension of depleted region (L_D) [Kno93]. The collection length is defined as the value of total collected

charges resulted from the induced particle (Q) divided by the value of generated charges (n) per unit length. It is simply written as:

$$CCE = \frac{L_C}{L_D} \quad \text{, with } L_C = \frac{\langle Q \rangle_{collected}}{n.e} \quad . \tag{3.3}$$

with value of n depends on the type of the particle and the material of detector, and e is the charge of electron (1.6 x 10^{-19} C). Another method to measure the CCE is conducted by comparing the histogram peak position from a CCE measurement setup to the reference. A more detail explanation is provided in the next chapter.

The value of CCE is one of the most important parameters to acquire information about the quality of the material because it contains information about device capability to generate charges from incoming particles. The CCE is extracting from the peak position of histogram from a setup with a Charge Sensitive Amplifier (CSA). The CCE value corresponds to the quality of contact, the trap concentration inside the bulk of the detector and the distribution of electric field. On the other hand, the Full-Width-Half-Maximum (FWHM) value of the histogram implies the quality of the generated signal. A broader FWHM indicates the deterioration of the signal mainly because of Fano fluctuation.

Transient current signal is one of the most important observables to study the characteristic of semiconductor crystal. By evaluation of the signal, carrier concentration, carrier mobility and carrier lifetime can be extracted. The transient signal can be studied with a fast current-sensitive amplifier. The signal current in a detector can be expressed with an equation based on Ramo's theorem [Ram39]:

$$i = evE_v \tag{3.4}$$

with e is the charge of electron 1.6 x 10^{-19} C, v is charge carrier velocity, and E_v is a normalized electric field.

Chapter 4

Characterization of Diamond

The characterizations conducted using the Metal-Intrinsic-Metal (MIM) diamond device are measurement of I-V characteristic, CCE, depth of depletion layer and Transient Current Technique (TCT) Characterization. The I-V characteristic is important to study about the doping concentration and the energy barrier of metal contact on the diamond. The measurement of CCE can be used to determine the quality of the bulk by calculation of carrier lifetime. The measurement of depth of depletion layer can give additional information about the number of charge carriers in the diamond bulk. Finally, the TCT Characterization is used to determine the mobility of carrier, saturation velocity of carrier and distribution of electric field inside the diamond crystal.
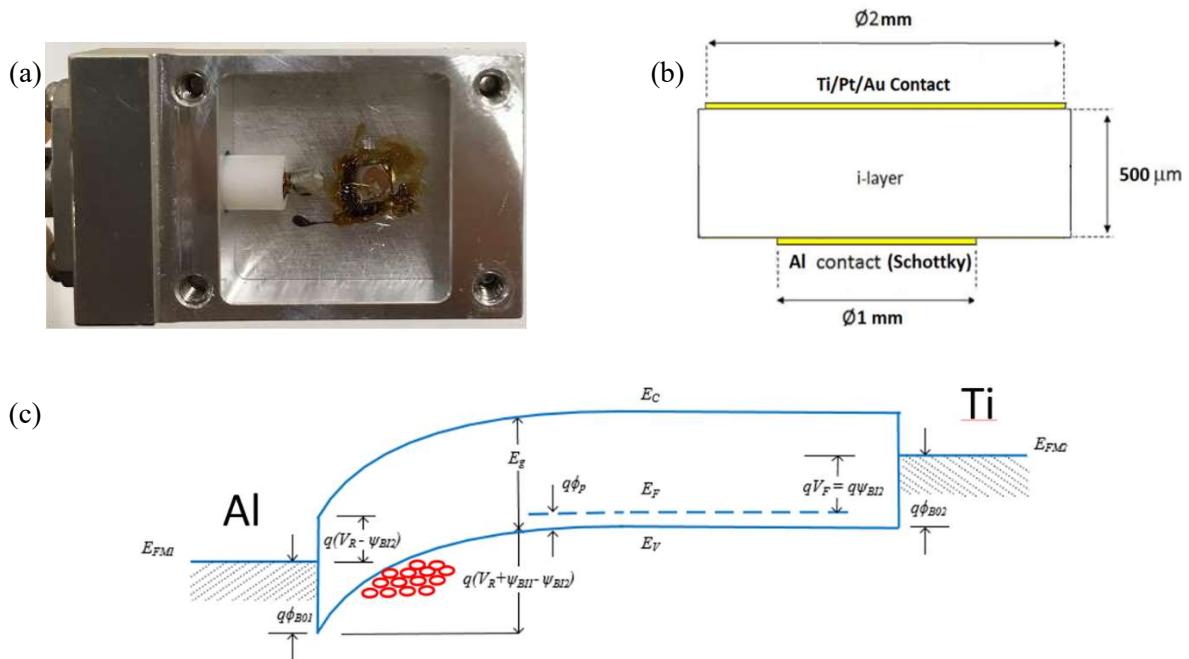
Figure 4-1. (a) picture and (b) diagram of MIM diamond device with Ti/Pt/Au-Contact and Al-Contact version. (c) The energy band diagram of MIM diamond detector. The Al-Contact and Ti/Pt/Au-Contact intends to be a Schottky and Ohmic contact, respectively..

4.1. Metal-Intrinsic-Metal (MIM) Diamond

In order to construct a model for designing the new diamond detector, characterization of a conventional MIM diamond detector made from high quality diamond crystal is conducted. The crystal is bought from ElemenSix and it is an ultrapure bulk diamond [El6]. The crystal used in this study is electronic grade Single Crystalline (SC) Chemical Vapor Deposition (CVD) diamond bought from ElementSix with a thickness of 500 μm and cross-section of 4 mm x 4 mm (Figure 4.1). Based on ElementSix diamond handbook [El6], the boron concentration in the crystal is < 1 ppb ($\approx 10^{14} / cm^3$). Both metal contacts made by a collaborator from Hokkaido University [Takahiro Shimaoka] and those two contacts supposed to have a different electrical characteristic. The first is formed by depositing 10 nm thick aluminum layer with a diameter of 1 mm on the oxygen-terminated diamond surface that results in a Schottky contact. On the other hand, the opposite contact is made by depositing three layers of metal i.e., Titanium-Platinum-Aurum (Ti-Pt-Au) in a respective order with a diameter of 2 mm to the surface of the diamond. This type of metal layer is widely suggested as an excellent ohmic contact for diamond device [Tac92, Tan06, Wan00].

4.2 Experiment Setup

4.2.1 I-V Characterization
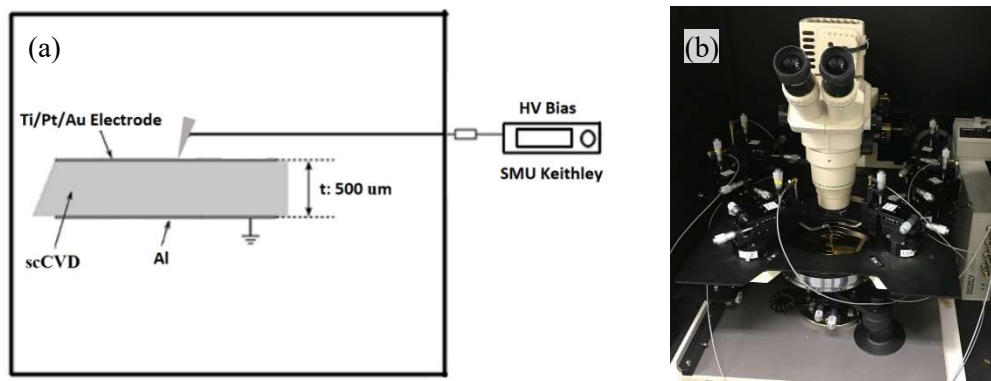
Figure 4-2. The diagram and the photograph measurement setup of prober station I-V Characterization of MIM Diamond detector inside a Faraday cage are shown in (a) and (b), respectively.

I-V characterization was conducted by using a prober-station. A probe touched the Ti/Pt/Au contact while the Al-contact sit on the chuck of the prober-station. A pump sucks tightly the

Aluminum plate, and the plate is set as the ground. The measurements are conducted in ambient air at room temperature. The current is measured with Keithley 2400 Source Meter Unit (SMU). The SMU biased the probe station and measured the current simultaneously as seen in Figure 4.2

4.2.2 CCE Measurement

The CCE measurement is important to evaluate the quality of the diamond crystal and metal contact. The quality of the diamond crystal and metal contact are reflected by the carrier lifetime of diamond which can be derive from the data of CCE as function of bias voltage and drift-time of carriers.

To measure the CCE of the crystal, the MIM diamond is connected to devices as shown in figure 4.3. The Aluminum-Side (Al-side) is connected to ground. On the other hand, Titanium-side (Ti-side) is connected to Charge Sensitive Amplifier (CSA) that has role of preamplifier. The CSA used in this experiment is CAEN A1422. The CSA has a built-in circuit tee. Therefore, high voltage power supply can be directly connected to the preamplifier. The CCE is measured by exposing both side of contact to the α-particle. By exposing both contacts, the effect of metal type for diamond contact can be studied.

The signal for CCE measurement is generated by mainly 5.486 MeV α-particles from [241]Am radioactive source with intensity of 4.25 kBq. Most energy (> 99%) of the α-particle is deposited to the detector because α-particle only penetrates less than 15 μm in a diamond layer [Kas16]. The shallow penetration depth with a collimator is not a crucial to measure the CCE. In this case, the collimator is the aluminum case of diamond detector with a thickness of 1 mm and opening diameter of ≈2 mm. The preamplifier processes the signal from the detector. The trailing time of the preamplifier signal is typically few hundred of microseconds. To prevent the pileup of the consecutive signals that can have period less than 1 μs, the signal needs to be processed by spectroscopy amplifier. Therefore, the preamplifier signal is processed by CAEN N968 Spectroscopy Amplifier to form a desired semi-gaussian signal. The shaping-time of the amplifier is set to be 0.5 μs.
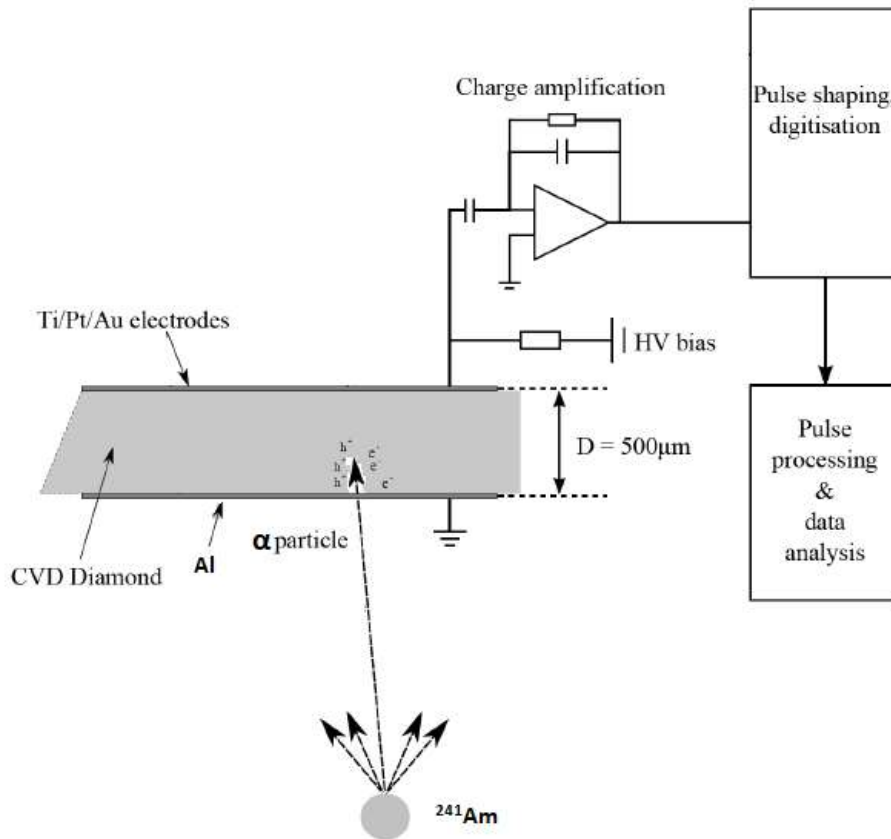
Figure 4-3 The setup of CCE measurement.

The final step is a signal processing conducted by Multi-Channel Analyzer (MCA) MCA-8000D coupled with the auxiliary computer software. The software presents the signal in the form of a multichannel histogram correlated with the amplitude of signals from the amplifier. The position of the peak in the multichannel histogram defines the CCE of the device. However, for a precise measurement of CCE, the signal needs to be calibrated because some of α-particle energy loses in the thin metal contact of the diamond detector without generated any signal. A PIN S3590-09, Hamamatsu silicon photodiode is used as a reference for this Diamond detector CCE measurement. The measurement is conducted inside a vacuum chamber at room temperature.

4.2.3 Depth of Depletion layer

This measurement is conducted to acquire information about the depth of depletion layer under Schottky Barrier. The depth of depletion layer under Schottky Barrier is essential information

that can be used to calculate the value of carrier concentration. By I-V characterization, hints about the values of carrier concentration and energy barrier are obtained. However, the acquired information is determined by those two parameters simultaneously. Therefore, the additional information from I-V characterization is crucial to obtain more precise estimation about the two basic parameters.
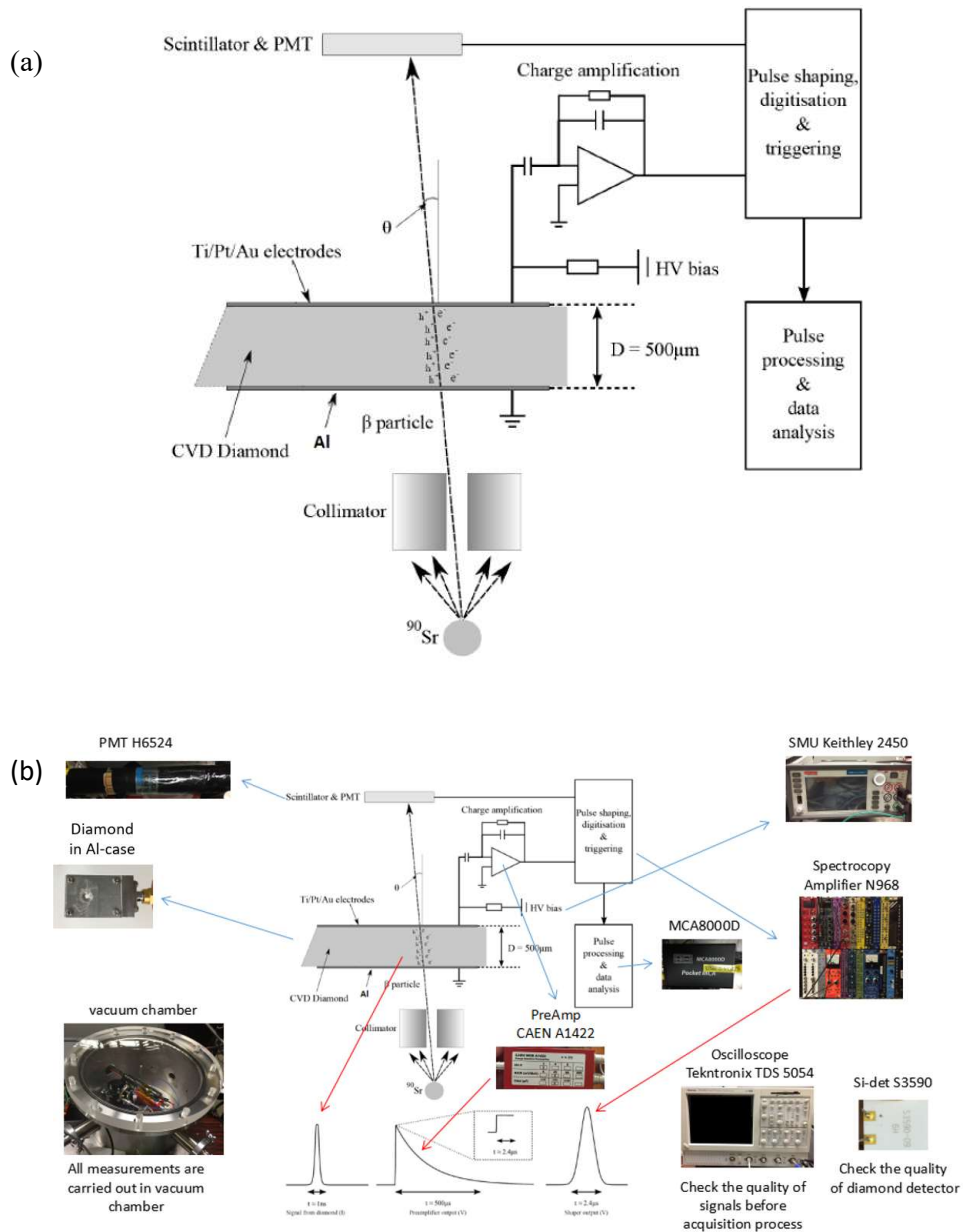
Figure 4-4. (a) Setup for measuring the depth of depletion layer. (b) The picture of every device related to each stage of measurement process of a signal from a β-particle.

In order to conduct measuring the depth of depletion layer, this measurement uses beta-particle source Strontium-90 (^{90r}Sr). A high energy beta particle can penetrate thick bulk of diamond

crystal. However, the signal is quite weak to be captured by MCA. To help the MCA to capture the signal, Photo Multiplier Tube (PMT) connected to Scintillator was utilized as shown in figure 4.4. The energetic beta particle that passes through the crystal will be detected by Scintillator. Beside the additional PMT to trigger the signal, the rest of setup is similar to the setup of CCE measurement with α-paricle.

4.2.4 Transient Current Technique (TCT) Measurement

TCT is obtained from experiment that exposing detector to discrete input such as particles and laser that triggers a current signal in detector with a short period (few nanoseconds). By TCT measurement, information about mobility of charge carrier, saturation of drift velocity and distribution of the electric field inside the crystal can be acquired. For high precision timing measurements of short signal, this experiment needs fast amplifier with large bandwidth. The setup for TCT measurement is shown in figure 4.5. All of the measurements are conducted inside a vacuum chamber at room temperature.

The setup consists of diamond detector, circuit tee, high voltage power supply, fast amplifier and Oscilloscope. In this measurement, MIM diamond device is utilized. For the circuit tee, a capacitor with 6 kV rating is installed. The fast amplifier is a minicircuit Gali52+ with bandwidth DC to 2 GHz. The amplifier has 20 dB gain. The output of the fast amplifier is evaluated with an oscilloscope Tektronix TDS 5054 with a sampling rate of 5GS/s and frequency range to 500 MHz.

The Diamond detector is connected to the high voltage power supply and fast amplifier through circuit tee. The circuit tee consists of a capacitor with a high voltage rating and a large resistor. Those two components split DC and AC signal from the diamond detector. The capacitor blocks large DC current from high power supply. On the other hand, the resistor prevents transient signal flow to high voltage power supply. The signal is directed to the line with capacitor and amplified by fast amplifier.
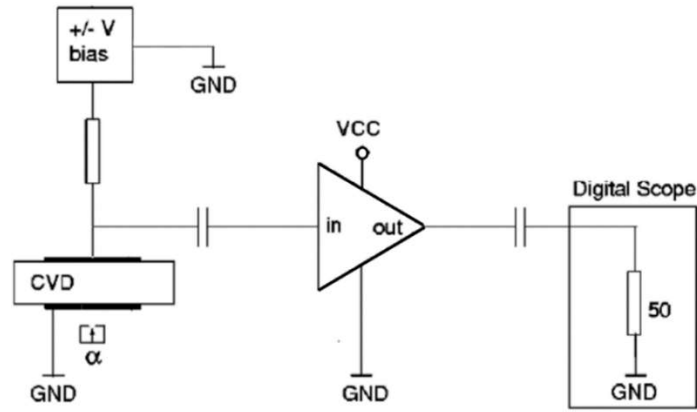
Figure 4-5. TCT measurement setup.

4.3 Measurements Results

The measurements are carried out with the setups explained in the previous subchapter. The aim of the measurements is to characterize the important properties of diamond detector.
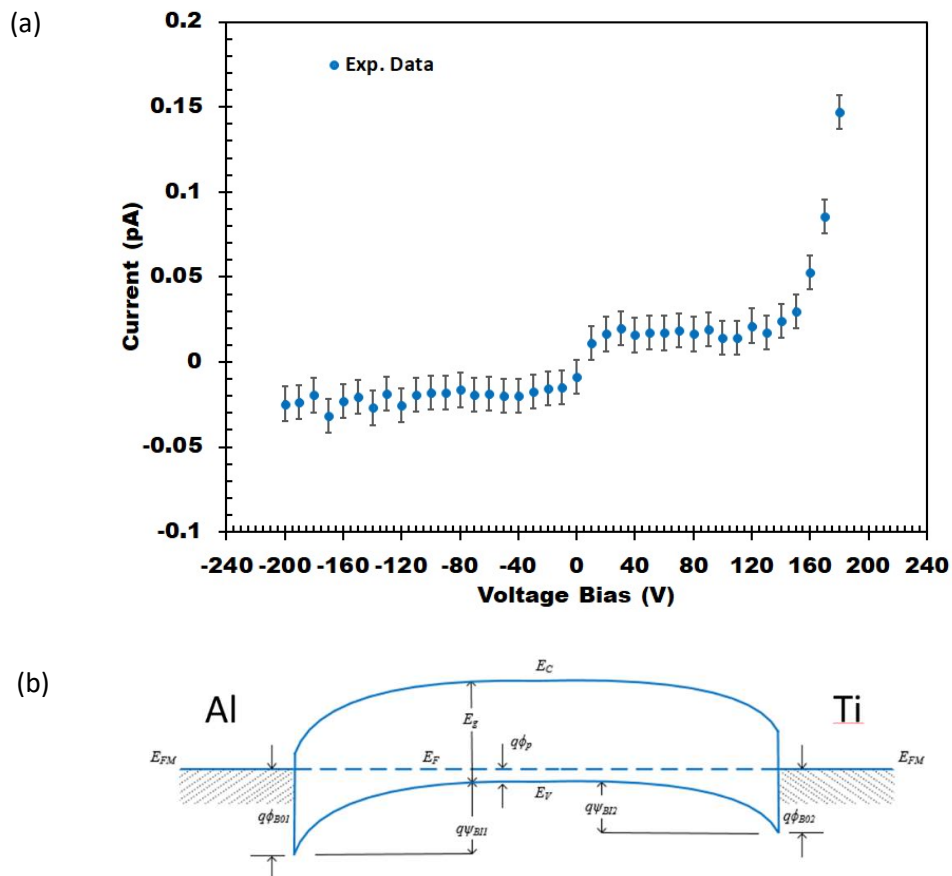
4.3.1 I-V Characteristic

(a)

(b)

Figure 4-6. (a) The I-V characteristic of 500 μm MIM Diamond detector. (b) Both side metal contacts have a Schottky barrier.

23

The Ti/Pt/Au-contact behaves indifferently as Al-contact. This shows the I-V characteristic in forward bias that results in a current less than 1 nA/cm^2 under both polarity of bias voltage $|V_{bias}| \leq 200$ V (figure 4-6a). The experimental data of diamond MIM device indicates that the sample has double-Schottky contact (figure 4-6b). The low current indicates either low carrier concentration of the bulk, high energy barrier of metal contact or combination of both. Both effects are undistinguishable from I-V characteristic measurement result due to an extremely low current under low bias condition. To distinguish the effect, a TCT characterization needs to be conducted to confirm the charge carrier concentration independently.

4.3.2 Charge Collection Efficiency (CCE)

MCA results in histogram that can be used to determine the value of CCE. The MCA histogram provides information about number of counts and the position of the signal amplitude at appointed bin (figure 4.7). The position of the bin gives information about the number of generated charge when an α-particle deposits its energy to the diamond. The distribution data reflects variation of generated charges during the measurement. The generated charge is closely related to deposited energy of the particle. The distribution is due to the different angle of incoming α-particle, energy straggling in the metal contact, Fano fluctuation and electronics noises.
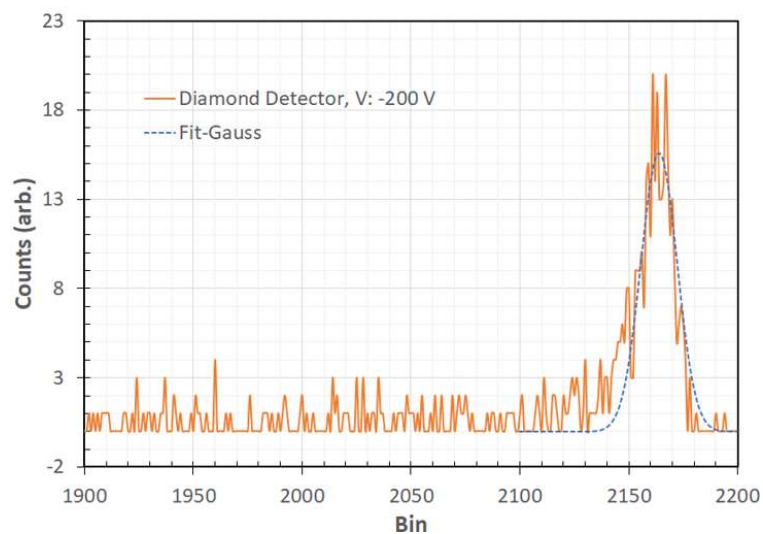

Figure 4-7. The solid purple line reflects distribution of generated charge while diamond exposed to alpha particle under -200 V bias voltage. The dashed blue line is a Gaussian fit to the energy distribution. The peak position is at bin 2164. The energy resolution ($\Delta E/E$) is 0.9 % ($\approx$ 49 keV).
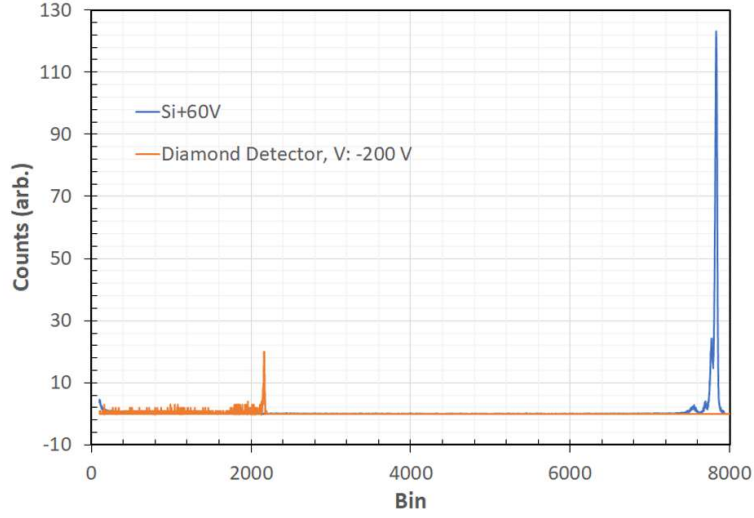
Figure 4-8. The blue histogram represents the energy distribution of alpha particle in silicon detector. The peak position of silicon's histogram is 7831 and the energy resolution is 0.4 %. The purple histogram represents energy distribution of diamond detector under -200 V bias (as seen in figure 4-7).

To calculate the value of CCE of the diamond, data from a detector that is widely considered as standard device is referred. For this purpose, the distribution of α-particle energy in silicon detector is used as the reference as shown in figure 4-8. The CCE of silicon detector is assumed to be 100%. To calibrate the measurement setup, test step pulses with different voltage values are fed to the setup (figure 4-9). The calibration results in a graph with a gradient and a y-intercept value for both diamond and silicon detector. Those two parameters can be used to obtain the CCE value of diamond detector as shown by a calibration formula [Har18]:

$$CCE_{Dia} = \frac{Peak\_ch_{Dia} - c_{Dia}}{Peak\_ch_{Si} - C_{Si}} \times \frac{\varepsilon_{Dia}}{\varepsilon_{Si}} \times \frac{m_{Si}}{m_{Dia}} \times \frac{5.486\ MeV - \varepsilon_{loss\_Si}}{5.486\ MeV - \varepsilon_{loss\_Dia}} \times 100\%, \quad (4.1)$$

with $Peak\_ch_{Dia}$ and $Peak\_ch_{Si}$ are the histogram peak channel of diamond detector and silicon detector, respectively. The m_{Dia} (m_{Si}) and c_{Dia} (c_{Si}) variable are gradient and y-intercept value for diamond (silicon) detector, respectively. The ε_{Dia} and ε_{Si} variable are the required energy to excited electron-hole pairs in diamond and silicon detector with a value of 13.1 eV and 3.62 eV, respectively. The ε_{loss_Dia} (ε_{loss_Si}) variable is energy loss of α-particle in the metal contact of diamond (silicon) detector. The energy losses of α-particle in silicon and diamond metal contact are estimated about 0.047 MeV [Aki06] and 0.002 MeV, respectively. The energy loss in the diamond is calculated with Bethe's equation by assuming the thickness of Aluminum contact 10 nm.
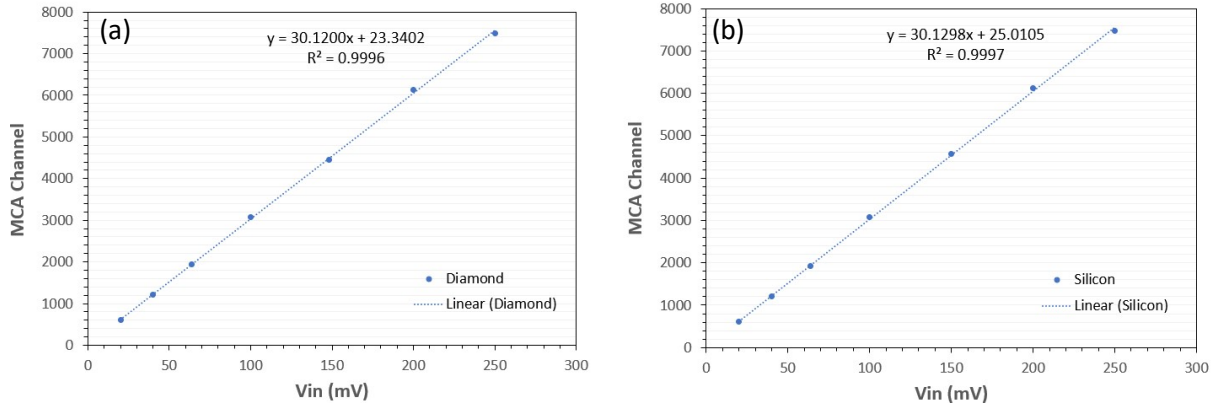
Figure 4-9. The calibration of CCE measurement setup for (a) diamond detector and (b) silicon detector. The position of the peak histogram in the MCA channel is calibrated by step pulses. The gradient and y-intercept value of the graph are extracted to calculate the calibration parameter of diamond detector.

The CCE calculation results in the distribution of CCE as seen in figure 4-10. The exposure of α-particle to Al-contact results in high CCE of 96.9±0.4 % or higher for holes under a bias voltage higher than 80 V. The decrease of CCE at lower bias voltage indicates the existence of traps level in the diamond crystal. The concentration of traps level is reflected by lifetime of the charge carrier that is discussed in the subchapter of transient signal evaluation.

In the CCE setup as shown in figure 4-4, Aluminum-Side (Al-side) contact is connect to ground. On the other hand, the Ti/Pt/Au-Side (Ti-Side) is biased with High-Voltage (HV) Source Meter Unit (SMU). The red (blue) circle data points are acquired if α-particle is illuminated from Al-Side with a negative (positive) bias. Conversely, the red (blue) triangle data points are acquired if α-particle is illuminated from Ti-Side with a negative (positive) bias.

For the blue triangle data points, α-particle is illuminated on the Al-Side opposite with the side in which electric field start to extend as shown in figure 4-11. The CCE reaches value > 50% under 10 V bias voltage, and CCE reaches ≈ 90% under 20 V bias voltage. The α-particle penetrates shallow layer of the diamond by some few tens of micrometers. As suggested by Ramo's theorem, current signal is not generated in area in which electric field absent. Therefore, the high CCE under low bias voltage means the electric filed is covered entire 500 μm thick crystal under low bias voltage. With the Gauss Law, an equation about the depth of depletion layer of metal-semiconductor structure can be derived as [Sze07]:

$$W = \sqrt{\frac{2\varepsilon_S}{qn_h}\left(\psi_{bi} - V - \frac{kT}{q}\right)}, \qquad (4.2)$$

with ε_s is permittivity of the semiconductor, q is charge of carrier, n_h is charge carrier concentration, ψ_{bi} is built-in potential due to the Schottky barrier, k is Boltzmann constant, and T is absolute temperature. Based on the formula, the low fully depleted condition under low bias condition represented by blue triangle can be used to estimate the concentration of charge carrier in the diamond crystal which is $n_h \leq 10^{11}$ /cm^3. The value of built in potential that is correlated to the height of Schottky barrier does not significantly affect the estimation because the order only within few Volts.   α
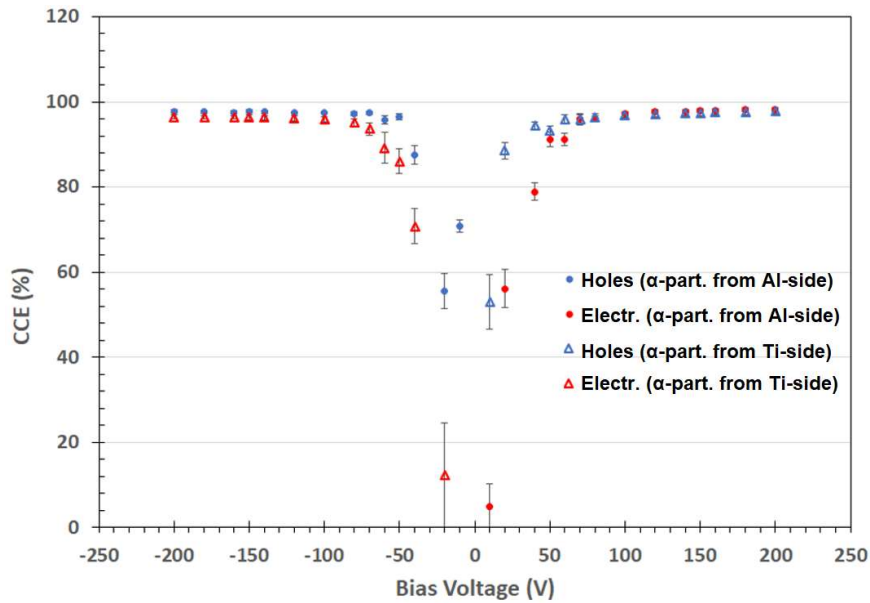
Figure 4-10. The CCE of MIM device is almost 100 % under high voltage bias condition for either contact. The error bars represent Full Width Half Maximum (FWHM) of the Gaussian distribution.
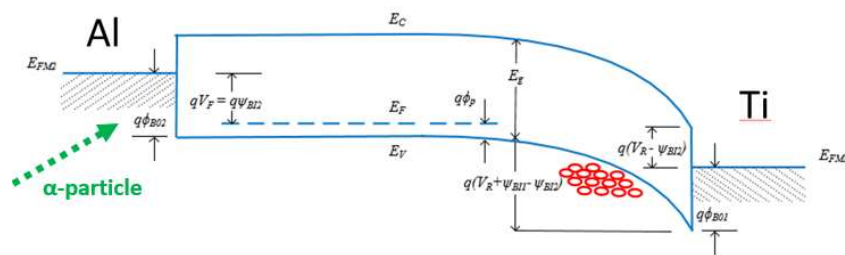
Figure 4-11. The energy band of Diamond detector with Al-Side grounded and Ti-Side bias with a low positive bias. The electric field is proportional to the gradient of energy band. In a low bias voltage, electric field is only concentrated near Ti-Side. An α-particle is illuminated from the Al-Side in which electric field is absent.

4.3.3 C-V Characterization

The C-V characterization is conducted with a prober station. The measurement is conducted with Keithley SMU 2400 which connected to Keithley 4205 REMOTE Bias-Tee. The data is processed using Keithley 4200-SCS Semiconductor Characterization System. Measurements of the capacitance at different frequency, 100 kHz, 1 MHz, and 10 MHz are conducted. The result of C-V characterization indicates that the capacitance of the MIM diamond sample is in the range of 0.5 – 0.6 pF depend on the input signal frequency. However, for a single frequency measurement, the capacitance is constant for bias voltage 0 to ±30 V (figure 4-11). The constant capacitance of the detector may come from an extremely low carrier concentration. The condition makes a low bias voltage already extend the depletion layer over all area of the crystal. The fully depleted condition over any range of bias voltage implies the capacitance is independent of bias voltage.
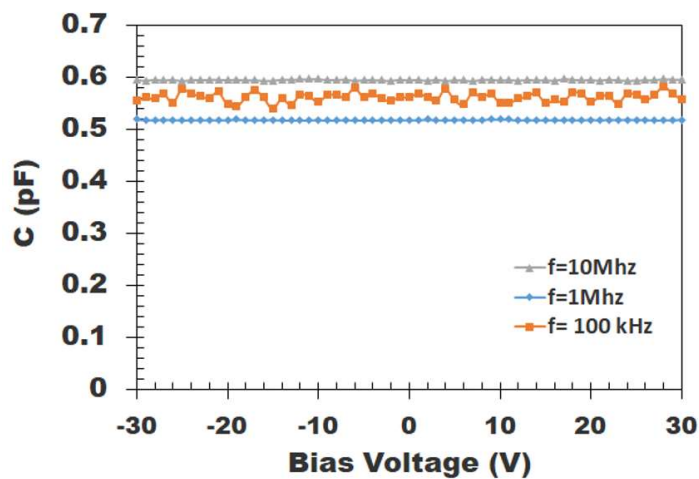
Figure 4-11. The value of capacitance as function of Bias voltage in three different AC frequency evaluation signal.

4.3.4 Transient Current Technique

The results of TCT measurement is conducted with a fast current-sensitive amplifier with voltage signal as the output. The voltage signal is averaged to get rid of random noise part. The voltage signal is converted to current signals as shown in figure 4-12 by equation:

$$i_{e,h}(t) = \frac{1}{R_{in}A}\left[R_{in}C_d\frac{dU(t)}{dt} + U(t)\right], \tag{4.3}$$

with $i_{e,h}(t)$ is electron or hole current as function of time, R_{in} is of input resistance of amplifier of 50 Ω, A is voltage gain of amplifier that has a value of 13, C_d is the detector capacitance of 0.6 pF and U(t) is voltage as function of time.

By fitting the leading edge and trailing edge of the signal, the drift time of the carrier can be calculated. The fitting is carried out using Error function in ROOT. The drift time of the charge carrier leads to the drift velocity of the charge carrier as function of electric field:

$$v_{dr}(E) = d/t_C , \qquad (4.4)$$

with E is electric field, v_{dr} is drift velocity of carrier, t_c is drift time of carrier and d is thickness of diamond sample which is 500 μm.
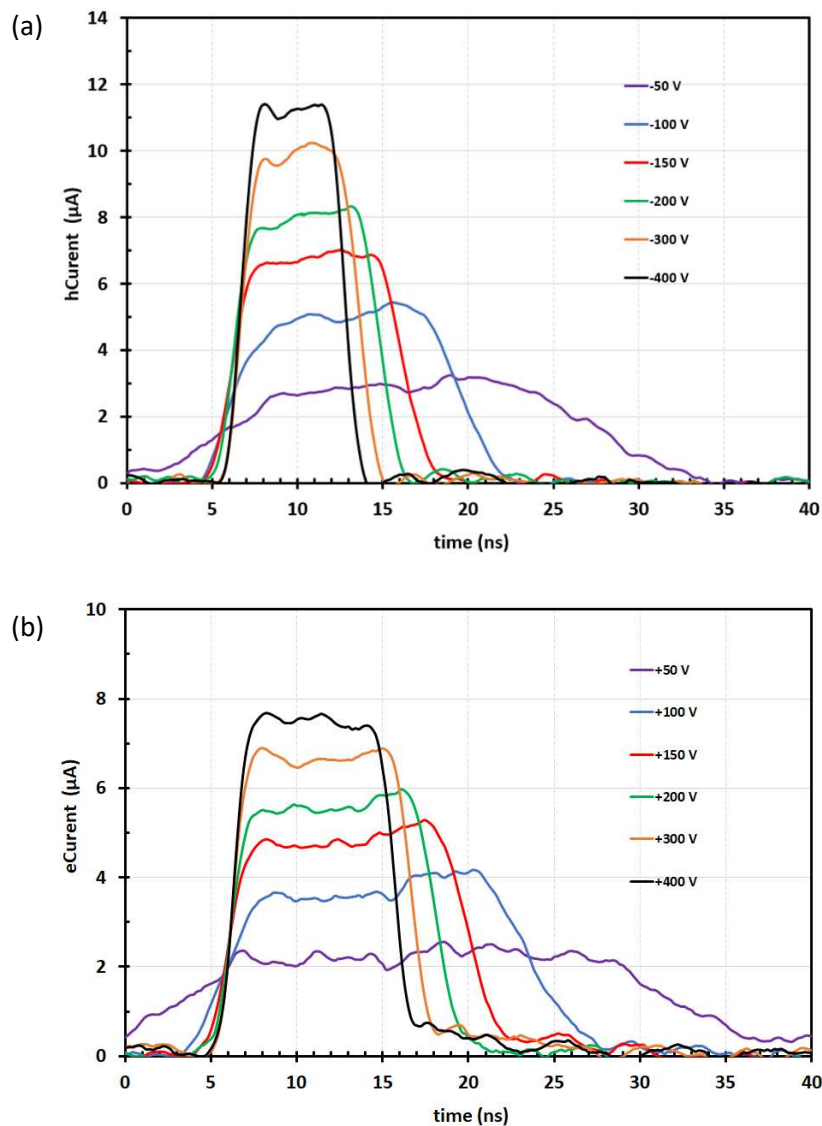
Fig. 4-12. The transient signal as α-particle penetrates MIM device. (a) Hole current (b) Electron current.

The velocity of the carrier will increase slowly under high electric field as shown in figure 4-13. The empirical approach to explain this phenomenon is saturation velocity model as:.

$$v_{dr} = \frac{\mu_0 E}{1 + \frac{\mu_0 E}{v_S}} \quad , \tag{4.5}$$

with E is electric field, v_{dr} is drift velocity, μ_0 is low-field mobility, and v_s is saturation velocity.

By fitting the drift velocity to the electric field with the saturation velocity equation, the value of mobility and saturation velocity of diamond detector can be acquired. The fitting results in the value of hole mobility is 2559 ± 33 cm^2/V.s and saturation velocity of hole is (1.35 ± 0.02) x 10^7 cm/s. On the other hand, the value of electron mobility is 2204 ± 32 cm^2/V.s and saturation velocity of electron is (0.76 ± 0.01) x 10^7 cm/s.
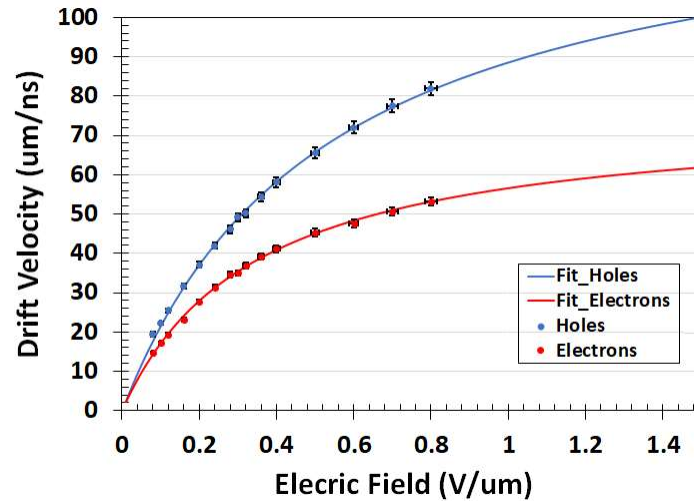
Figure 4-13. The fitting of mobility and saturation velocity of hole and electron in MIM Diamond detector.

For further characterization, the value of lifetime can be calculated by using the data of transient current measurement. By using Hecht's equation:

$$\frac{Q}{Q_0} = (\frac{\tau}{t_{tr}}) \cdot (1 - exp^{-t_r/\tau}), \tag{4.6}$$

where the CCE can be fitted as function drift time. The variables in the equation consist of Q/Q_0= CCE, t_{tr} for drift time of carrier, and τ for lifetime of carrier. The fitting of CCE versus drift time of carrier results in the lifetime of electron (169 ns) and the lifetime of the holes (490)

ns. The values of mobility, saturation velocity and lifetime of the carriers are comparable with the references as shown in table 4.1 except for the last reference. Unlike the other references that use the saturation velocity formula (eq. 4.5), Kassel fits the velocity as function of electric field by using Caughey-Thomas approach [Cau67]. The approach tends to overestimate the mobility value from a sets data points that are basically comparable to the data belongs to the other references.

Table 4.1. Comparison of the mobility, saturation velocity and lifetime of the carriers of high quality single crystalline CVD diamond sample in this study to the references who use the same type of diamond sample [Per05, Pom05, Gab08, Kas16].

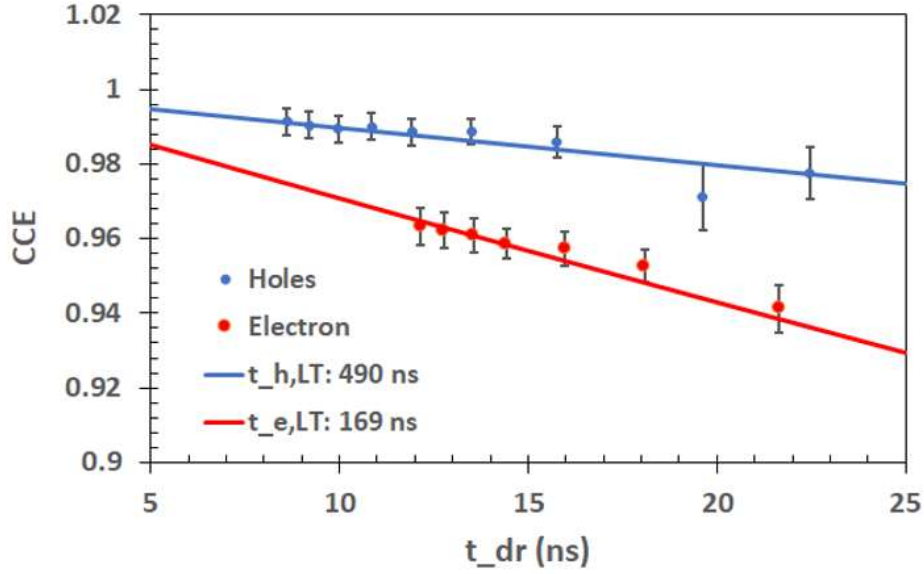|	μ_0 – Low Field Mobility (cm²/Vs)	v_s – Saturation Velocity (cm/s)	τ – Life Time (ns)
This study			
Electrons	2205	7.6×10^6	169
Holes	2559	13.5×10^6	490
Pernegger, 2005			
Electrons	1714	9.6×10^6	33.8
Holes	2064	14.1×10^6	35.8
Pomorski, 2005			
Electrons	2071	8.5×10^6	174
Holes	2064	14.1×10^6	968
Gabrysh, 2008			
Electrons	2760	-	-
Holes	2750	-	-
Kassel, 2016			
Electrons	9793	45.0×10^6	-
Holes	2661	15.4×10^6	-

Figure 4-14. The fitting of carrier life time using Hecht's equation. The error-bars represent the Gaussian distribution of Alpha particle peak histogram

To construct a reliable model using TCAD simulation program, all of the important parameters of a high-quality diamond sample need to be obtained. However, one more crucial parameter is needed, the carrier density inside the diamond bulk. The value of carrier density can be clarified by fitting of electric distribution inside the diamond crystal. The distribution of electric field can be derived from an equation that shows the relation between transient current and drift velocity of carrier as shown by:

$$I = \frac{Qv}{d} \quad , \tag{4.7}$$

with I is transient current, Q is total generated charges, v is drift velocity of charge carrier, and d is the thickness of the sample. By substituting the drift velocity in equation 4.7 to equation 4.5, a new equation is obtained to give information about the relation of electric field (E) and specific position inside the diamond bulk (x) as [Isb06]:

$$x = \int_0^t v \, dt = \frac{d}{Q} \int_0^t I \, dt , \tag{4.8}$$

$$E = \frac{1}{\mu \left(\frac{Q}{dI} - \frac{1}{v_s} \right)} \quad . \tag{4.9}$$

In the previous discussion the value of mobility (μ) and saturation velocity (v_s) were already acquired. The parameter Q is the total generated charge. The value of this parameter can be obtained from an integration of the transient current signal. The average value of the integration is 67 fC. By solving these analytical equations, the distribution of the function of carrier concentration can be attained. Using equation 4.8 and 4.9, the current signal as a function of time can be converted to graph of electric field distribution as a function of position inside the diamond bulk. Comparison between the analytical distribution of the electric field and the graph derived from transient current (figure 4-15) concludes the analytical distribution of electric field of diamond that has carrier concentration of 1×10^{10} /cm^3 represent the experimental data better than the one with carrier concentration of 1×10^{11} /cm3.
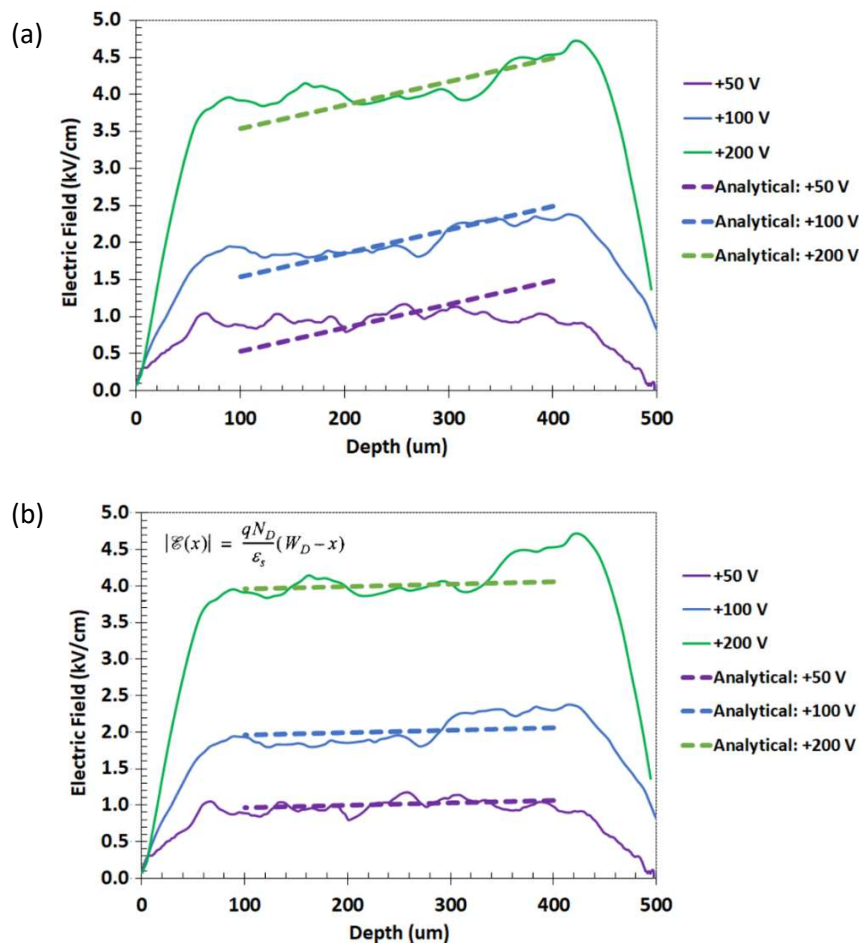
Figure 4-15. Fitting of the distribution of electric field as function of position inside the MIM diamond sample. Solid line is distribution electric field derived from experiment data. Dashed lines are analytical distribution of electric field for (a) carrier concentration n_h: 1×10^{11} /cm^3 and (b) n_h: 1×10^{10} /cm^3.

4.3.4 Depth of Depletion Layer

Energetic beta particle can penetrate the thick crystal of diamond. From calculation by using Bethe's equation, beta particle with energy > 0.5 MeV penetrate 500 μm thick diamond bulk. In this experiment ^{90}Sr emits beta particle with energy 0.4-2.2 MeV. The peak of spectra is around 1 MeV. Therefore, the beta particle can penetrate the MIM diamond detector.

The CCE of β-particle is acquired by comparing the peak position of energy deposition by β-particle and the peak position of deposition energy of alpha particle in diamond crystal (figure 4.16). The measurement is conducted under high bias voltage to ensure the maximum charge is generated by both particles. This comparison concludes maximum energy deposited by beta particle in MIM diamond detector under -100V bias is 230±33 keV. By assuming the ehp creation energy is 13.1 eV, the maximum of generated charge can be calculated as 2.80±0.4 fC. By the assumption, the generated charge by β-particle as a function of bias voltage is shown in figure 4-17.

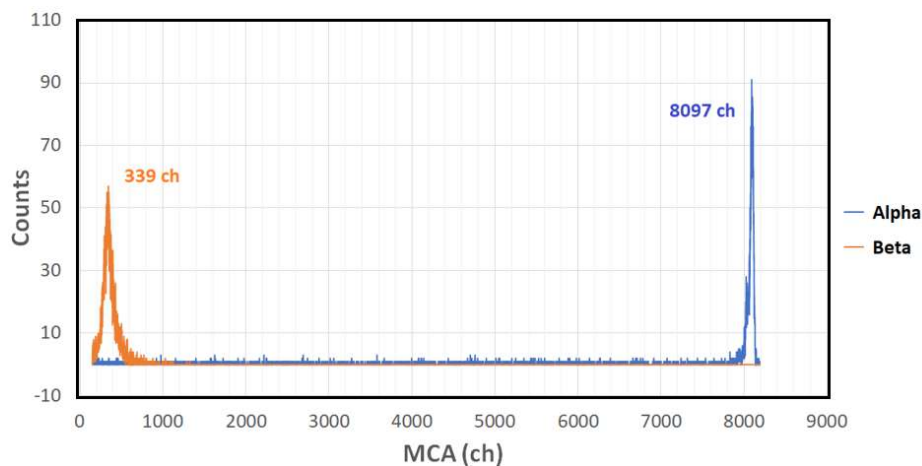Figure 4-16. Comparison of the peak position of deposition energy by β-particle and peak position of deposition energy of the α-particle in the diamond sample under -100 V bias.

Based on the Ramo's theorem, an energetic particle only generates signal if it creates ehp in region that is covered by electric field. Therefore, β-particle which is considered as Minimum-Ionized-Particle (MIP) can be used to study the depth of depletion layer by evaluating the generated charges in the thick MIM diamond sample. By converting the generated charge as function of bias voltage to the depth depletion layer by using MIP conversion constant of Q_{MIP}: 57.67×10^{-7} pC/μm [Mor16], the information about the depth of depletion layer can be acquired.

By the conversion constant, depth of depletion layer ≈ 500 μm can be achieved by bias voltage of |V| ≥ 20 V. By applying carrier concentration of 1 x 10^{11} /cm^3 in TCAD simulation, the experimental data can be reproduced quite well (figure 4-17a). However, if CCE from α-particle experiment is taken into account, the generated charge of in the low bias condition is higher (figure 4-17b). Therefore, the carrier concentration should be less than 1 x 10^{11} /cm^3.
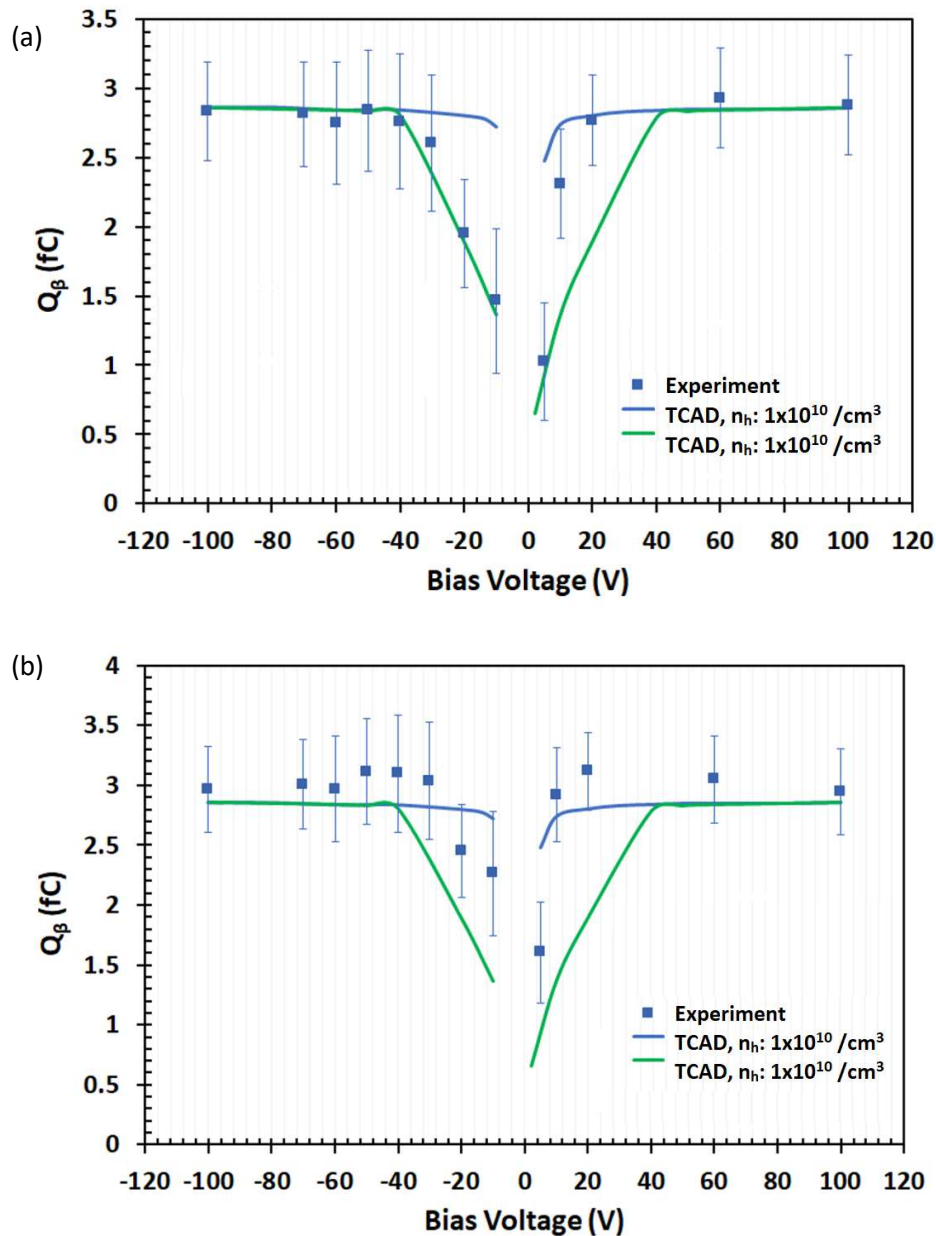

Figure 4-17. (a) Experimental result of generated charges by β-particle from ^{90}Sr. The blue (green) line is simulation result of β-particle in diamond detector with carrier concentration of 1 x 10^{10} /cm^3 (1 x 10^{11} /cm^3). (b) The generated charge by β-particle after a calibration with CCE of α -particle.

4.4 Other Samples

In order to validate the simulation model, two other diamond sample is evaluated. The first is Cividec MIM 140 μm diamond detector placed inside a metal case by the manufacturer as shown in figure 4-18a. The Cividec diamond is believed to be a single-crystalline CVD diamond. The metal contact for the sample is gold contact for both sides. The second is NDT MIM 500 μm diamond detector as shown in figure 4-18b. the NDT sample is a high-quality mono-sectoral High-Pressure High-Temperature (HPHT) sample with a low Boron Doping concentration. The SIMS measurement (figure 4-19) shows that the Boron concentration is 10^{14} /cm^3, the measurement limit of SIMS. The metal contacts of NDT sample are circular Titanium/Molybdenum (Ti/Mo) on both sides.
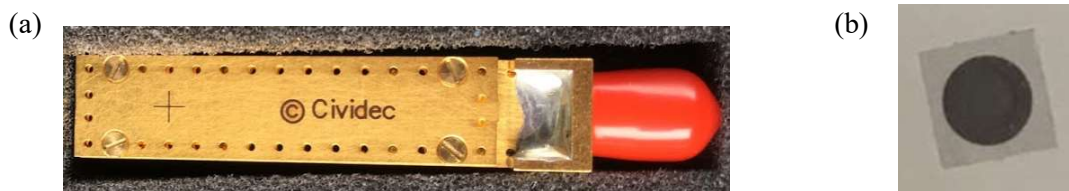
(a)   (b)

Figure 4-18. (a) The picture of Cividec detector inside metal case. (b) The picture of NDT diamond sample.
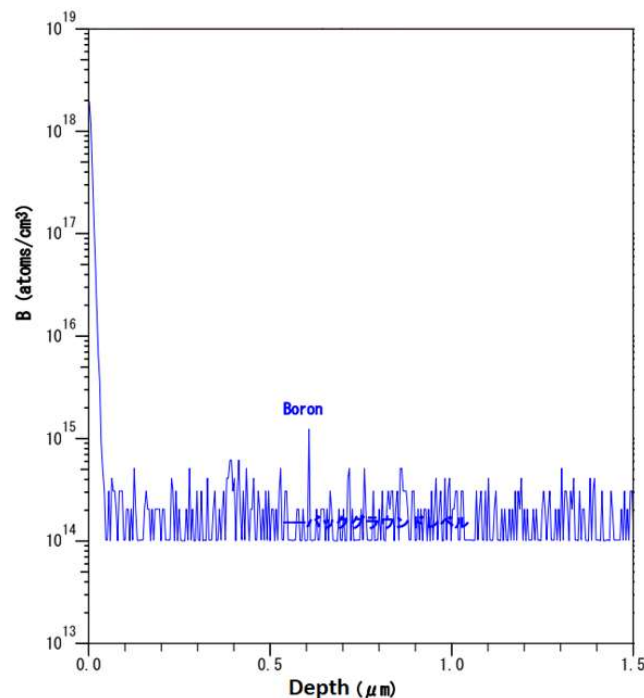

Figure 4-19. The Boron concentration measurement result of Secondary Ion Mass Spectroscopy (SIMS) in NDT sample.
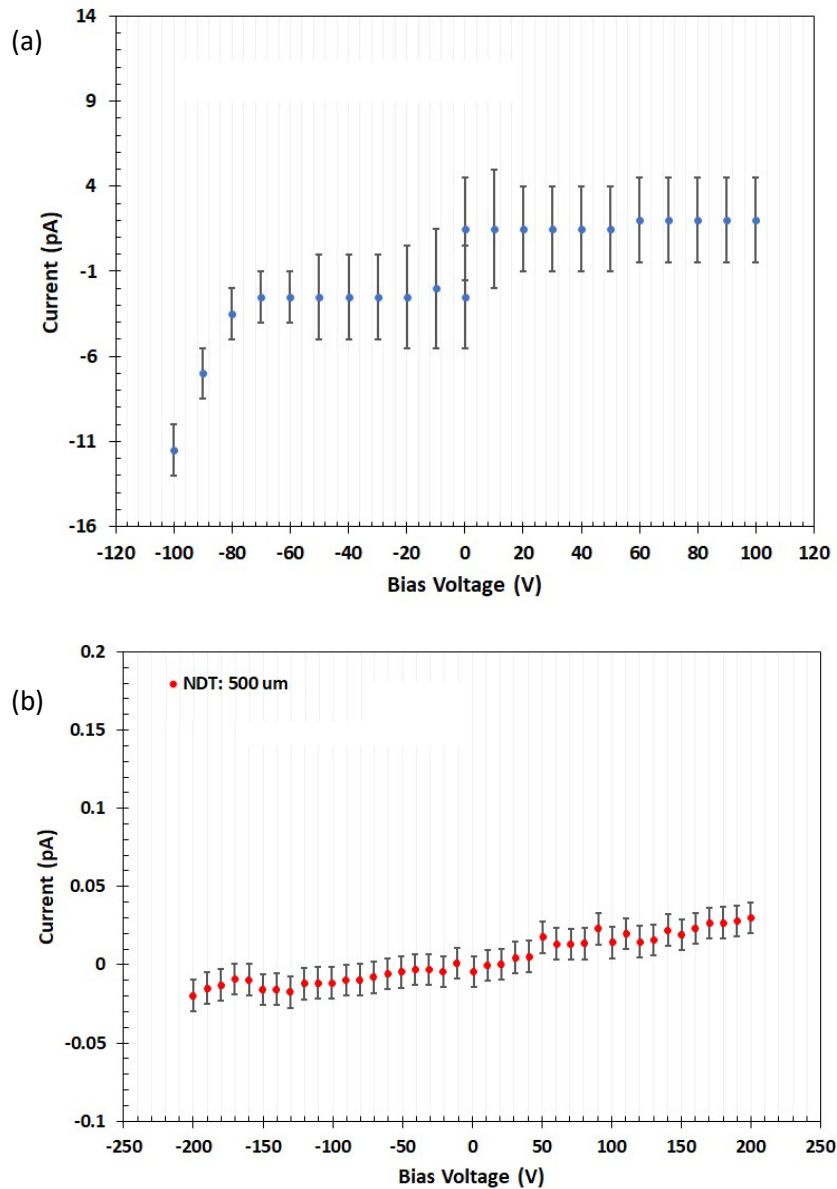
Figure 4-20. I-V characteristic of (a) Cividec diamond sample and (b) NDT diamond sample.

To evaluate the quality of the metal contact and the diamond crystal, the I-V characterization is conducted for both samples. The I-V characteristic of Cividec sample is measured inside a vacuum chamber with Keithley 2450 SMU (figure 4-20a) at room temperature. On the other hand, the I-V characteristic of NDT sample is measured with a prober station in ambient air at room temperature. Both I-V characteristic are measured in a different setup due to the restriction from the casing of Cividec sample. Therefore, the I-V characteristic of NDT sample is significantly lower than that of the Cividec sample (figure 4-20b). Direct connection between the SMU and diamond case generates significant leakage current that overwhelm the extremely low dark current of diamond detector. However, both of the sample shows small leakage

current for both voltage bias polarity. It indicates both metal contacts for those samples have significant Schottky Barrier.

The CCE measurement by using α-particle is conducted to both of the samples. The maximum CCE of Cividec sample is about 95%, slightly below the maximum value achieves by ElementSix sample as shown in figure 4-21a. The high CEE indicate that the quality of the diamond crystal and metal contact fabrication are excellent. On the Other hand, the CCE of NDT sample is quite low. From the previous measurement, it is known that the CCE of ElementSix sample is around 96%. Thus, the relative position of the ADC peak channel in figure 4-21b can be used to find the CCE value of NDT sample. The CCE value of the sample only about 20% under 200 V bias. The low CCE indicates problems in metal contact fabrication or the abundant of defect in the crystal.
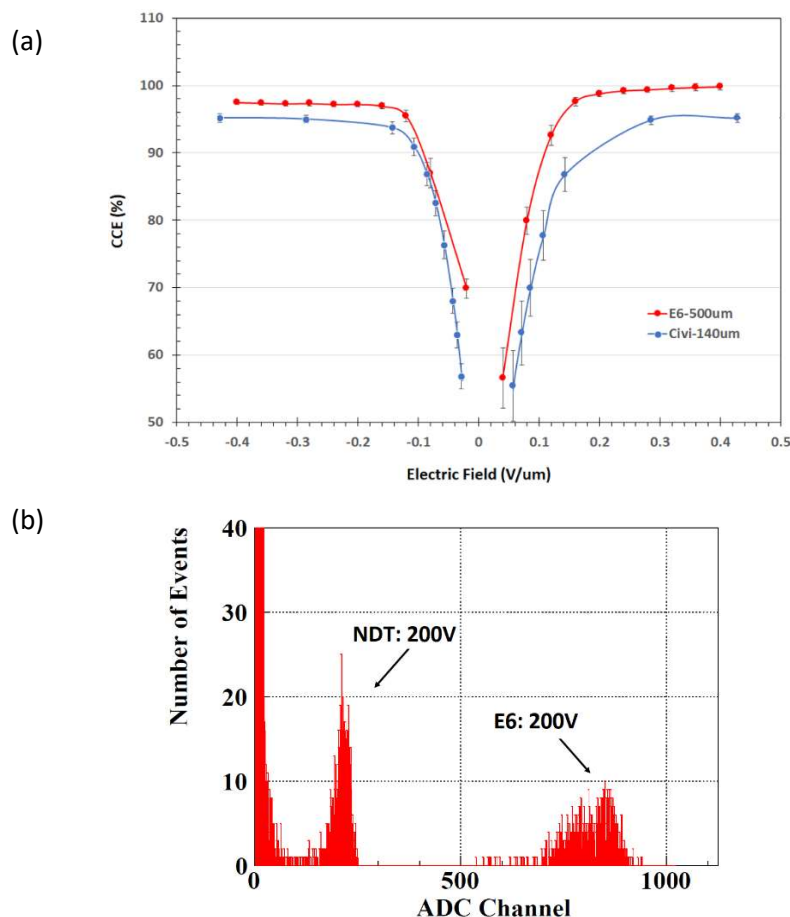

Fifure 4-21. (a) The comparison between the CCE of Cividec 140 μm and ElementSix 500 μm diamond detector. (b) The comparison of peak Analog to Digital Converter (ADC) channel of NDT 500 μm and ElementSix 500 μm diamond detector under 200 V bias voltage. The relative CCE value is reflected by the relative peak channel position of the NDT histogram.

Transient current signal from α-particle can be used to complement the CCE evaluation. The transient current is derived from a output voltage signal of Gali52+ Amplifier that are convert with equation 4.3 is shown in figure 4-22. The integration of the current signal corroborates the high CCE value of Cividec diamond. The thickness of Cividec sample is 4.2 times thinner than that of ElementSix sample, therefore the drift time of charge carries is expected to be inversely proportional to the thickness under high electric field condition. However, the leading edge risetime and trailing fall-time of signal dominates the signal. It makes the drift time of carrier is only around three times shorter than that of ElementSix sample which is longer than expected. Hence, the domination of leading and trailing edge timing results in the measurements of carrier charge mobility and lifetime based on the transient signal of the thin sample is less ideal than those of a thicker sample.
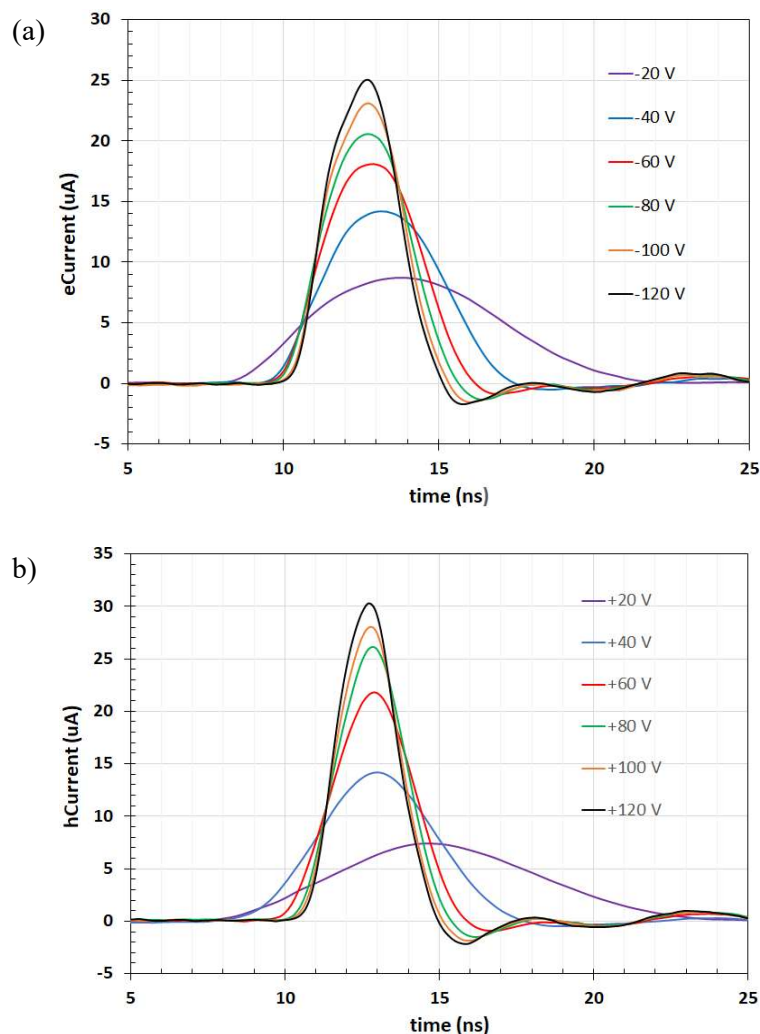

Figure 4-22. The transient current of Cividec diamond sample from (a) electrons, and (b) holes.

If the mobility of charge carrier is defined similar with a thicker sample, the drift time is measured based on the mid-timing of leading edge and trailing edge of the signal. The mid-timing is defined with an error-function at leading edge and trailing edge of the signal as shown in figure 4-23. The subtraction results of the mid-timing of trailing edge and the leading edge defines the drift-time of the charge carrier. With equation 4.4, those drift times are converted to the drift velocities of the carriers. Based on the information, drift velocity can be plot as function of electric field as shown in figure 4-24.

(a)

Cividec-Dia: +60 V, Amp.: Gali52+

Mean: 11.38 +/- 0.01 ns
Sigma: 0.84 +/- 0.01
MFactor : 11.32 +/- 0.03
yConstant : 0.06 +/- 0.004

(b)

Cividec-Dia: +60 V, Amp.: Gali52+

Mean: 14.32 +/- 0.02 ns
Sigma: 0.79 +/- 0.02
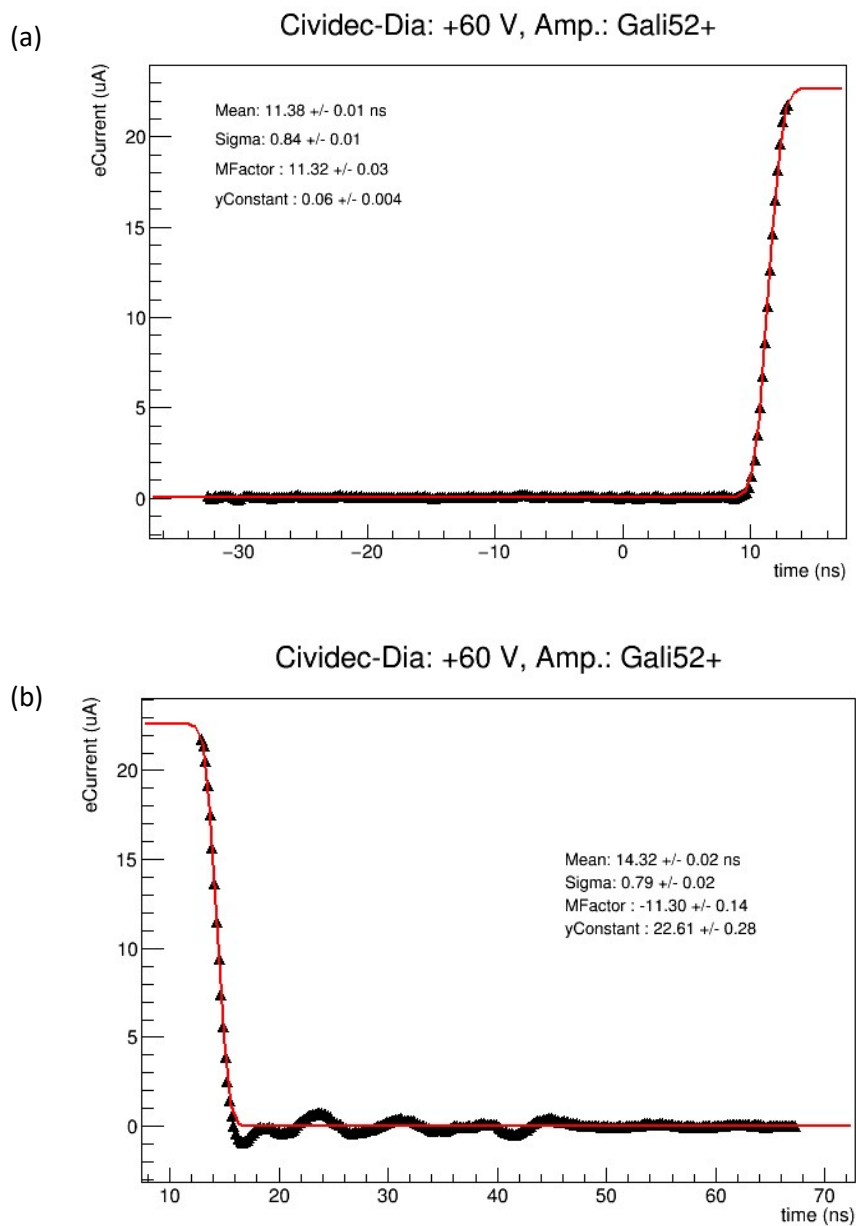MFactor : -11.30 +/- 0.14
yConstant : 22.61 +/- 0.28

Figure 4-23. The fitting of error-function at the leading edge and trailing edge of the Cividec transient signal under +60 V bias voltage.
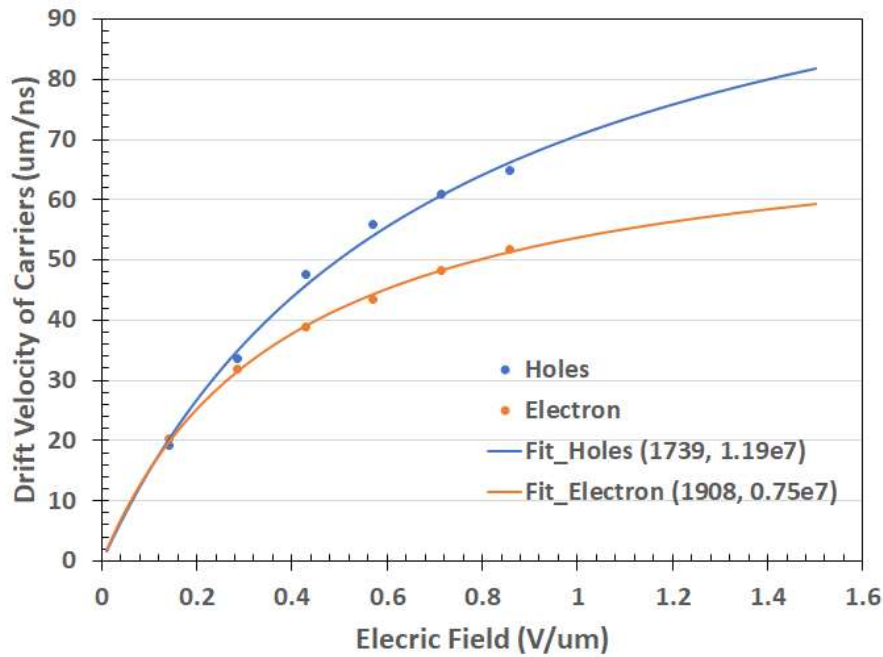
Figure 4-24. Plot of the drift velocity of charge carrier as function of Electric field for Cividec diamond sample.

The fitting of drift velocity as function of electric field with the saturation velocity model (equation 4.5) results in the charge mobility and saturation velocity value. For Cividec sample the mobility of holes (electrons) is 1739 cm^2/V.s (1908 cm^2/V.s). On the other hand, the saturation velocity of holes (electrons) is 1.19 x 10^7 cm/s (0.75 x 10^7 cm/s). The lower values of both parameters compared to the values of ElementSix sample can be understood due to the lower overall CCE value in any range of electric field as shown in figure 4-21a. On the hand, the non-ideal character of the thin Cividec sample may also give some disadvantage of less validity to use the saturation velocity model to calculate the carrier mobility and saturation velocity.

The transient current of the NDT sample confirms the low CCE measurement is shown in figure 4-24. The integration of current result around 10% of total charge created by 5.486 MeV α-particle in the other high-quality scCVD diamond crystal with similar thickness even under high bias voltage of ±400 V. The signal period also quite short for 500 μm sample that indicate short drift time of carrier. The SIMS measurement suggests that the sample has extremely low boron concentration. Therefore, electric field should be sufficiently high and uniform under high bias voltage to result in high CCE. The most possible reason of the low CCE is the high density of additional energy levels inside diamond bulk which behaves as traps that capture the

drifted charge carriers. Beside the capturing the charge, the trap levels can also deform the distribution of electric field inside the diamond bulk which deteriorate the shape of the transient signal [Kas16].
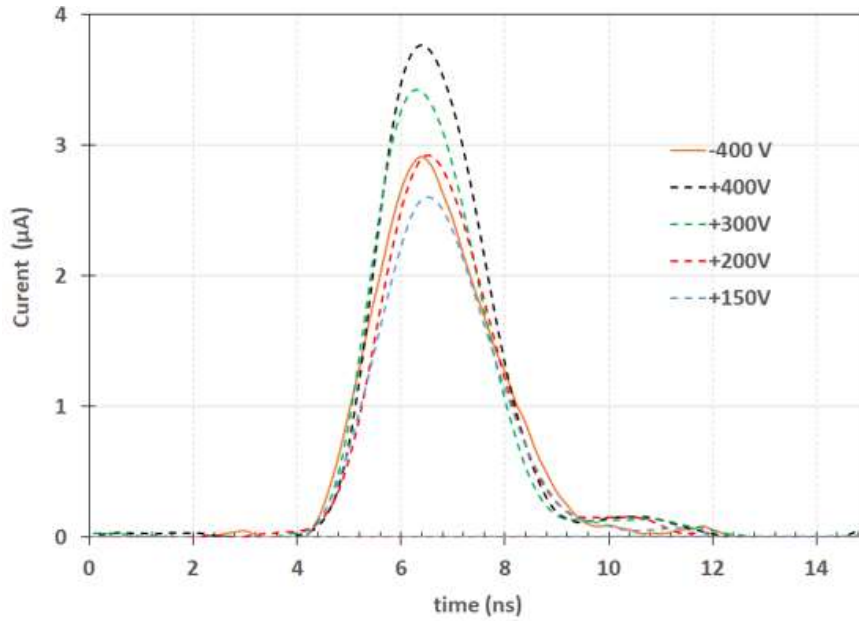

Figure 4-24. The transient current of NDT sample.

Chapter 5

Numerical Parameterization of Diamond Crystal

TCAD simulation works by calculation of three basic equation, i.e., Poisson equation, drift-diffusion transport equation and Continuity equation in finite elements for specific device geometry. However, each equation requires involving some models to finish the calculation, e.g., model that explains the number of active carriers, the mobility of carries, generation-recombination parameter and avalanche parameter. The model used in the TCAD simulation is based on Brezeanu work [Bre07-2] with modifications of some parameter values. Two properties that dictate the electric characteristic significantly in the diamond device simulation are the density of active carrier and charge carrier mobility.

All simulation in this work is made in a 2D approach. 3D simulation can simulate more realistically, but it requires enormous computing power and much longer time to result in convergent outputs. The charge concentration in this simulation follows the characterization result in previous chapter which is 10^{10} /cm^3. The value can reproduce reasonable I-V characteristic of MIM diamond especially in the reversed bias the simulation result can fit the data quite well. Furthermore, the transient simulation results also match quantitatively with experimental results. The results of simulations are divided into two parts. First part is simulations of MIM mainly to test the reliability of TCAD simulation in reproducing the experiment data. the thickness of Cividec sample is 4.2 times thinner than that of ElementSix sample

5.1 Carrier Concentration

The intrinsic carrier concentration of diamond is extremely low in room temperature, in the order of 10^{-27} /cm^3. However, in a real intrinsic diamond crystal, the carrier concentration suggested by manufacturer is much higher than the theoretical intrinsic value because in CVD process used to fabricate diamond crystal, Boron and Nitrogen are common impurities incorporated unintentionally. Boron as the shallowest acceptor for diamond gives the crystal hole carrier. Furthermore, as the effect of the deep energy level of doping, the number of activated carriers can be significantly fewer than given doping concentration especially for a

diamond with a high doping level (> 10^{13} /cm^3) [Ras08]. Hence, calculation precise carrier concentration in a diamond device requires the involvement of incomplete ionization model. In this TCAD simulation, the level of ionized carrier density in diamond is derived from the modified Fermi-Dirac distribution [Ras08].

The activation energy of holes from boron acceptor depends on its concentration [Ras08]. On the other hand, the activation energy of electrons from phosphor donor do not show any decrease up to 10^{19} /cm^3 concentration [Mar14]. In the prior studies, the lowest implemented boron doping concentration in TCAD simulation to study diamond device with intrinsic crystal is in the order of 10^{11} /cm^3 [Ras08, Bre07, Mor16]. The reason of 10^{11} /cm^3 boron concentration implemented is that the TCAD numerical calculation can be done quite easily without many convergence issues of the numerical calculation.

The leakage current is function of carrier concentration (Figure 5-1). By prior diamond MIM characterization by beta particle, the value of carrier concentration should be less than 10^{11} /cm^3. The calculation of electric distribution conclude data reproduce better if analytical distribution of electric field has carrier concentration 1 x 10^{10} /cm^3. Therefore, in this work, the n_h: 1 x 10^{10} /cm^3 is implemented to the TCAD simulation.
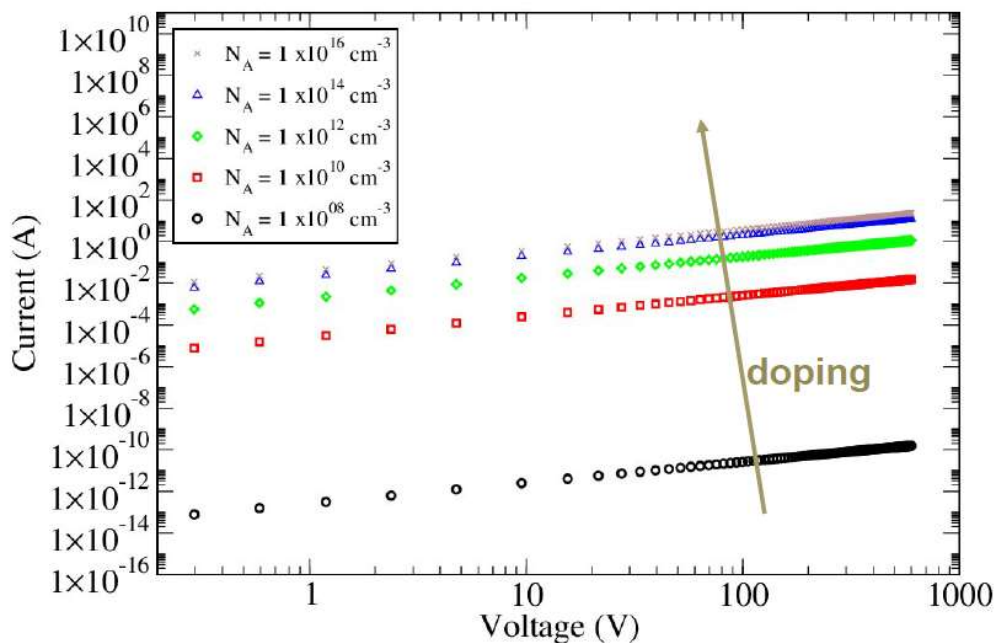

Figure 5-1. The dependency of Leakage current to carrier concentration [Mor].

5.2 Mobility of Carrier

For the mobility model, this study uses a default model suggested by TCAD Sentaurus based on a formula proposed by Masetti et al. [Mas83]. The maximum mobility values record by a reference for diamond at room temperature are 4500 cm^2/V.s for electron and 3800 cm^2/V.s for holes [Isb02]. The experiment was conducted with Transient Current Technique (TCT) in 2002. However, the value cannot be reproduced by other experiments using TCT technique or Hall-effect method. The more recent experiments result in significantly lower mobility for both hole and electron [Per05, Pom05].

The TCT characterization was used to obtain the mobility of holes of 2559 cm^2/V.s and mobility of electron of 2205 cm^2/V.s. Those mobility value corroborates the prior measurements of carrier mobility in some diamond device with high quality single crystal. Thus, the value can be implemented to the next simulations to design a new diamond detector. The values of saturation velocity acquired from TCT characterization were also utilized. Furthermore, the value of lifetime for electron and holes of 169 ns and 490 ns, respectively, were also implemented in this simulation.

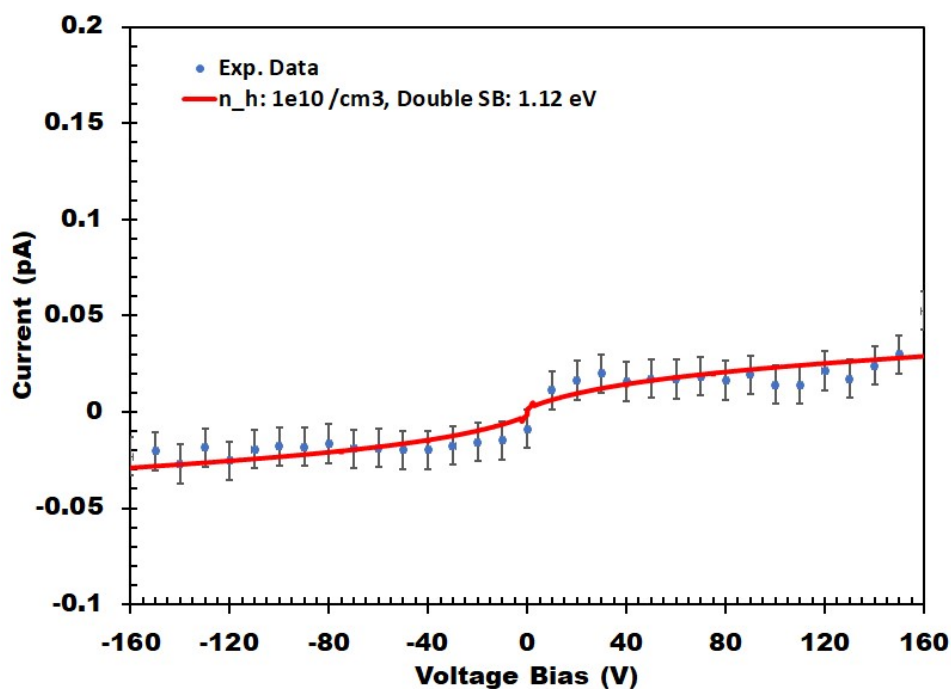## 5.3 Reproduction of Diamond Characterization Data

Figure 5-2. Reproduction of I-V Characteristic

Figure 5-2 shows that TCAD simulation can reproduce the reversed bias I-V characteristic of the MIM device quite well. Some references provide different value of Schottky Barrier at Aluminum and diamond interface, but the range is between 0.8 eV to 2.2 eV [Eva09]. Thus, for reproducing the data, we fit the value of Schottky barriers that can reproduce the data best. In this work, a Schottky Barrier of 1.11 eV is implemented for both Al-contact and Ti-Pt-Au contact. Moreover, with that configuration, the order of leakage current of TCAD simulation matches with experimental data in a high voltage forward bias, i.e., some tens of picoampere under 200 V forward bias or higher. The reason of high energy barrier on Ti-Pt-Au might be this metal configuration may have a more significant mismatch between Fermi level of metal and that of crystal. Different with my sample, the previous claims of the ohmic behavior toward Titanium metal as diamond device contact are since the crystal has significantly higher Boron doping, more than 10^{16} /cm^3 [Wan00, Tan06].

The model can reasonably reproduce CCE of diamond sample at high bias voltage, but the lifetime should be decreased to < 30 ns for both carriers to reproduce the data (figure 5-3). However, the implementation of the model to TCAD simulation also succeed to reproduce the transient signal of hole and electron quite well in the range of bias voltage from ±50 V to ±400 V (figure 5-4). Thus, this model performs are utilized to be a reference for development of a new diamond detector.
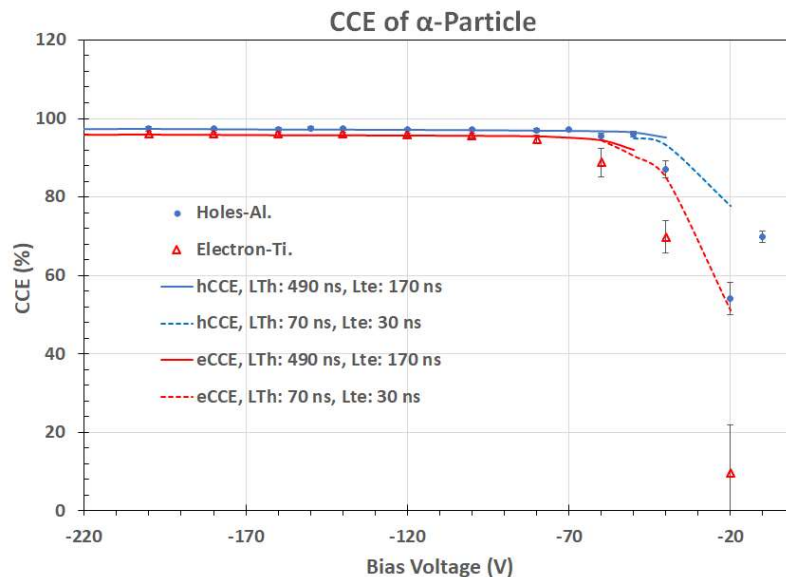

Figure 5-3. The model can reproduce the CCE value quite well at high bas voltage but it failed to reproduce the value of CCE for bias voltage < 60 V. By lowering the life time for holes and electrons to 70 ns and 30 ns (dashed-line), respectively, the model fits the data better for bias voltage < 60 V. The error-bars represent the FWHM of MCA histogram.
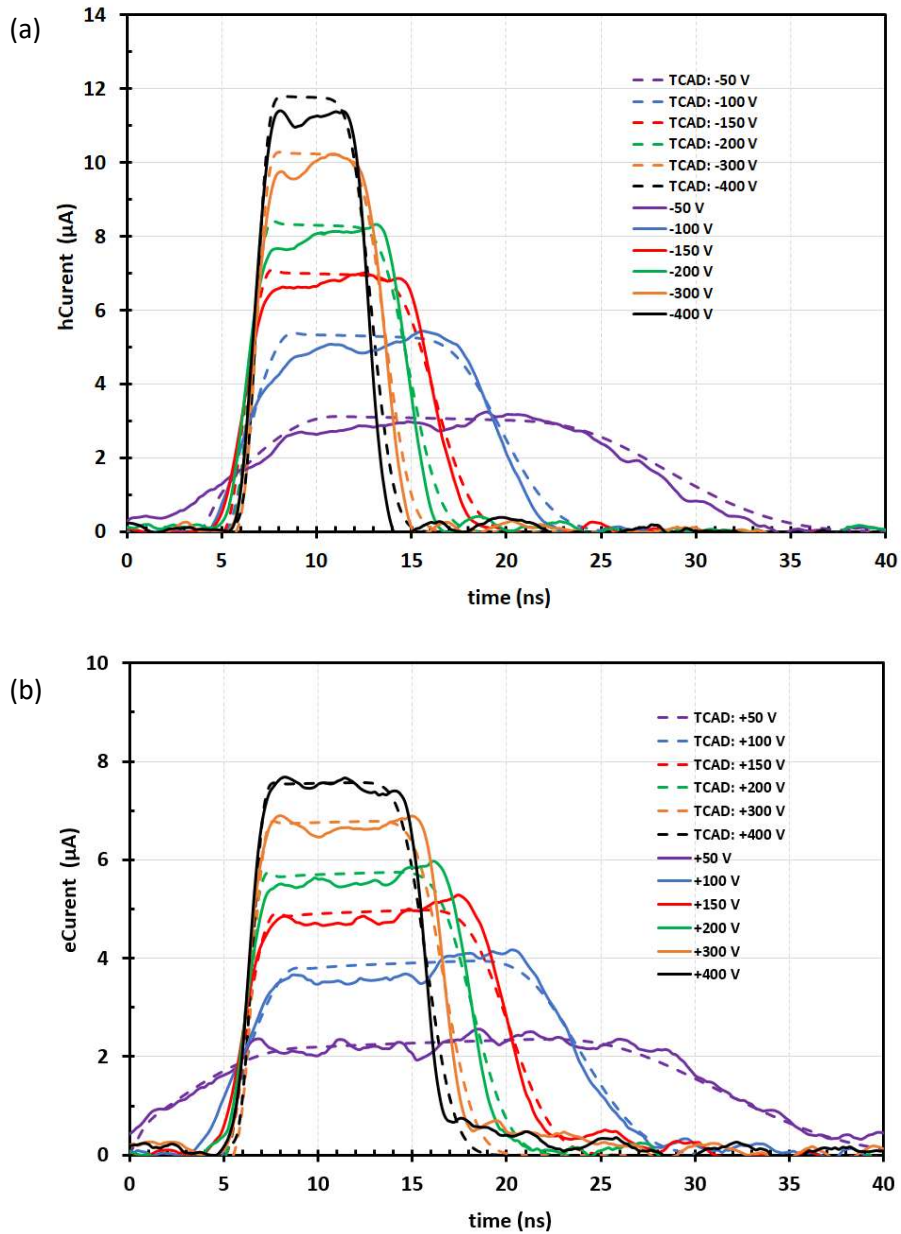
Figure 5-4. The model can reproduce the transient current for both (a) holes carrier (b) electron current quite well.

5.4 Other Sample

The model constructed from the evaluation of ElementSix sample is applied to reproduce the data acquired in other samples. The I-V characteristic is mostly defined by Schottky Barrier of the contact. The default value of Schottky Barrier (SB) obtained from the ElementSix sample is 1.15 eV. However, the variation of Schottky barrier (figure 5-5) result in a range of 1.10 eV – 1.15 eV that still excellently reproduces the data.
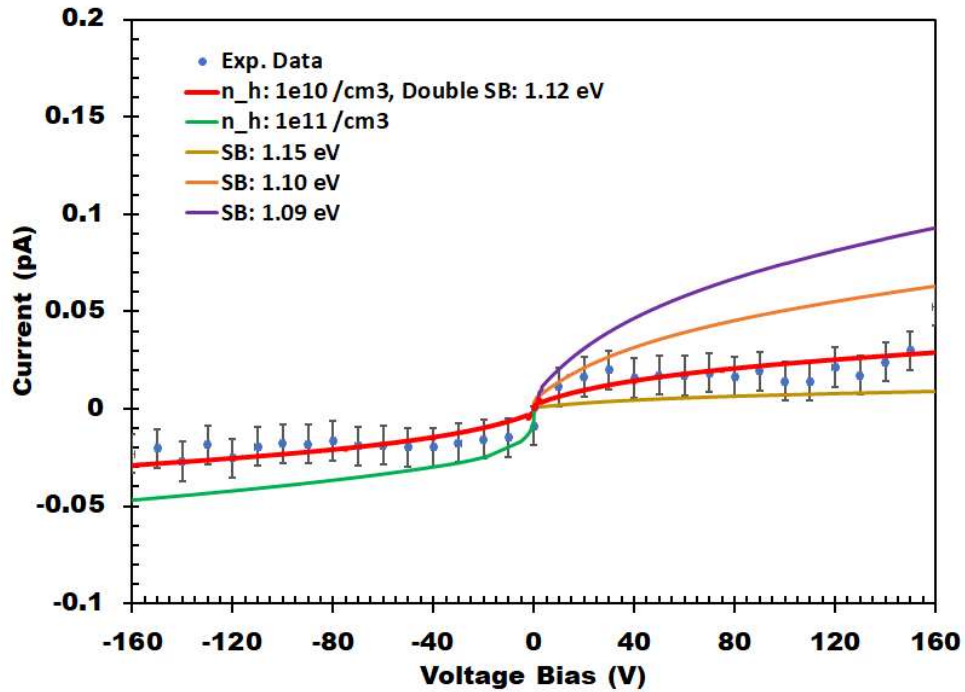
Figure 5-5. The variation of the carrier concentration and the Schottky Barrier of ElementSix sample.

The I-V characteristic of NDT sample as shown in figure 5-6a is best fitted with SB of 1.12 eV. The SB value is in the range of the default SB value obtained in ElementSix evaluation. Therefore, the Ti/Mo contact on the NDT crystal can be predicted has similar Schottky Barrier than that of Ti/Pt/Au and Al-contact on ElementSix sample. On the other hand, the I-V characteristic of Cividec sample can be well reproduced with SB of 0.95 eV as shown in figure 5-6b. The result is quite low compared to the value acquired with ElementSix sample. However, the different setup of I-V characterization of Cividec sample and ElementSix sample makes this direct comparison less valid.
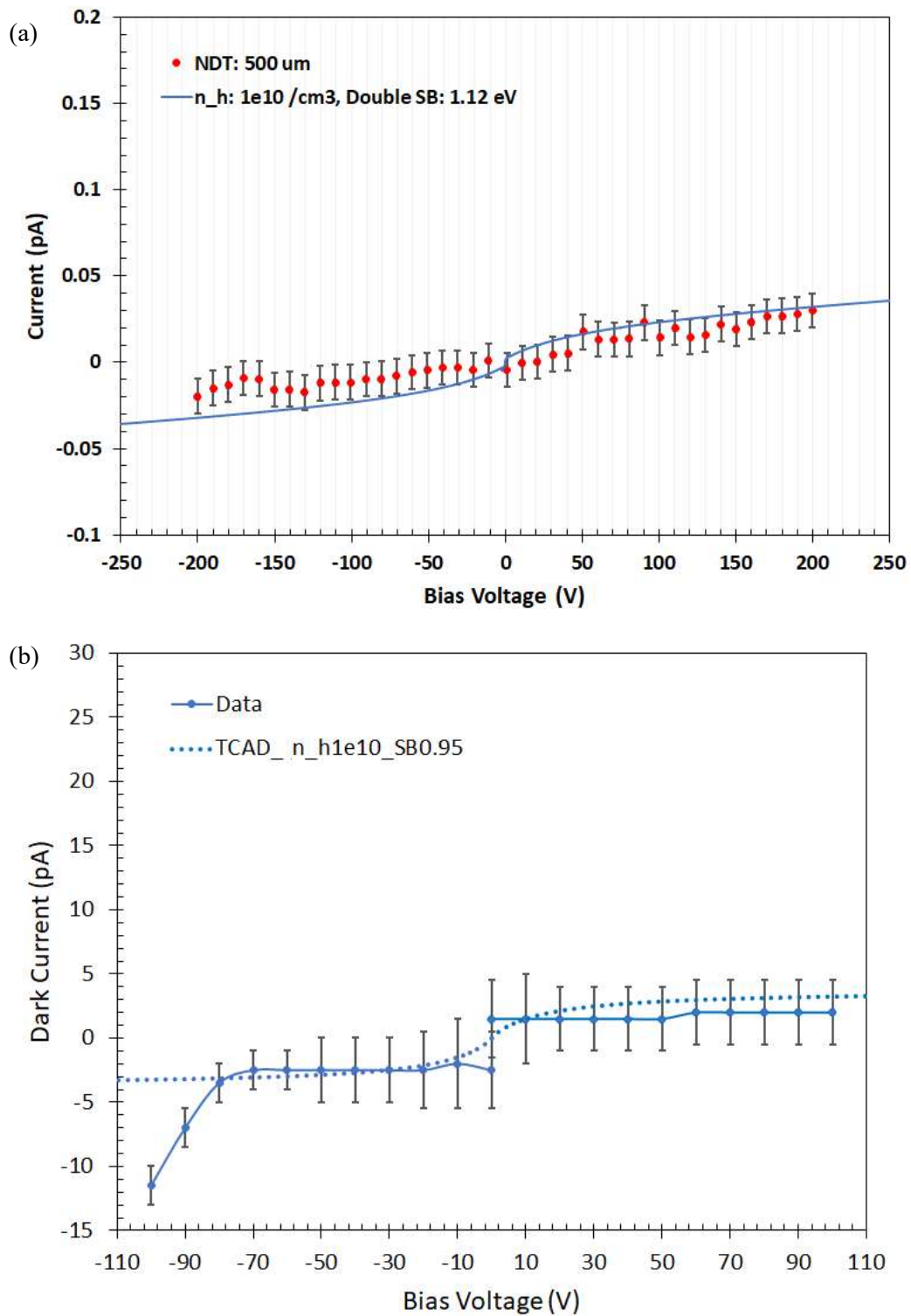
Figure 5-6. The Reproduction of I-V characteristic of (a) NDT sample reproduced by TCAD simulation with n_h: 1 x 10^{10} /cm^3 and SB: 1.12 eV and (b) Cividec sample by TCAD simulation reproduced by TCAD simulation with n_h: 1 x 10^{10} /cm^3 and SB: 0.95 eV.
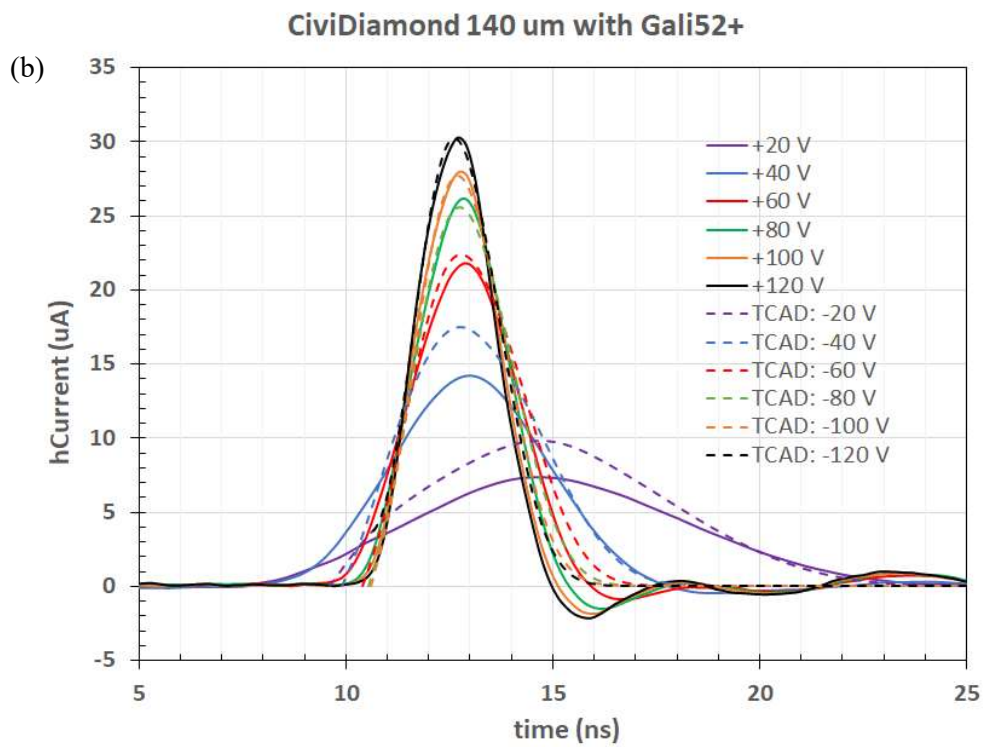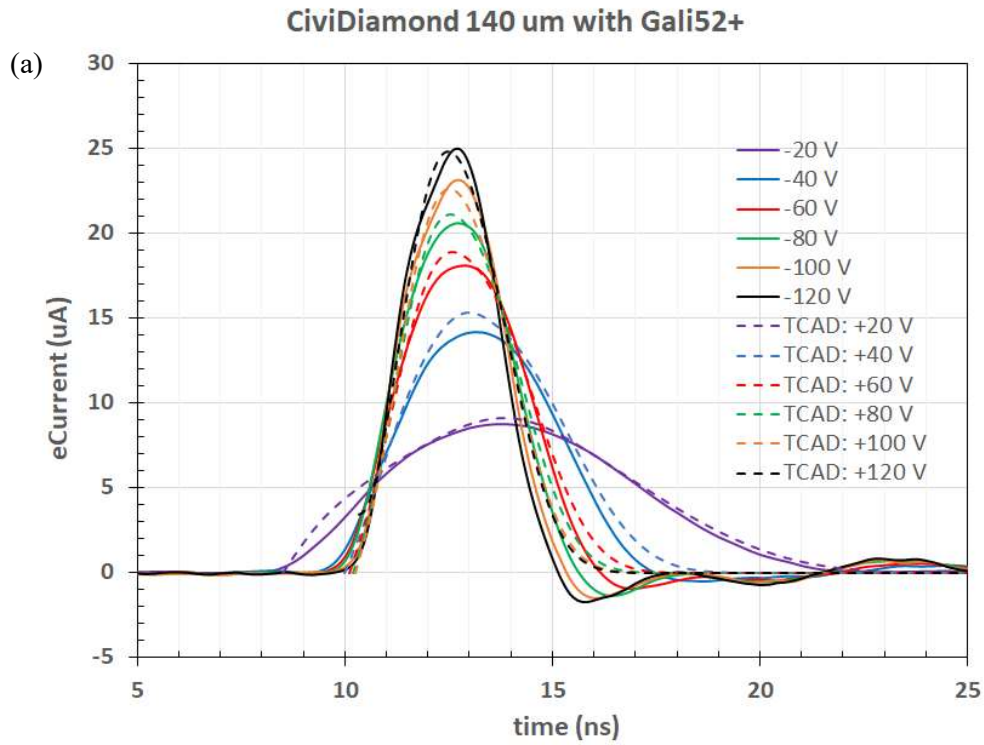
Figure 5-8. The reproduction of the transient current of (a) electrons and (b) holes in ElementSix sample.

The default value of simulation acquired from the ElementSix evaluation is applied to reproduce the transient current of Cividec sample except for the carrier mobility and saturation velocity. By applying the value acquired from Cividec evaluation with mobility of holes (electrons) is 1739 cm^2/V.s (1908 cm^2/V.s) and saturation velocity of holes (electrons) is 1.19 x 10^7 cm/s (0.75 x 10^7 cm/s) the transient current can be reproduced quite well (figure 5-8). Thereore, this model is quite versatile to evaluate the performance of any working diamond detector with few modifications based on the experimental evaluation of the diamond sample.

The transient signal of NDT sample cannot be reproduced with an ideal simulation model due to low CCE value. The short drift time of the charge carrier may indicate the absence of electric field in the deeper part of crystal or the fast recombination of charge carrier due to abundance of the defects that creates many traps level. A simulation of the transient signal by TCAD shows that a deep trap level of 0.83 eV from valence band and conduction band can reproduce the signal well as shown in figure 5-9. A uniform distribution of electric field can be expected inside a high quality intrinsic scCVD diamond sample under a high bias voltage (>50 V for diamond sample with thickness of 500 μm). However, the simulation result implies the trap levels deteriorates the distribution of electric field inside the bulk of diamond crystal. The low CCE suggests that the trap levels capture drifted carriers in a short time. The low-quality transient signal cannot be used to evaluate the mobility and saturation velocity of charge carrier in the NDT sample.
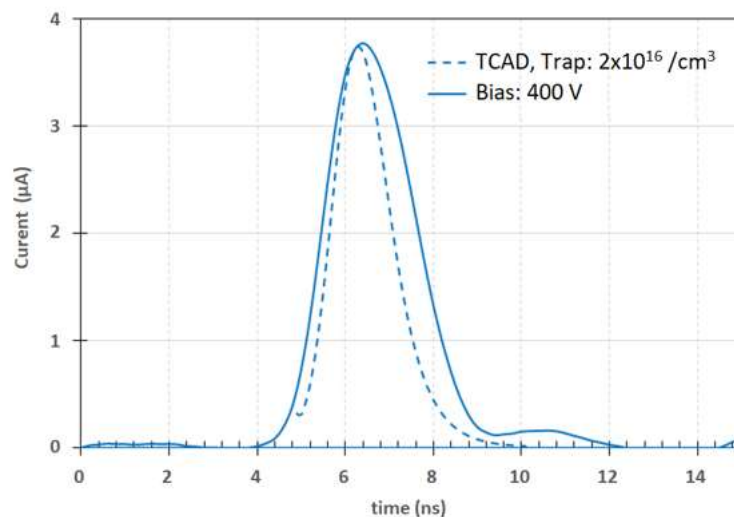

Figure 5-9. The reproduction of transient signal with TCAD simulation by implementing a donor (acceptor) trap level of -0.83 eV (+0.83 eV) from valence (conduction) band with electron cross-section and hole cross-section of 2x10^{14} cm^2 and 1x10^{14} cm^2, respectively.

Chapter 6

Design of a Diamond Detector with Signal Amplification

Based on the validation of TCAD model by using the MIM diamond, simulations were carried out to design a new diamond that may generate charge amplification effect. The main factor that enhance the charge amplification is a high electric field. McKay [Mck54] and Cynoweth [Cyn58] parameterize the charge multiplication by ionization coefficient α. The ionization coefficient reflects the generation of new charge per single charge per μm. The relation between the generated charges by multiplication effect and the ionization coefficient is shown as:

$$Q = \frac{Q_0}{1 - \int_0^d \alpha x \, \mathrm{d}x} \tag{6.1}$$

$$\alpha = ae^{-\frac{b}{E}} \tag{6.2}$$

with Q_0 is the charges that are generated merely by deposition energy of impinging particles. The parameter x reflects the path in which the charges are multiplied in high electric field region. Equation 6.2 expresses the relation between the ionization coefficient and electric field with parameter a and b are fitting parameters. In this work, a = 0.56 /μm and b = 219 V/μm are applied [Sku16].

Some prior studies indicate that a significant charge multiplication phenomenon occurs if electric field exceed certain value. In figure 6-1, some the theoretical calculations and experimental measurements propose different value of threshold electric field. However, one of the latest experiments suggests the threshold electric field is around 0.3 MV/cm [Sku16]. Therefore, we use the threshold value to design the new diamond detector.

In order to generate such high electric field, the intrinsic thick crystal with planar contacts is not suitable. The thick crystal requires extremely high bias voltage to reach sufficient electric field. In the thick sample, the defects are also more abundant, therefore the high bias voltage may also generate extremely large breakdown current. On the other hand, growing a high-

quality free-standing diamond crystal with a thickness < 15 μm [Kas16] is also not an easy task. Therefore, a diamond detector with needle-like structure is proposed to enhance the electric field (figure 6-2).
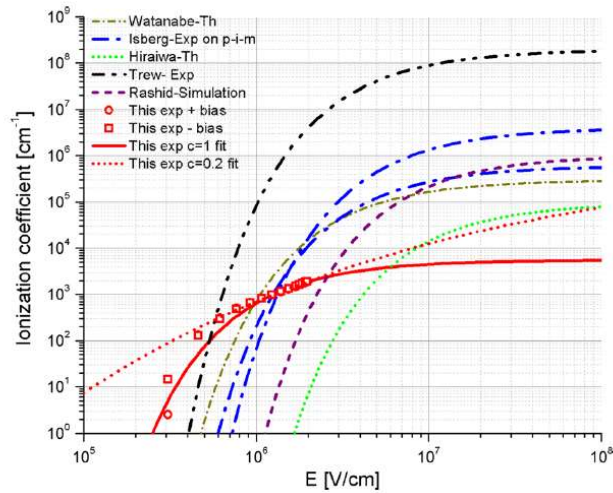

Figure 6-1. Ionization parameter from various references (Graph is taken from a reference Skukan *et al.* [Sku16]). The data of the recent experiment infer that charge amplification starts if Electric field ≥ 0.3 MV/cm.
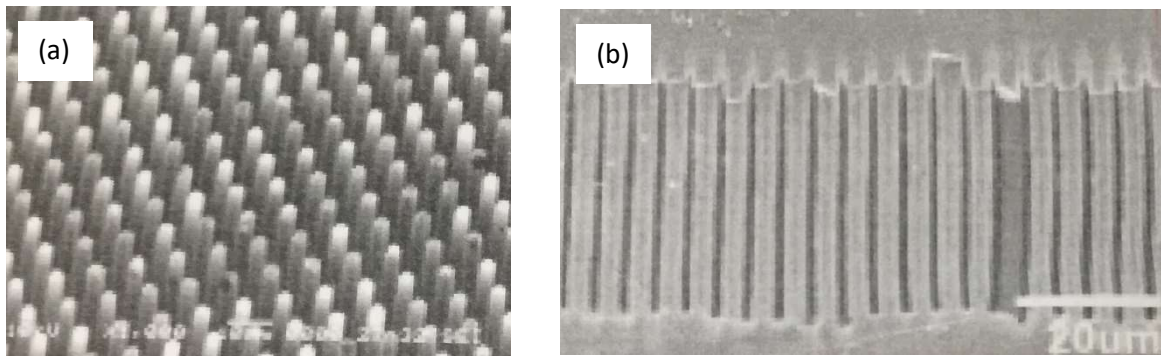

Figure 6-2. (a) The top surface diamond needles structure (b) The backend plate of diamond substrate and the surface of the needles. (Figures from Namiki Corp.)

The dimension of the needle structure is shown in the figure 6-3 (a). The backend of the needle structure is a bulk diamond. The first metal contacts will be fabricated on the backside of the backend bulk and the second contact is fabricated at the tips of needle structure. The design allows particle to deposits its energy at the planar contact of backend bulk diamond (figure 6-

3 (b)). The needle structure confines electric field and it is designed to enhance the electric field. If carriers are generated near the bulk contact, the carriers are attracted inside the needle that has higher electric field. Thus, the charges may be multiplied due to high electric field inside the needles.
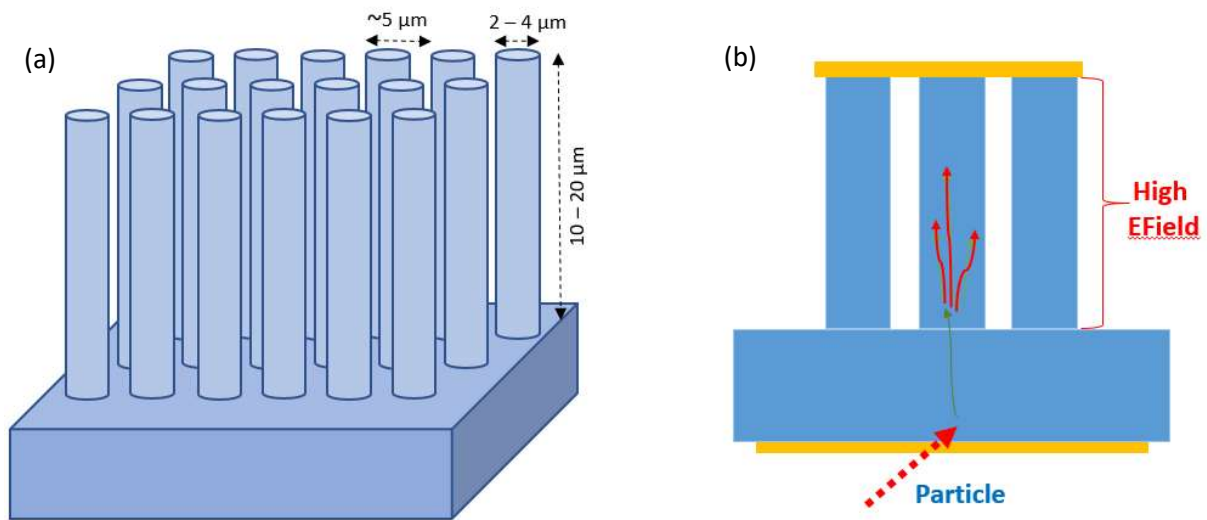

Figure 6-3. (a) The geometrical size of the diamond needles structure (b) The side view of the needle structure while high energy particle deposits energy near the contact. The red arrow represents the high energy particle. The green arrow represents carrier with low energy in low electric field region. The red arrow represents carrier becomes energetic and generates additional charges in high electric field region.

By using the parameter of charge carrier concentration, carrier mobility, saturation velocity and carrier life-time from characterization in previous chapter, the needle structure is simulated. In the simulation, a diameter of 4 μm and the space between the needle of 3 μm was implemented. By the simulation, the strength of electric field is compared for different bias voltage, height of the needle, and the thickness of the backend substrate.

Under -100 V bias, all of configurations indicate the electric field inside the narrow needle is significantly higher than that inside the bulk. Moreover, the electric field distribution in the needle structure is also quite uniform (figure 6-4). The uniform electric field inside the needle may allow uniform charge amplification. Therefore, the estimation of deposited energy can be carried out by measuring the signal.

Figure 6-4. The distribution of electric field of diamond needle structure. The contact on backend bulk is connected to the ground and the contact at top surface of the needle is biased with -100 V. (a) The needle structure with the height of 5 μm and the thickness of backend bulk is 15 μm. (b) The needle structure with the height of 15 μm and the thickness of backend bulk is 5 μm. (c) The needle structure with the height of 15 μm and the thickness of backend bulk is 35 μm.

The electric field distribution of the devices in figure 6-4 are shown in figure 6-5. In a bulk of intrinsic diamond with a low carrier concentration, the electric field will be uniform. If a 20 µm-thick bulk diamond with planar contact of both-sides is under -100 V, the estimated electric is 5 x 10^4 V/cm. The total thickness of the needle structure and its backend substrate is also 20 µm. By growing needle structure with height of 5 µm on 15 µm backend bulk, the electric field increase by > 60 % compared to the 20 µm-thick bulk diamond detector. However, the needle structure with a height of 15 µm on 5 µm backend bulk, the electric field improvement is only around 10 %. On the other hand, the device shown in figure 6-4 (c) has a total thickness of 50 µm. The bulk intrinsic diamond device with comparable thickness will generate 2 x 10^4 V/cm uniformly. In the simulation of needle structure with the same total thickness, the strength of electric field is improved by > 60 %. Therefore, the ratio of the height of needle and the thickness of backend bulk defines the enhancement of electric filed. The smaller ratio of needle height to the thickness of backend bulk results in a higher electric field improvement inside the needle structure.

Figure 6-5. The electric distribution of a vertical line in the middle of needle in figure 6-4. The red, blue and cyan line are electric field distribution of figure 6-4 a, b and c, respectively.

As expected, by increasing the bias voltage to -1000 V, the electric field is one order of magnitude higher than previous value (figure 6-6 and figure 6-7). By biasing the needle structure with this high bias voltage, all of the electric field inside the needle exceed 0.3 MV/cm. The number is sufficient to initiate charge amplification when carrier drift in the area.
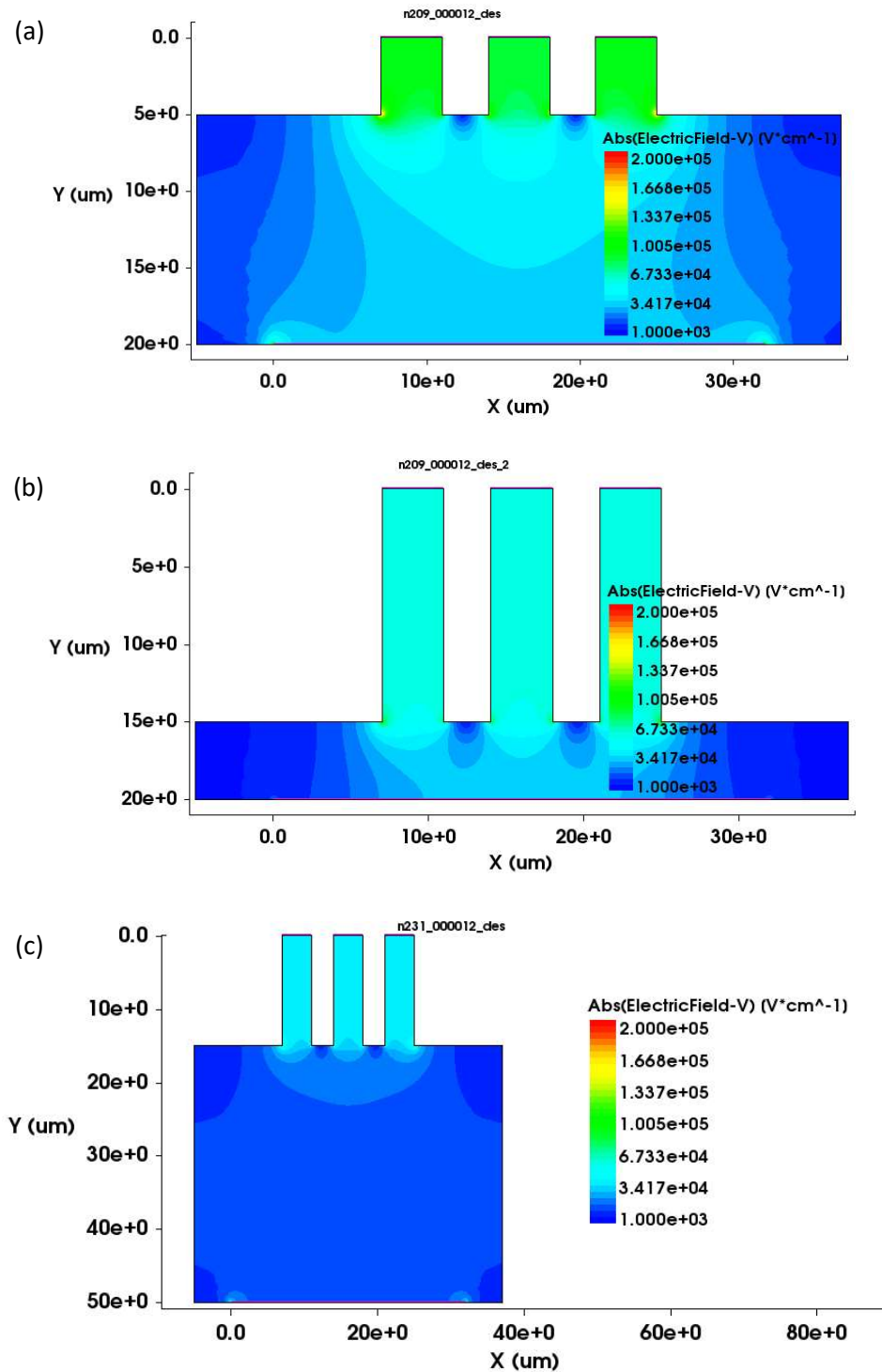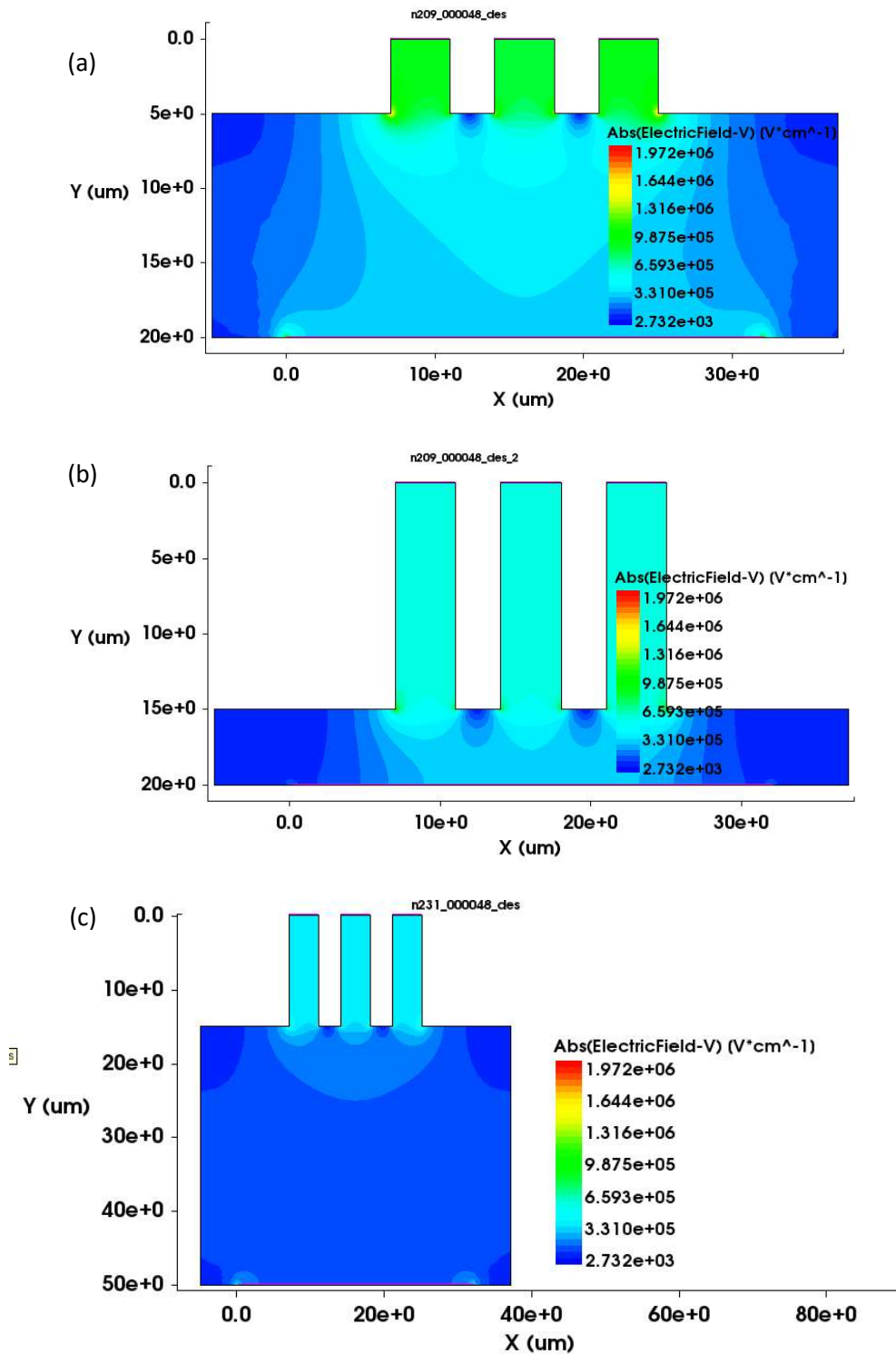
Figure 6-6. The distribution of electric field of diamond needle structure. The contact on backend bulk is connected to the ground and the contact at top surface of the needle is biased with -1000 V. (a) The needle structure with the height of 5 μm and the thickness of backend bulk is 15 μm. (b) The needle structure with the height of 15 μm and the thickness of backend bulk is 5 μm. (c) The needle structure with the height of 15 μm and the thickness of backend bulk is 35 μm.
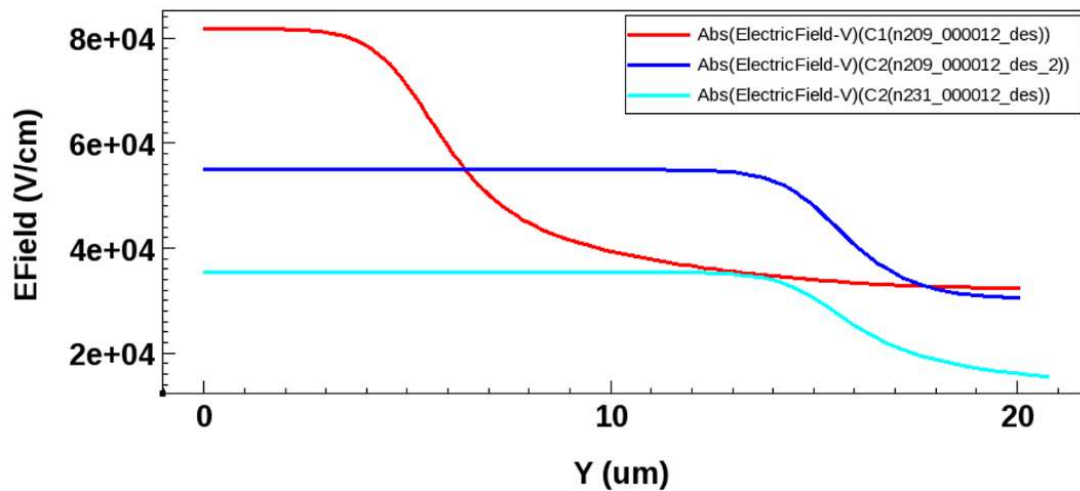
Figure 6-7. The electric distribution of a vertical line in the middle of needle in figure 6-6. The red, blue and cyan line are electric field distribution of figure 6-6 a, b and c, respectively.

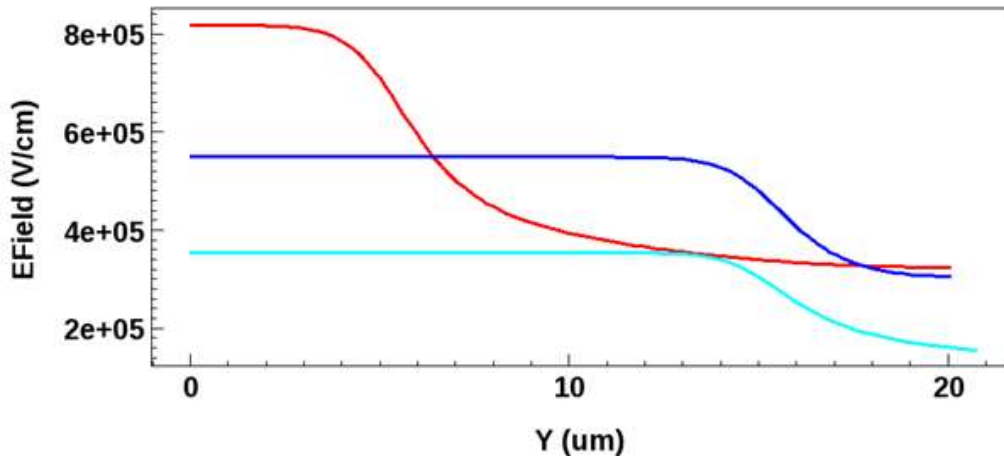In the figure 6-8, the simulation shows how the current of charges distributed inside the needle structure after high energy particle deposits energy near the backend contact. The low electric field in the backend bulk attracts the charges to the narrow needle with a high electric field. With the knowledge of the length of amplification drift path, the deposited energy can be calculated. The mechanism is quite similar with of that in Avalanche Photo Diode (APD). Due to the high field breakdown of diamond, the process may occur in whole intrinsic bulk instead of complicated silicon P^+IPN^+ structure.

The current signal of holes carriers indicates the signal can be well generated in the needle structure for bias voltage of -100 V, -1000V and -1600 V (figure 6-9). The charge integration of the signal model without impact ionization is 68 fC. The impact ionization improves the generated charge around 30% and 370% under bias voltage of -1000 V and -1600 V, respectively. Thus, if the geometry of diamond detector can be realized, the drawback of low signal amplitude of diamond detector can be overcome.
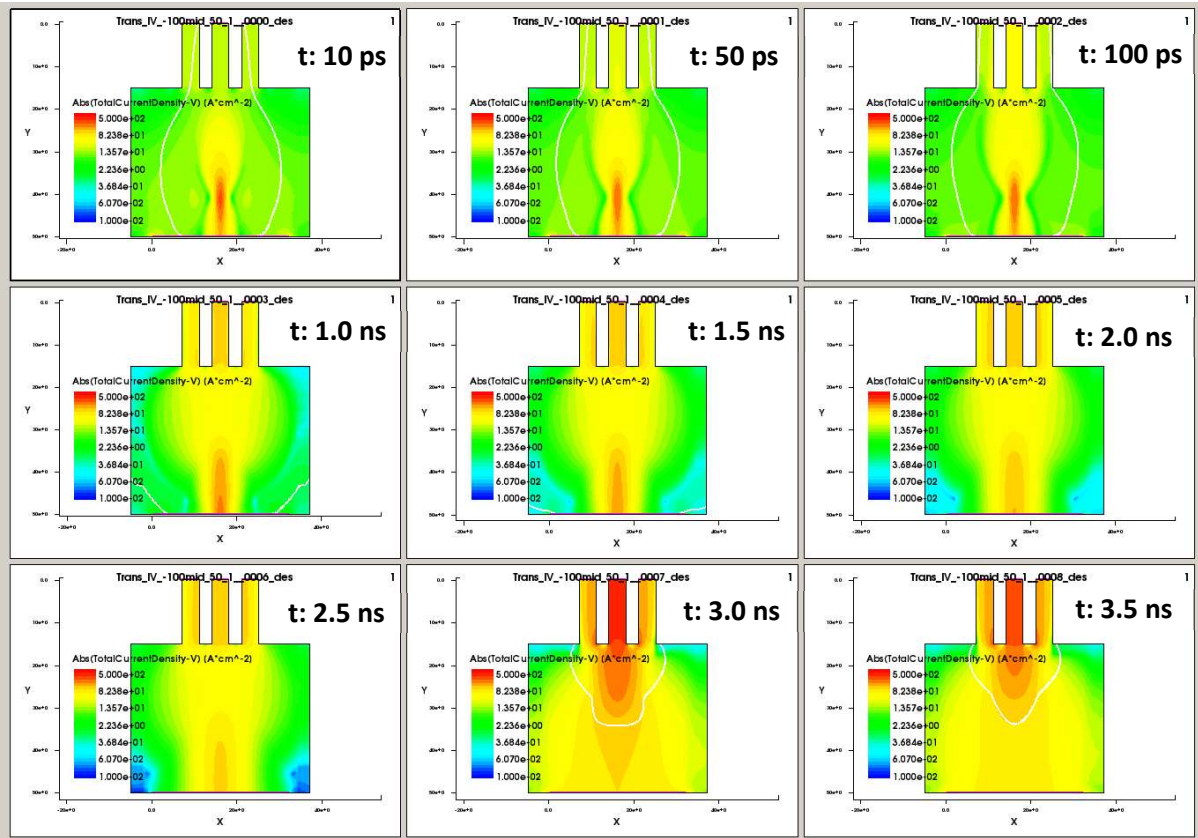
Figure 6-8. The distribution of charges current in needle structure with the height of 15 μm and the backend thickness of 35 μm as function of time under -100 V bias. The charges are generated near the backed-bulk contact and they are attracted to the needle. Due to high electric field in the needle, the amplification of carriers may occur.

(a)

(b)
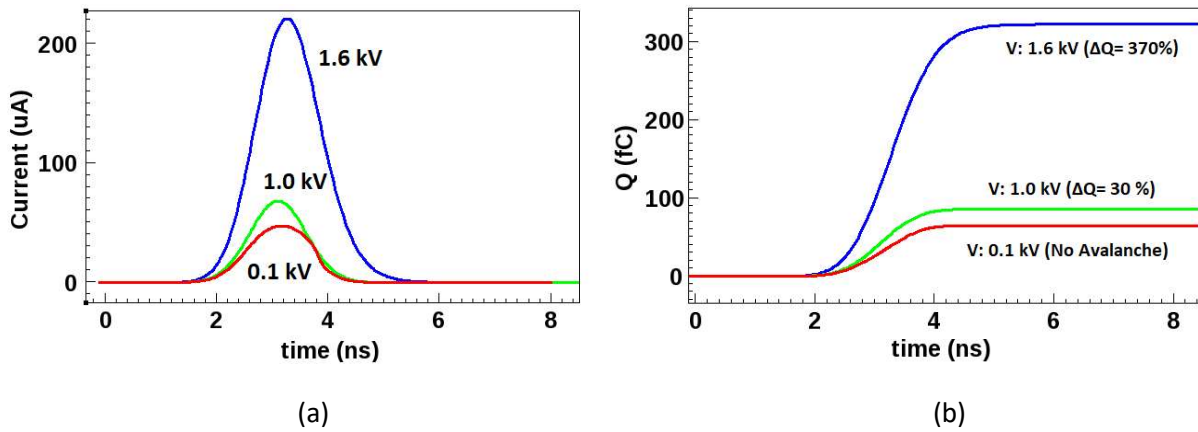
Figure 6-9. (a) The transient hole signal of 5.486 MeV α-particle impinges at the backend contact of 5 μm needle on 15 μm diamond bulk with and without impact ionization. (b) The integration of signal that shows ≈30% improvement of generated charges due to the impact ionization.

Chapter 7

Fast Transimpedance Amplifier

In order to build a set of diamond sensor read-out system for particle experiment, a multi-channels fast amplifier is a necessity for front-end electronics to detect high count rates of incoming particles. Unfortunately, the commercially available fast amplifiers are not suitable for large array multi-channel diamond detector due to a large power consumption. The large power consumption of the fast amplifiers is caused by the application of old bipolar transistor design in their circuit. In this work, a fast Application-Specific Integrated Circuit (ASIC) amplifier is designed based on the cutting-edge technology of the 65 nm CMOS transistor.
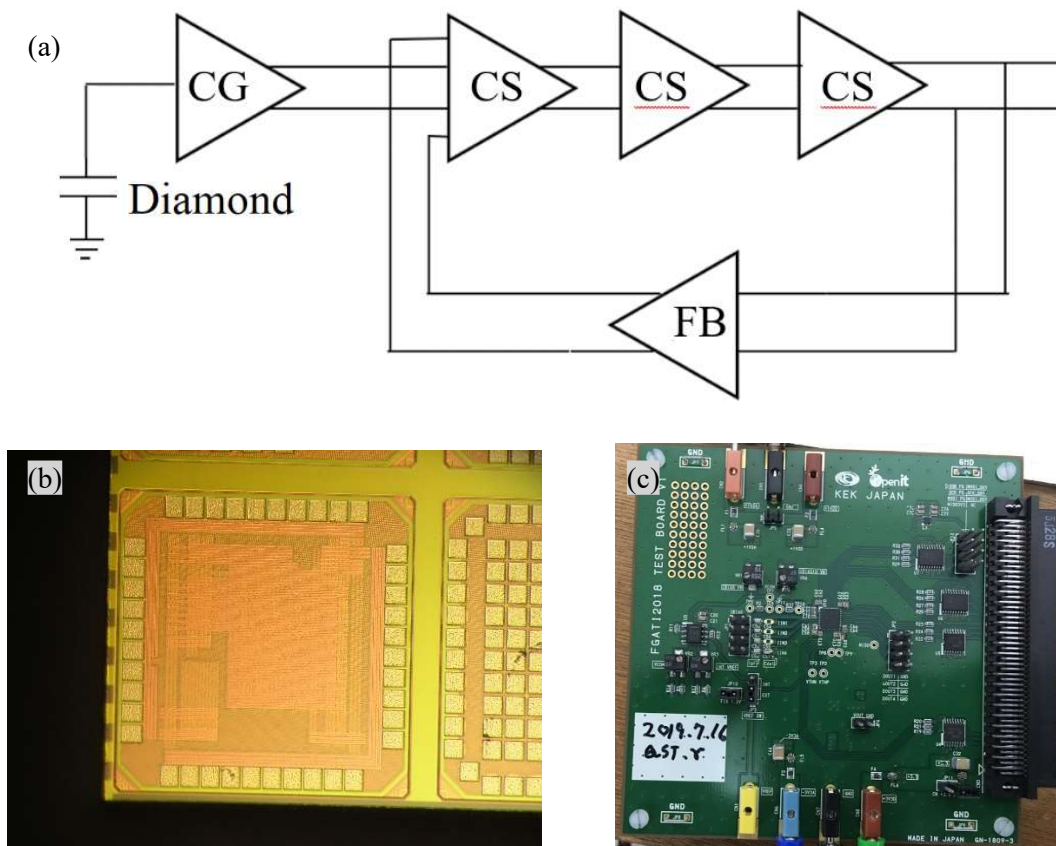

Figure 7-1. (a) The block diagram of FGATI amplifier. CG, CS, and FB are Common-Gate preamplifier, Common-Source Amplifier, and Feedback Circuit, respectively. (b) The photograph of FGATI chip. (c) The photograph of 4-channel FGATI test board.

In designing a wide bandwidth, high gain, low noise, low power consumption amplifier, a differential Transimpedance Amplifier (TIA) with Flipped Voltage Follower (FVF) current preamplifier was developed for front-end application in particle experiment. The differential configuration is selected in designing this TIA because it has a lower noise level than a single-end amplifier. On the other hand, the FVF Common-Gate (CG) preamplifier promises low power consumption and low thermal noise level. The block diagram of the FGATI amplifier and the photograph of the FGAT chip on a silicon die are shown in figure 7-1a and 7-1b, respectively. A test board shown in figure 7-1c is manufacture to evaluate the performance of the FGATI design.

7.1 Input Stage Common-Gate Preamplifier
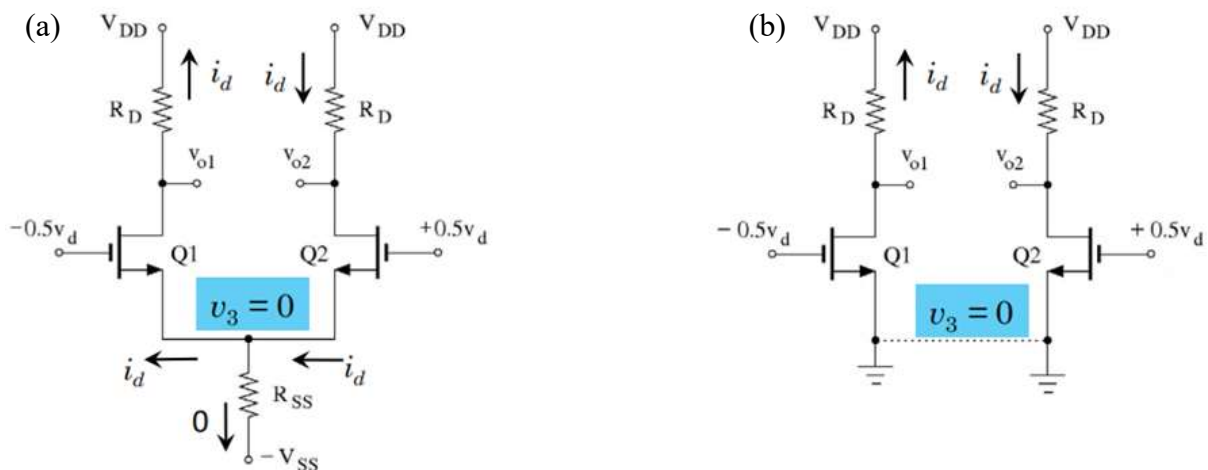
Figure 7-2. (a) A differential Common-Source Amplifier, the specification of both CMOS is considered identical. (b) The simplified circuit. For small signal-current, no current signal flows through the lower current source. The node is considered as a virtual ground. The differential gain is expressed in equation 7.1. v_d and i_d are voltage signal and small current flow, respectively [Ran12].

The main benefit of the Transimpedance Amplifier upon the widely used differential Common-Source (CS) amplifier is the potency of CG configuration to result in an amplifier with a wider bandwidth and lower power consumption. The wider bandwidth of CG input configuration than CS configuration comes from the fact that the CS amplifier is more prone to the Miller effect. The Miller effect increases the Gate-Drain capacitor (C_{GD}) proportionally to the transistor gain. This phenomenon decreases the bandwidth of the circuit. Fortunately, Miller effect is not a problem for CG configuration.

On the other hand. the potency of lower power consumption of CG configuration comes from the mechanism to yield the differential gain which is different with that of CS. For the differential CS amplifier (figure 7-2), the differential gain is proportional to the transconductance (g_m) of the CMOS that can be defined by equation:

$$\frac{v_{o1}}{-0.5v_d} = -g_m(r_0 \parallel R_D) \quad \text{and} \quad \frac{v_{o1}}{-0.5v_d} = -g_m(r_0 \parallel R_D)$$

$$G = -g_m(r_0 \parallel R_D), \tag{7.1}$$

with v_{01} is negative output voltage, v_{02} is positive output voltage, v_d is the input voltage, r_0 is a resistance of the NMOS due to channel length modulation, R_D is load-resistance, and R_{SS} is bias-resistance. The load resistance R_D can be in the form of PMOS active-load. On the other hand, the bias resistor R_{SS} is the resistance of a current source. R_{SS} is not involved in the calculation because the small current signal does not flow through R_{SS}. The transconductance is proportional to Direct Current (DC) current of CMOS as indicated in the equation below:

$$g_m = \frac{I_D}{(V_{GS} - V_{th})}, \tag{7.2}$$

with I_D is DC current of the CMOS DS-channel, V_{GS} is gate voltage of the CMOS and V_{th} is the threshold voltage. By Substitute equation 7.2 to equation 7.1, the direct relation of differential gain with the DC current as shown in equation:

$$G_{CS} = \frac{-I_D(r_0 \parallel R_D)}{(V_{GS} - V_{th})}. \tag{7.3}$$

Hence, to achieve high differential gain with Common-Source amplifier, the DC current should also be high. Eventually, a high bias voltage is required in operation of CS amplifier that consumes relatively large power.
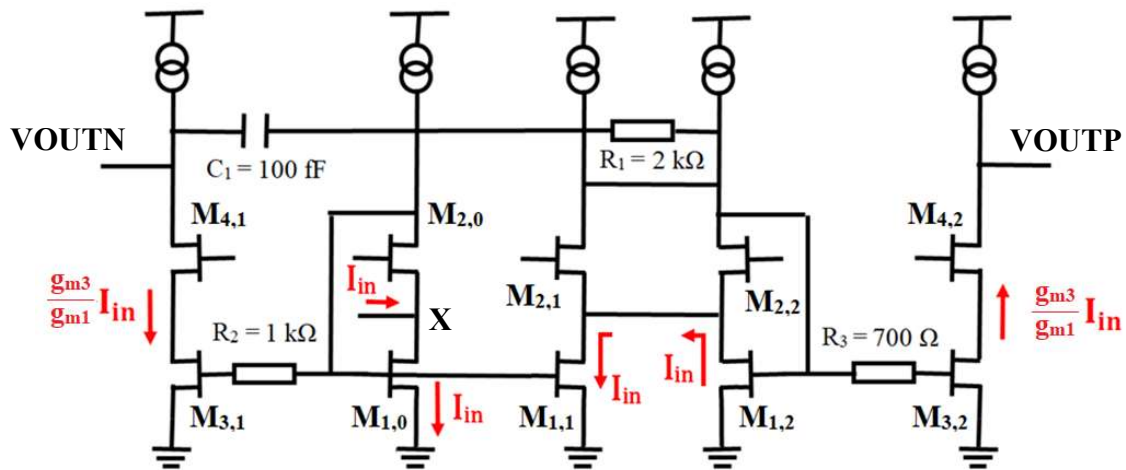
Figure 7-3. The Schematic of Transimpedance Amplifier with current mirror FVF topology. The design defines the transconductances of NMOS $M_{1,0}$, $M_{1,1}$, and $M_{1,2}$ are equal to g_{m1}. The transconductance of NMOS $M_{2,0}$, $M_{2,1}$, $M_{2,2}$, $M_{2,3}$, $M_{3,1}$, and $M_{3,2}$ are equal to g_{m3}. The transconductance of NMOS $M_{4,1}$ and $M_{4,2}$ are equal to g_{m4}. Load resistances of this amplifier are active-loads comprised of PMOS. The unconnected gates of the upper NMOSs are biased with a constant voltage.

Unlike Common-Source amplifier, the common gate amplifier in TIA attains high gain independent of the DC current of the CMOS. The configuration of the current amplifier as input stage in TIA is shown in figure 7-3. The gates of all upper NMOS ($M_{2,0}$, $M_{2,1}$, $M_{2,2}$, $M_{4,1}$, $M_{4,2}$) are kept constant during the operation. That makes the lower NMOS ($M_{1,0}$, $M_{1,1}$, $M_{1,2}$, $M_{3,1}$, $M_{3,2}$) control the flow of signal current. When a signal current is fed to the input Node X, the majority of current signal flows through the NMOS $M_{1,0}$. The flow of signal simultaneously increases the Drain voltage of NMOS $M_{2,0}$ that loops to the gate of NMOS $M_{1,0}$. The gate voltage is also transmitted to NMOS $M_{3,1}$ and $M_{1,1}$. The ratio of the transconductance of NMOS $M_{3,1}$ and $M_{1,1}$ defines the current gain of the negative output (VOUTN). On the other hand, the transconductance of $M_{1,1}$ is similar to the transconductance of NMOS $M_{1,0}$. Therefore, the NMOS $M_{1,0}$ behaves as a current mirror for NMOS $M_{1,1}$ that makes NMOS $M_{1,1}$ generate a current similar to the input current signal through its Drain-Source (DS) channel.

Due to the constant gate voltage of NMOS $M_{2,1}$ and $M_{2,2}$, the current signal is pulled from the drain NMOS $M_{1,2}$ to form a looping signal current. The loop is essential to create differential conversion. The current drives the drain voltage of NMOS $M_{2,2}$ that loops to the gate of NMOS $M_{1,2}$. The gate voltage of NMOS $M_{1,2}$ is connected to the gate of NMOS $M_{3,2}$. Thus, the voltage drives the DS current of NMOS $M_{3,2}$. The transconductance of NMOS $M_{3,2}$ is similar to that of

NMOS $M_{3,1}$. Therefore the magnitude of the current signal is similar, but they have opposite polarity. The differential gain of this current amplifier depends on the output Resistor. If the output resistor is $R_{out}/2$ for each output, the voltage of the output is derived by equation:

$$V_{OUTN} = M \cdot I_{in}R_{out}/2 \quad \text{and} \quad V_{OUTP} = -M \cdot I_{in}R_{out}/2$$

$$V_{OUT} = M \cdot I_{in}R_{out}$$

$$G_{CG,\Omega} = M \cdot R_{out} , \tag{7.4}$$

with M= g_{m3}/g_{m1} is Miller ratio. In a single die, the transconductance depends on the ratio between the total channel width and length of the CMOS. The gain calculation in equation 7.4 shows that it is independent of NMOS DC current. Therefore, the bias voltage can be set low, and the amplifier can work with low power without affecting its amplifying performance. The low power consumption is also closely related to low power dissipation. Power dissipation increases temperature of amplifier input stage that generates noise. Input current noise is proportional to temperature that can be approximated by equation [Wan05]:

$$\overline{I_{n,total}^2} = ckT , \tag{7.5}$$

with c is a constant that depends on the topology of the amplifier, k is Boltzmann constant, and T is the absolute temperature. Hence, FVF TIA design can avoid high input noise level due to less power dissipation than a Common-Source amplifier.

Particle experiments often require a high-speed amplifier with a wide bandwidth of some GHz. In TIA, the bandwidth is inversely proportional to the capacitance at the input node and input impedance. Therefore, low input capacitance and input impedance are desirable. The input capacitance at input node X is comprised of:

$$C_{in} = C_D + C_{gd,1} + C_{gs,2} + C_{sb,2} , \tag{7.6}$$

with C_D = detector capacitance, $C_{gd,1}$ = gate-drain capacitance of NMOS $M_{1,0}$, $C_{gs,2}$ = gate-source capacitance of NMOS $M_{2,0}$, $C_{sb,2}$ = source-bulk capacitance of NMOS $M_{2,0}$. However, the total capacitance from both NMOS is in order of few femtofarads. On the other hand, the capacitance of a diamond detector is in order of few picofarads. Therefore, the capacitance of the detector is the main factor that defines the input capacitance of the TIA circuit. Eventually, the bandwidth of the circuit is simply written by equation:

$$\omega_{3-dB} = \frac{1}{C_D Z_{in}} \quad . \qquad\qquad (7.7)$$

The detector capacitance is a parameter inherently given by the type of detector material and its design. Whereas, the input impedance can be optimized by choosing the topology of the amplifier circuit.

In order to obtain the desirable low input impedance, the topology of this TIA amplifier forms current-mirrors with FVF configuration. The input signal is fed to the drain of the lower NMOS ($M_{1,0}$), and a loop connects the drain of upper NMOS ($M_{2,0}$) to the gate of $M_{1,0}$ (Figure 7-3). With the configuration, small signal current at the input node is divided through both NMOS. However, the voltage loop from the drain of $M_{2,0}$ to the $M_{1,0}$ gate reduces the resistance of $M_{1,0}$ D-S channel. Hence, the majority of current flows through $M_{1,0}$ NMOS. This configuration decreases the input impedance of the amplifier, the input impedance is expressed in equation:

$$Z_{in,X} \approx \frac{1}{g_{m2} \cdot (1 + g_{m1} R_{B,P})} \quad , \qquad\qquad (7.8)$$

with $R_{B,P}$ is the load resistance due to PMOS current source. This low impedance is a more suitable option to achieve a wide bandwidth compared to another option of FVF input node.

If the current input signal is fed to the drain of NMOS $M_{2,0}$ at node Y as shown in figure 7-4a, the input impedance is higher because the signal current flows through NMOS $M_{2,0}$ and $M_{1,0}$. The D-S channel resistance of $M_{1,0}$ is reduced by the loop as the previous configuration, but the channel resistance of NMOS $M_{2,0}$ is still high. Therefore, the signal current flows through a significantly higher resistance. The approximation of input impedance with this configuration is:

$$Z_{in,Y} \approx \frac{R_{B,P}}{g_{m1} R_{B,P} + 1} \quad . \qquad\qquad (7.9)$$

At low frequency, this alternative configuration can have input impedance around one order of magnitude higher than the current configuration in TSMC 65 nm CMOS technology. Thus, due to higher input impedance, this alternative option is not an ideal option for designing an amplifier with wide bandwidth output.
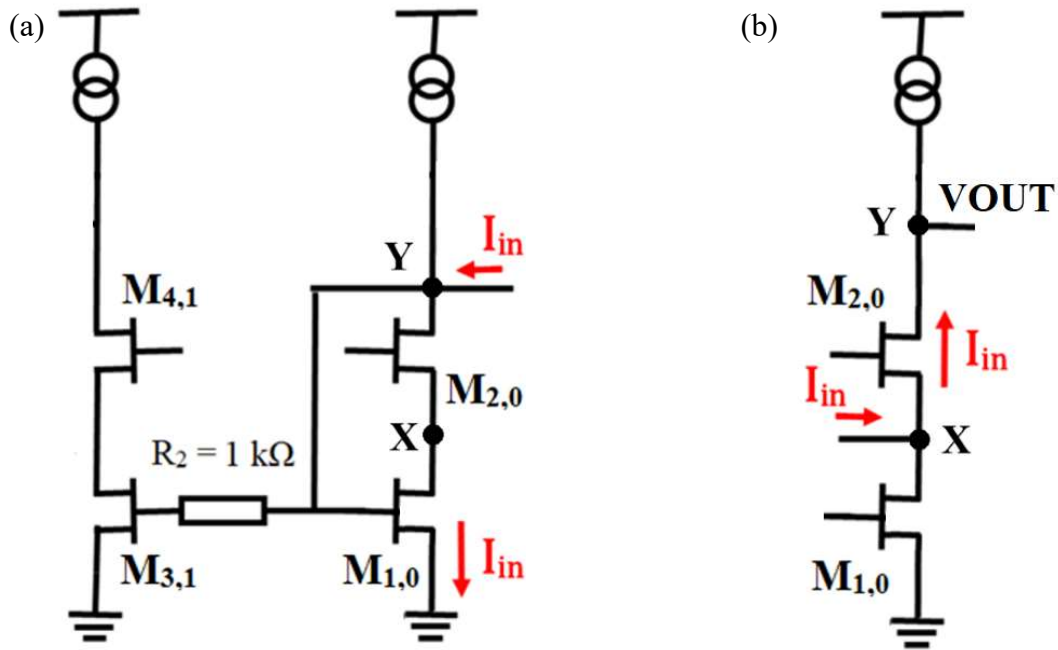
Figure 7-4. The Schematic of the input stage of TIA(a) with alternative input at Y node, and (b) Regular (REG) without Loop configuration.

The common configuration of the TIA input is Regular (REG) configuration without loop as shown in figure 7-4b. The Gate-Source (GS) voltage of the NMOS $M_{1,0}$ is constant while signal enter the circuit. Therefore, no signal current flows to NMOS $M_{1,0}$. All input current flows to NMOS $M_{2,0}$. The input impedance for this configuration is

$$Z_{in,REG} \approx \frac{1}{g_{m2}} \quad . \tag{7.10}$$

Compared to the input impedance FVF TIA ($Z_{in,X}$), the WOL input impedance is significantly larger. The order approximately similar with the input impedance of the $Z_{in,Y}$. Thus, the decision to use FVF TIA configuration is better to other two options for designing a TIA with a wide bandwidth.

The additional components on the schematic (figure 7-3) are the serial Resistor and capacitor that connect the VOUTN and the drain of NMOS $M_{2,2}$. The nonsymmetrical configuration from the input line to VOUTN and VOUTP is unavoidable due to the differential loop between the input line and VOUTP. The longer signal transmission process makes VOUTP signal prone to a longer delay. The positive feedback is applied from VOUTN to the differential driver loop to mitigate the delay and improve the bandwidth of VOUTP output. The other additional

components are the resistor R_2 and R_3 at the gate of NMOS $M_{3,1}$ and $M_{3,2}$ have a function to stabilize the circuit due to an unstable pole near the 3-dB frequency.

7.2 Differential Common-Source Stage

The differential amplifier is a better configuration to manage the noise problem compared to a single-ended amplifier. A differential amplifier theoretically has a low noise level due to the common-mode rejection (CMMR) property. Unlike the single output amplifier that transmits all noise to the output, the positive and negative output of the differential amplifier is subtracted. The subtraction removes common-mode (CM) noise from the output. Thus, it is able to cancel-out coupling noise and ripple that is unavoidably transmitted from inputs and power lines of the amplifier.

In order to improve the gain of TIA, the current preamplifier is followed by three stages of Common-Source amplifier. The schematic of a single stage of the common-source amplifier is shown in figure 7-5. The current sources above the output node are comprised of PMOS. NMOS M_1 and M_2 gate voltage have a role as a current source by keeping the gate of both NMOS constant. The positive (negative) output voltage of the input stage preamplifier is fed to NMOS M_3 (M_4). The input voltages that drive NMOS M_3 and M_4 has opposite polarity. Due to the opposite polarity of those input voltages, the current flow in the DS channel of NMOS M_3 and M_4 also have opposite polarity and form a loop of current. The current-sources above and below the driven NMOS keep their channels' current constant. Therefore, the current signal flows through the load resistance R. If the other resistance parallel to output node is assumed significantly larger than R, the gain of this CS Amplifier stage is approximately:

$$G_{CS1} = -g_m R. \tag{7.11}$$

with g_m is the transconductance of NMOS M_3 and M_4. VREF can be tuned to adjust the gain and bandwidth of the CS amplifier. In the setup, two value of R is available in the test board. By activating the internal switch, the second resistor with significantly lower resistance can be activated. The activation of the switch turns off the gain of the CS stage.
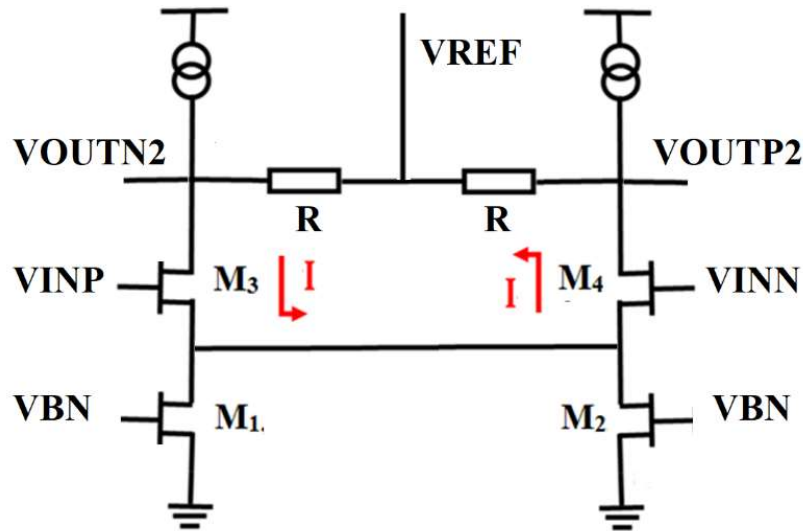
Figure 7-5. A stage of Common-Source amplifier. M_1 is identical to M_2, and M_3 is also identical to M_4.

7.3 Simulation Result

Simulations were conducted for this TIA amplifier with Spectre simulator from Cadence by using TSMC 65 nm technology. In the simulation, the input of the FVF preamplifier is a current source in parallel to 1 pF additional dummy capacitor. The 1 pF additional capacitor comes from the ≈0.5 pF diamond capacitor and other 0.5pF additional stray capacitor from input cable connector and the pad of PCB board [Wan05]. As suggested by theory, the input capacitance defines the bandwidth of the amplifier. By variating the input capacitor with one order of magnitude step, the simulation shows positive output voltage of CG preamplifier has significantly different bandwidth (figure 7-6)). The bandwidths of CG preamplifier with C_{in} 0.1 pF, 1 pF, 10 pF, 100 pF are around 3 GHz, 3 GHz, 2 GHz, 200 MHz, respectively.

In the simulation, the effect of input node position is shown in figure 7-7. The simulation confirms the advantage of feeding the input to X-node to improve the bandwidth. Within the operational range, the input impedance at X-node is more than 10 times lower than the input impedance at Y-node. However, the impedance becomes in the same order when frequency > 2 GHz. The input impedance of REG configuration is even larger than that of FVF amplifier due to the absent of the loop as shown by blue line.

With input at X node and input capacitor 1 pF, the bandwidth of TIA and all stages of FGATI amplifier are shown in figure 7-8 and figure 7-9, respectively. The bandwidth of positive output and negative output is almost identical. The bandwidth of TIA is ≈ 3.6 GHz with a gain of 46

dBΩ for each output. On the other hand, the bandwidth of FGATI is ≈ 2.7 GHz with a gain of 75 dBΩ for each output. By subtraction both FGATI outputs, the total gain is 80.3 dBΩ (10.4 kΩ). This simulation confirms the 3 stages of CS amplifier improve the gain of low power FVF preamplifier. The -180^0 phase-shift in TIA and overall FGATI amplifier occurs at relatively high gain. However, this amplifier does not have feedback signal, therefore the large phase shift does not affect the stability.
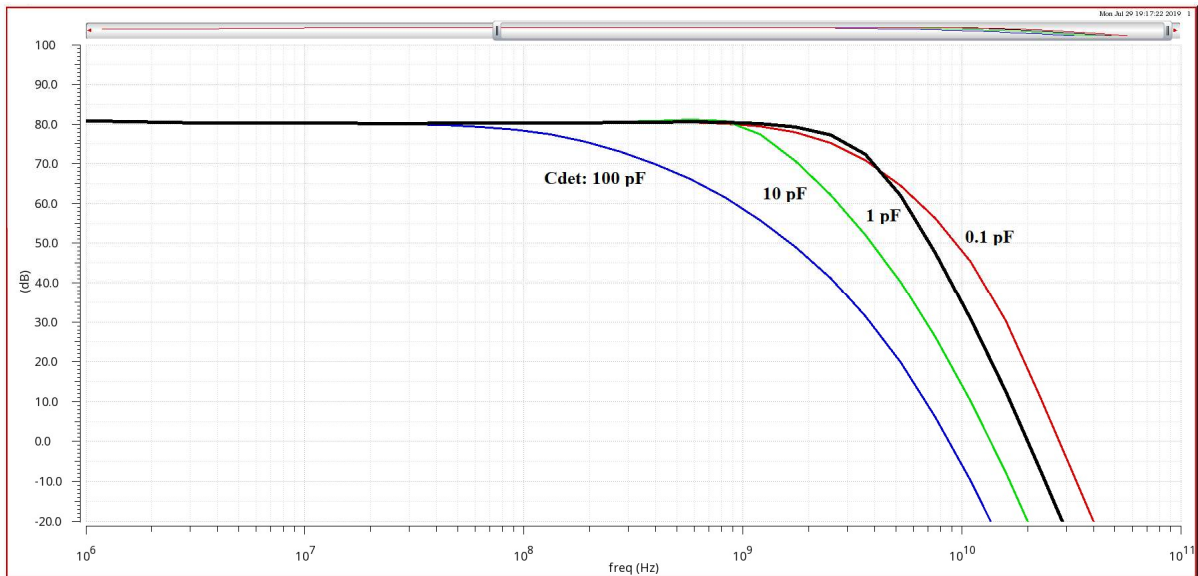
Figure 7-6. The frequency response of CG preamplifier for the positive output (VOUTP) as a function of detector capacitance.

The effect of additional RC as positive feedback from VOUTN to differential loop is shown in figure 7-10. The positive feedback gives improvement to the frequency response of VOUTP output of CG preamplifier. The gain of VOUTP becomes more identical to that of VOUTN at high frequency. On the other hand, this additional RC results in no significant effect to the improvement of phase delay of the preamplifier output.
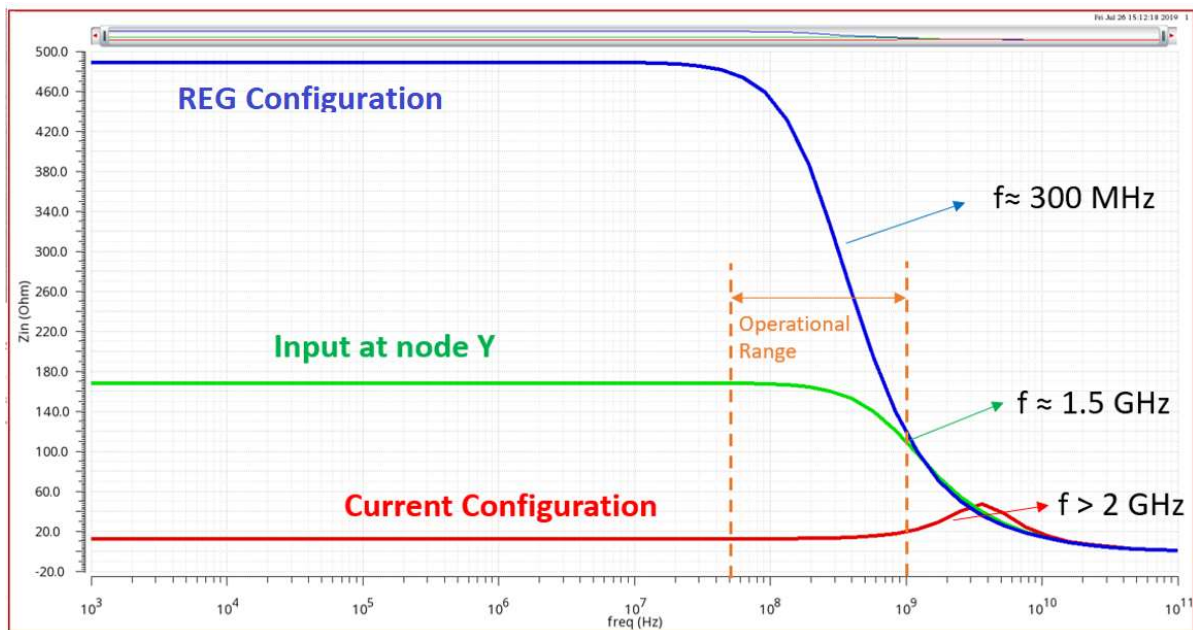
Figure 7-7. The input impedance in linear scale of FVF TIA amplifier at node X is shown by a red line. The input impedance if the input is at node Y is shown by green line. The input impedance of REG TIA is shown by blue line.

By biasing TIA with 1.2 V power supply, the simulation shows that the current flows through the power-line 5.9 mA. Therefore, the power consumption of this TIA amplifier is 7.1 mW. The power consumption is significantly smaller than that of amplifier widely used for diamond detectors. For example, Minicircuit Gali52+ and Cividec TCT amplifier have an operational power consumption of 780 mW [Mini] and 1.2 W [Civi], respectively.
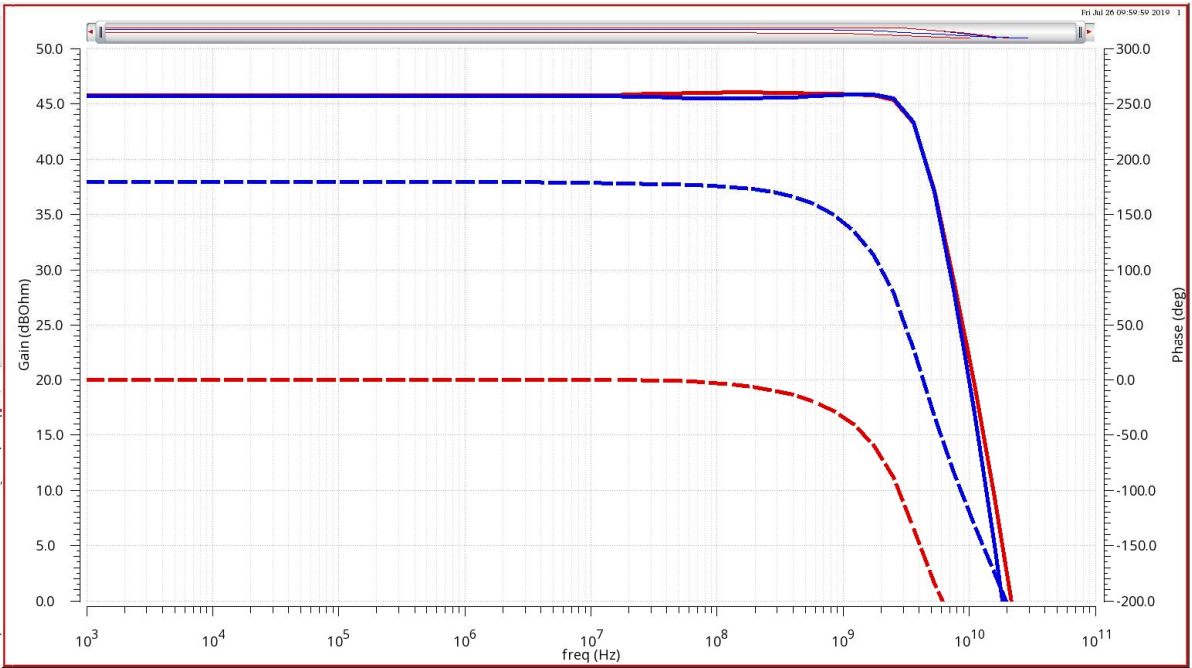
Figure 7-8. Solid-blue (red) line represents the frequency response of the AOUTP (AOUTN) for TIA stage. The dashed-blue (red) line is the phase of the AOUTP (AOUTN) for TIA stage.

Figure 7-9. The gain and bandwidth of every stages in TIA. The blue, orange, green and red-line are the output of Common-Gate Preamplifier stage, first Common-Source stage, second Common-Source stage and final Common-Source stage, respectively. The final gain and bandwidth are 80.3 dBΩ and 2.7 GHz, respectively.

71
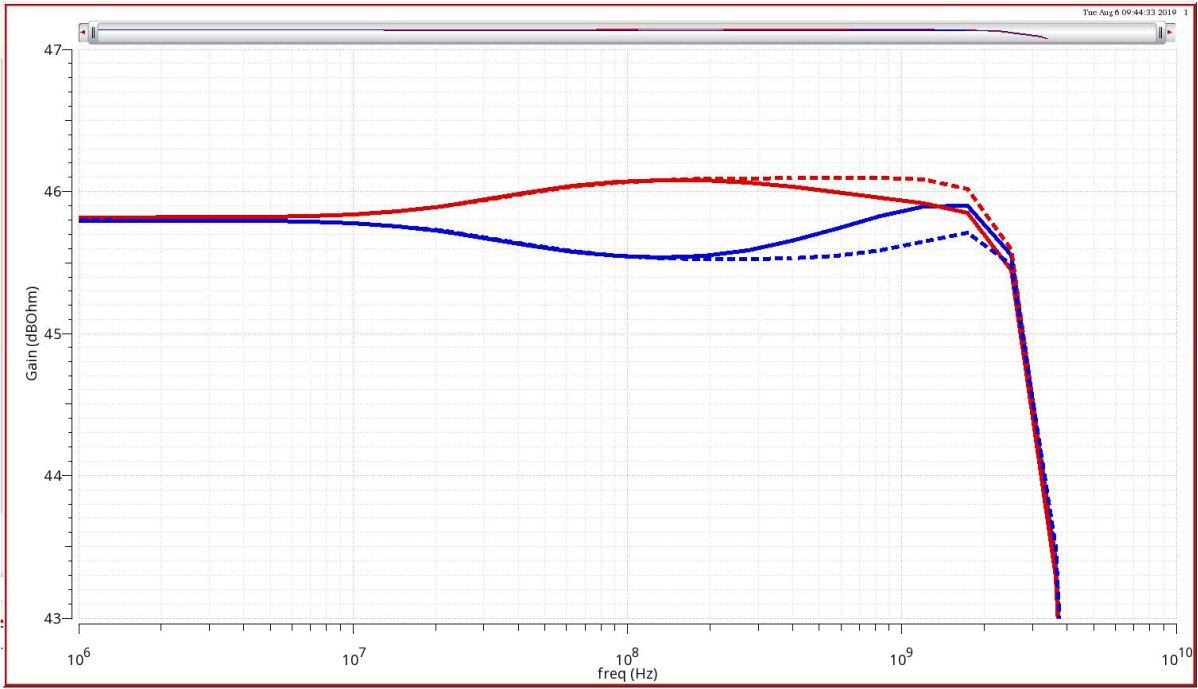
Figure 7-10. Solid-line (with-box) is the frequency response of TIA stage with (without) additional RC positive feedback. Blue-line and red-line are positive analog output (AOUTP) and negative analog output (AOUTN), respectively.

7.4 Measurement Result

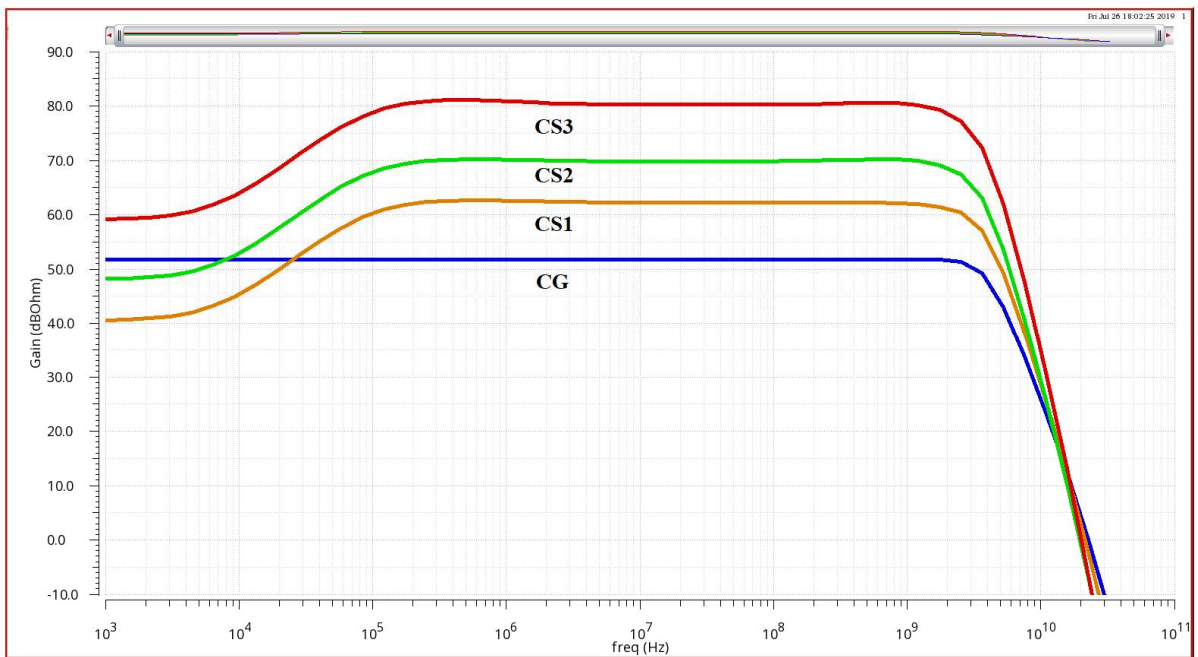In order to study the performance of the design of TIA circuit, a 4-channels TIA test board is evaluated. With the test board, current measured from 1.2 V power line is 24 mA. By this measurement, the power consumption of this TIA can be calculated as 28.8 mW for 4-channel or 7.2 mW/channel. This measurement confirms the low power consumption value acquired from the simulation.

Figure 7-11. (a) The connection of the pulse generator to TIA amplifier. (b) Connection of Diamond detector to TIA.

Test signal for evaluating of conversion gain of circuit and noise level is generated by a pulse generator Hewlett-Packard 8131A 500 MHz. An oscilloscope Teknotrik DPO 7254 2.5 GHz 40 GS/s is utilized to evaluate the output signal. The signal is probed by a high impedance Tektronik TAP 1500 1.5 GHz prober. The power supply for the TIA test board is a Texio PW-18 power supply.
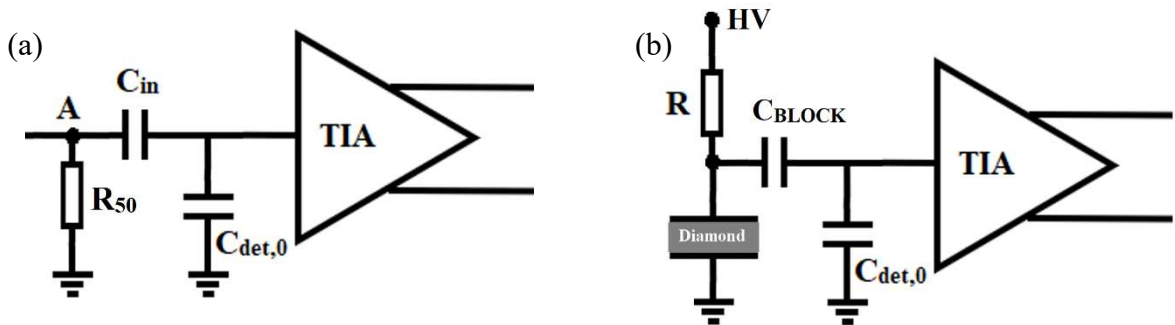
A voltage to current signal converter is incorporated before the input node of TIA amplifier. The input of TIA amplifier is a current signal, but the pulse generator transmits a voltage signal. Therefore, a 50 Ω resistor is connected in parallel at node A (figure 7-11a) for impedance matching. The node is connected to the input node of TIA amplifier by 1 pF C_{in} capacitor. Finally, the TIA input node is connected in parallel with $C_{det,0}$ additional capacitor. The total capacitor of the input disregard of other parasitic capacitors is:

$$C_{det} = C_{in} + C_{det,0} \qquad (7.12)$$

Evaluation of the dynamic range of TIA amplifier indicates that the maximum charge if C_{det} is 1 pF that still results in linear amplification is around ±40 fC (figure 7-12). With higher input capacitance, the saturation point of maximum input charge is also higher with lower bandwidth as the trade-off.

Conversion gain (G_C) of TIA is obtained from the linear slope of the output voltage amplitude versus input charge (figure 7-13). The G_C depends on the input capacitor, the highest GC of 8.43 mV/fC is obtained with C_{det} = 1 pF. On the other hand, the noise level in the circuit is reflected by Equivalent Noise Charge (ENC). For calculating ENC, standard deviation (σ_n) of output signal noise is measured. The relation of ENC with conversion gain and standard deviation of noise level is:

$$ENC\ (e) = \frac{G_C \cdot 1.6 \times 10^{19}}{\sigma_n} \qquad . \qquad (7.13)$$

The σ_n and ENC as a function of input capacitance are listed in table 7.1. The plot of ENC as a function of input capacitance is shown in figure 7-14. As predicted, the ENC increases proportionally to the input capacitance. The graph also confirms that the ENC is independent of input charge.

Table 7.1 The noise level standard deviation (σ_n), conversion gain (GC) and equivalent Noise Charge (ENC) as function of input capacitance (C_{det}).

Cdet (fC)	σ_n (mV)	G_c (mV/fC)	ENC (electrons)
1	6.7	8.4	4967
6	8.3	8.9	5857
11	9.7	7.8	7820
23	11.9	6.3	11757
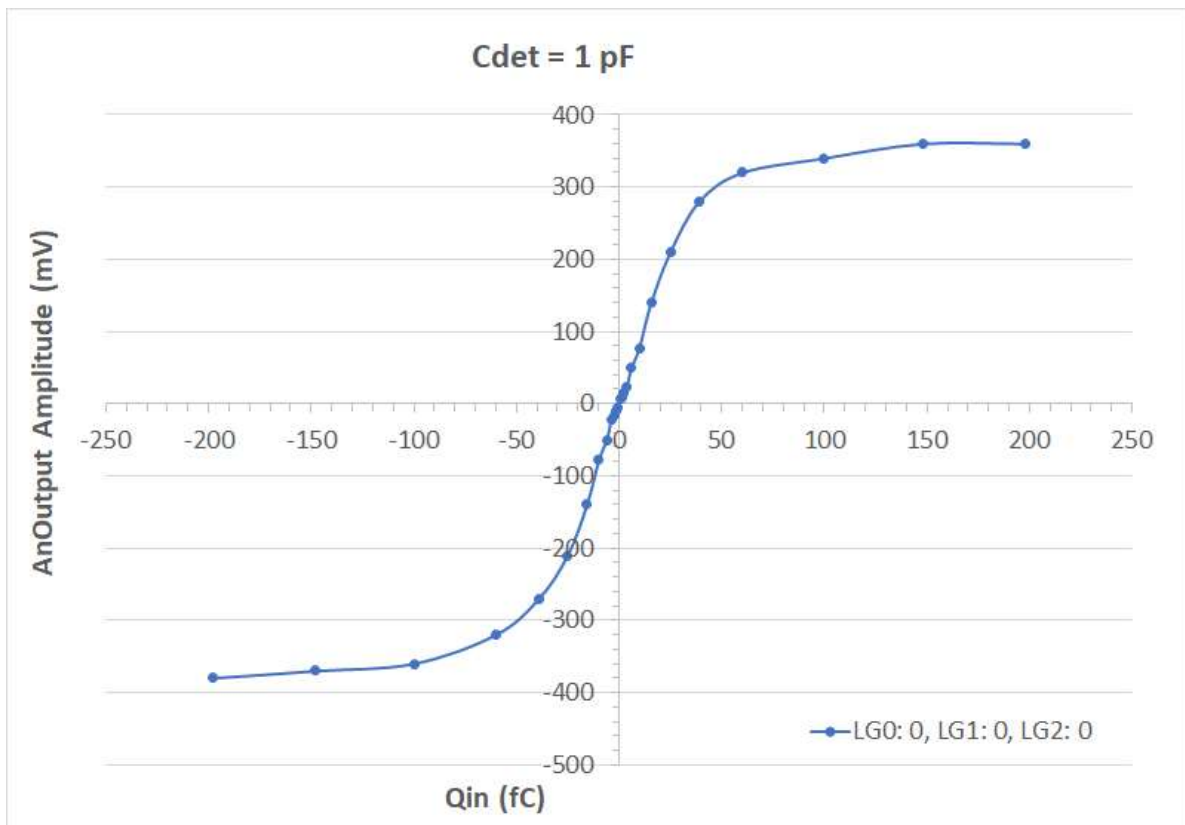
Figure 7-12. The dynamic range of TIA amplifier with C_{det} = 1 pF

The signal from the pulse generator has a leading-edge risetime of 0.3 ns. However, due to the effect of input capacitance, the leading-edge rise-time is slower. Risetime of signal leading edge is inversely proportional to the bandwidth. Therefore, by increasing the input capacitance, the frequency response gets slower, and the risetime is longer, as shown in figure 7-15.

A diamond detector is utilized to evaluate the gain of the FGATI amplifier. The amplifier is connected to a diamond detector to evaluate α-particle signal from ^{241}Am. The magnitude of current signal by using the setup is already measured thoroughly in chapter 4. Hence, the current can be use as the reference for the gain measurement. The $C_{BLOCK} = 2.2$ nF and R = 8 MΩ are utilized as a Bias-Tee to prevent high voltage (HV) bias connects to TIA input as shown in figure 7-11b. The C_{BLOCK} value is large compared to the diamond capacitor. Therefore, its effect to total input capacitance is omitted. On the other hand, the large resistor in the Bias-Tee acts as voltage divider of HV. However, most HV transmitted to diamond because diamond resistance is in TΩ order.
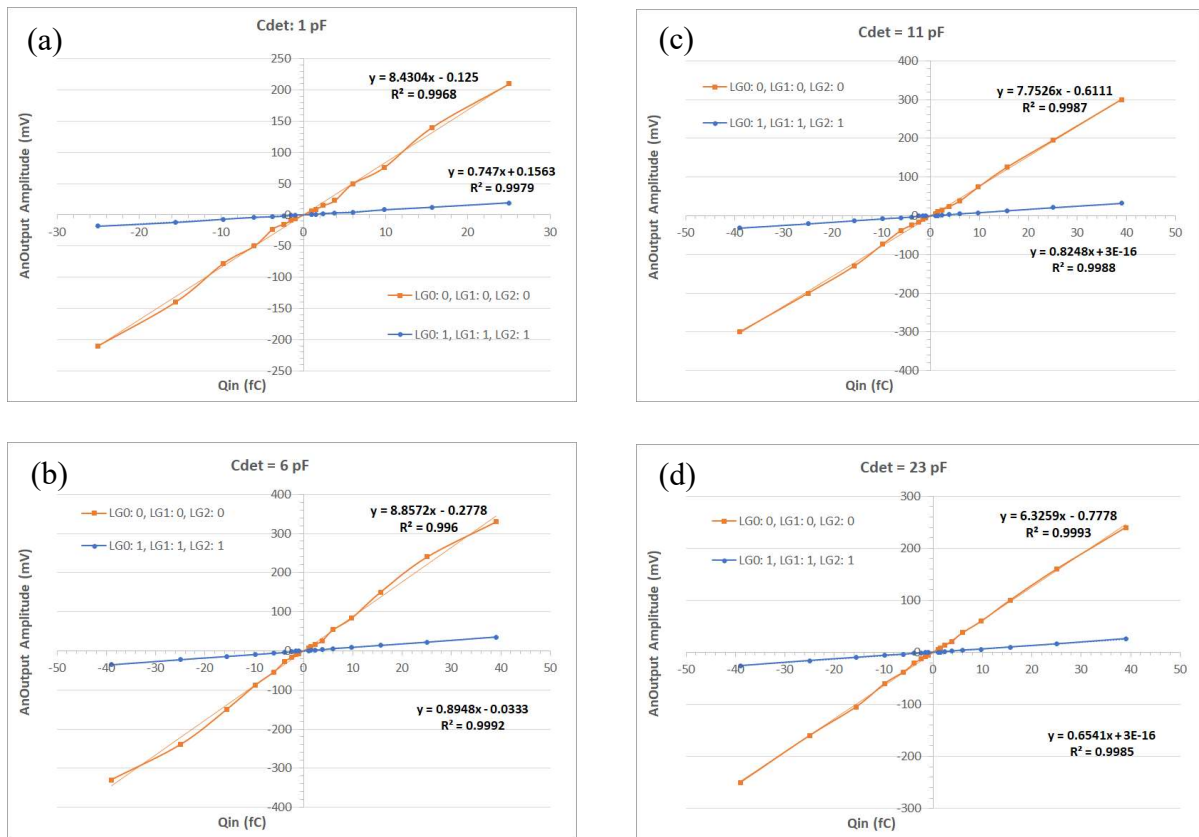
Figure 7-13. The conversion gain of TIA amplifier with (a) C_{det}: 1 pF (b) C_{det}: 6 pF (c) C_{det}: 11 pF (d) C_{det}: 23 pF. The orange (blue) line represents the conversion gain with all three CS stage activated (deactivated). The gradient of the lines is the conversion-gain of the circuit with a unit of mV/fC.
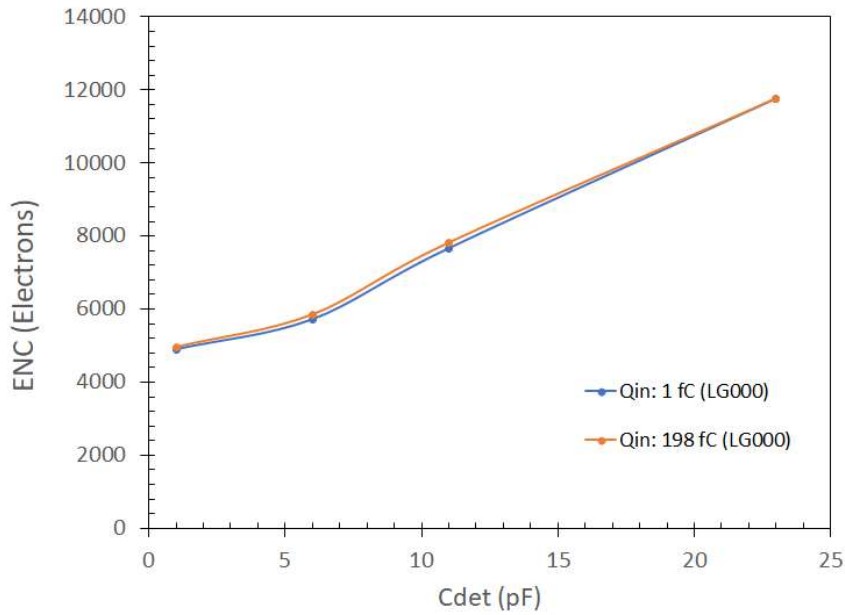
Figure 7-14. The ENC as a function of the input capacitance of TIA test bench.
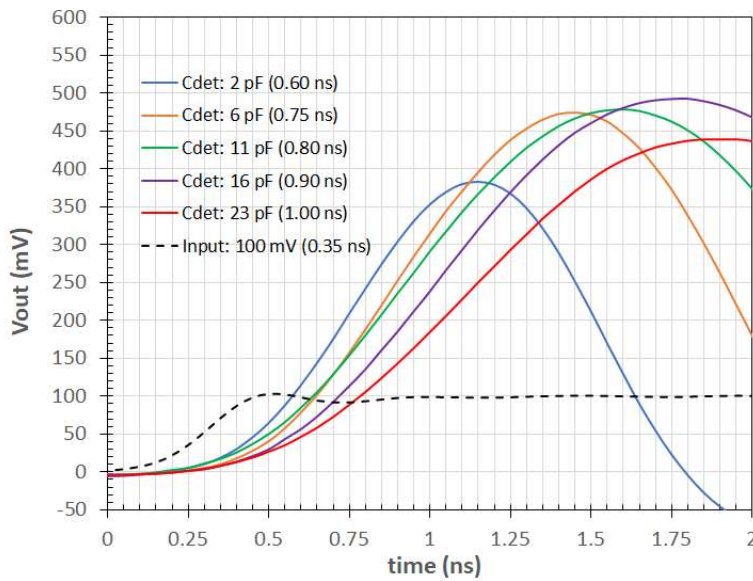
Figure 7-15. The leading-edge rise-time (10% - 90%) of TIA output signal.

Measurement of FGATI amplifier bandwidth is important to evaluate its performance. The setup for the measurement is shown in figure 7-16. The first part is the Signal Generator (SG) that generate sinusoidal voltage signals within frequency range of 100-2500 MHz. A 50 Ω impedance is connected in parallel to match the impedance of the SG. On the other hand, an additional capacitor of 0.1 µF is added for converting the voltage signal from the SG to a current signal. The 2 kΩ resistor is the estimation of the stray impedance in the transmission line before

FGATI input node. The frequency response of FGATI amplifier is evaluated by the Spectrum Analyzer. The analysis result of the frequency response is represented by the red data points in figure 7-17. The data is compared to realistic simulation that include effect of the additional capacitance, resistance and possible stray inductance of 2 nH at the input node of FGATI amplifier. It shows that the simulation result that has bandwidth around 1 GHz quite match with the data points.

Figure 7-16. The setup to measure the bandwidth of FGATI amplifier.

Figure 7-17. The comparison between the frequency response of FGATI amplifier by Simulation and measurement.

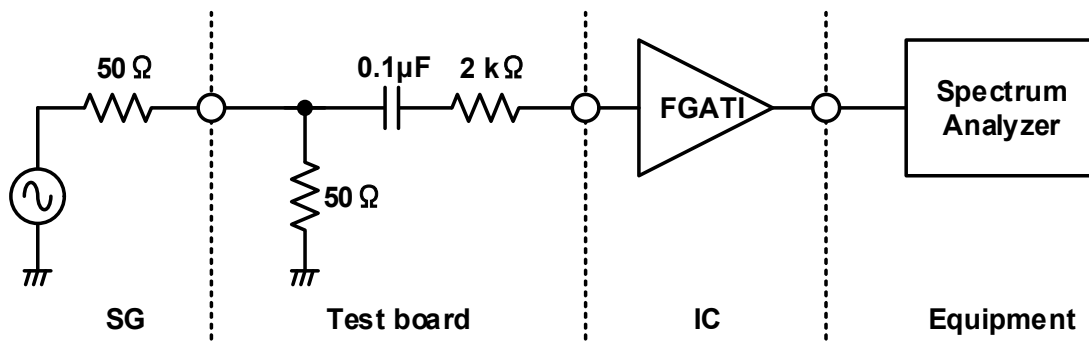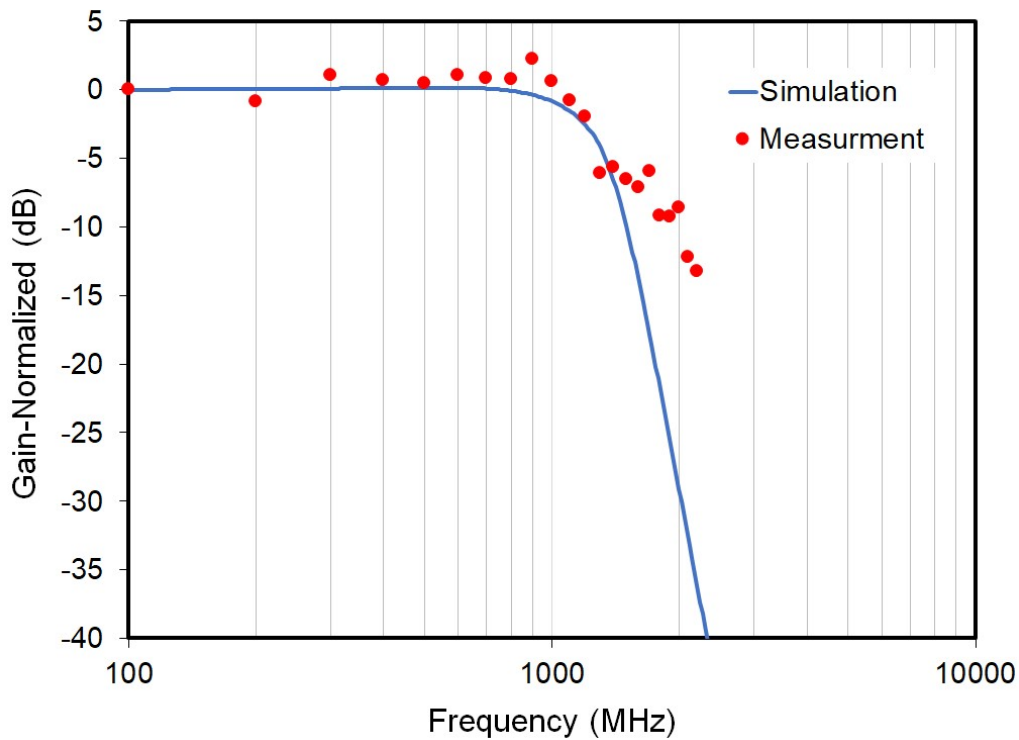The analog output of TIA stage has low amplitude. Therefore, it is required three stages of CS amplifier to make the output observable. However, the CS stages decrease the bandwidth of the FGATI amplifier. Thus, a digital block is added to overcome the problem. The digital block works by adjusting a voltage threshold (V_{th}) value to convert a pair of leading and trailing edge of the TIA analog output signal to a digital signal with a corresponding width by a comparator. The V_{th} of the comparator can be controlled by a Serial Peripheral Interface (SPI) bit line. The V_{th} is ramped up and down by ±2.6 mV for a single step of adjustment. With measuring all of the data point in every level of V_{th}, the analog signal can be reproduce as shown in figure 7-18. The data points resemble the simulation result for both positive and negative signal. It proves the FGATI amplifier is work as designed. Thus, this FGATI amplifier system with the digital block is expected to have better frequency response than 1 GHz which is acquired with the analog block.
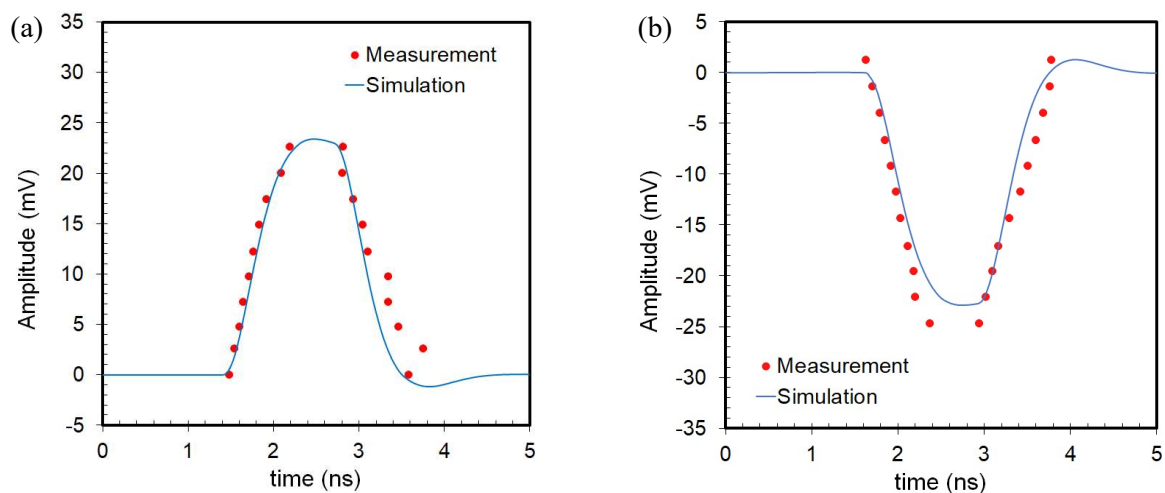
Figure 7-18. The comparison between the simulation result of TIA analog output signal to the reproduction result of the signal by digital block of FGATI amplifier. (a) positive, and (b) negative signal.

The output voltage signals of α-particle under bias voltage between 200 V to 400 V are shown in figure 7-19a. The Full-Width Half Maximum (FWHM) of the signal reasonably reflects the mobility of carriers in the diamond detector [Pom05]. The Charge Collection Efficiency (CCE) of the detector is measured by Charge Sensitive Amplifier (CSA) with a silicon PIN detector

as reference. The measurement result CCE ≈ 96 %. α-particle signal from [241]Am has an energy of 5.486 MeV. By considering the CCE, the generated charge by the α-particle in the diamond detector is around 66 fC. To reproduce the charge, the signal in the fig. 7-19a is divided by transimpedance gain of 79.6 dBΩ shown in figure 7-19b. The estimation of transimpedance gain is close to the value predicted by simulation of 80.3 dBΩ. Therefore, if the output signals are reproduced by simulation, the input signals can be estimated as seen in figure 7-20 by the dashed-lines which are lower than the input signals expected from the experiment due to the higher gain.
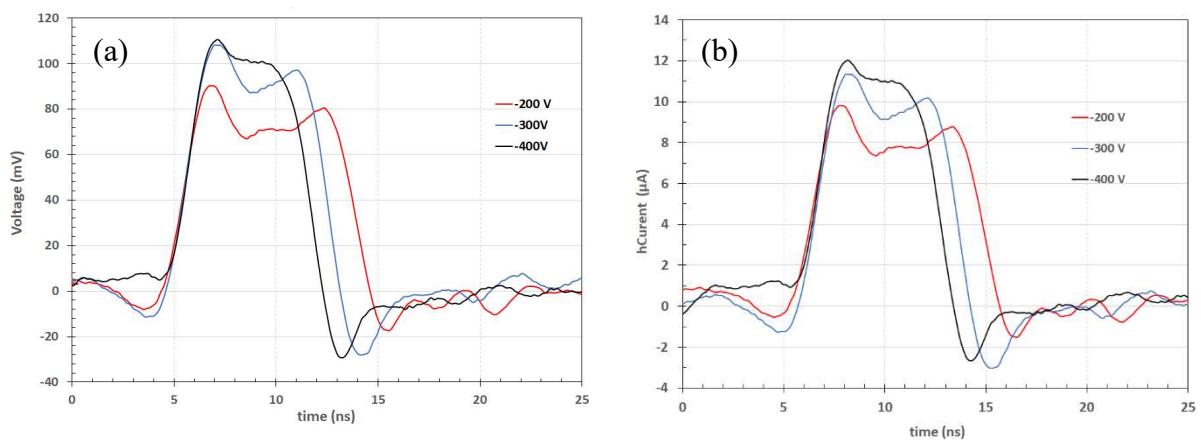
Figure 7-19. α-particle signal measured by TIA (a) Voltage signal. (b) Current signal converted from the voltage signals with a conversion constant of the transimpedance gain of 79.6 dBΩ.
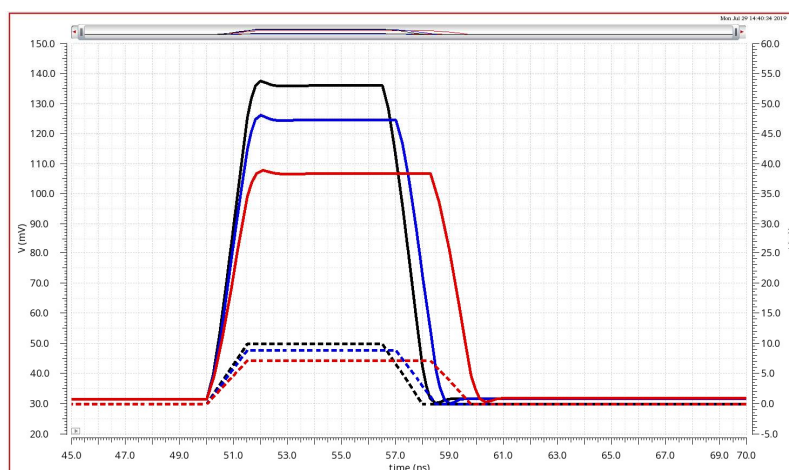
Figure 7-20. The simulation of signal from holes transient current of α-particle in 500 μm diamond. The dashed-line are input signals and the solid-lines are TIA output signals. Red, blue and black line correspond to signal from a diamond detector with bias voltage of 200 V, 300 V and 400 V, respectively.

Table 7-2 TIA Performance Comparison

	[Tag15]	[San15]	[Pon16]	**This Work**
CMOS Technology	130 nm	130 nm	130 nm	**65 nm**
V_{Supply} (V)	1.5	1.3	1.2	**1.2**
R_T (dBΩ)	50.1	60	51	**79.6**
BandWidth (GHz)	7.0	6.9	11.5	**1.0**
DC Power (mW)	7.5	16.9	30	**7.2**
Output Type	Single	Single	Single	**Differential**

The comparison of the performance of the FGATI to other TIA designs is shown in the table 7-2. The FGATI amplifier design with a TSMC 65 nm CMOS technology achieves the lowest power consumption among other recent TIA amplifiers. Therefore, this FGATI amplifier is ideal to be implemented in an application that implements large multichannel detector system which is sensitive to power dissipation such as in the main accelerator facilities.

CONCLUSION

In order to develop a new Diamond detector that can perform carrier amplification effect, a model is applied in TCAD simulation. To construct the model, evaluation of the recent high-quality diamond crystal is conducted. With the sample, the important parameters were extracted from a high-quality diamond MIM detector. The evaluation concludes the detector is a double-Schotty-contact device. The evaluation of gradient of Transient Current signal and generated charge of β-particle give strong evidence that the carrier concentration of the intrinsic diamond has order of $N_A \approx 10^{10}$ /cm^3. The Fast Amplifier has a high Bandwidth (>1 GHz) and it is capable to evaluate the Transient Current Signal of α-particle in diamond detector. Derivation of the transient current drift time conclude the mobility of carrier is 2559 cm^2/V.s (2205 cm^2/V.s) for holes (electrons). The Simulation Model of scCVD diamond that includes the value of Carrier Concentration, Energy Barrier of Metal Contacts, Mobility of Carriers, Lifetime of Carrier can reproduce all experiment data quite well. By using the Model, the feasibility of the new type of diamond detector was evaluated. The detector design can generate High Electric Field to produce charge amplification effect.

The TIA amplifier has low power consumption of 7.2 mW. The power consumption is significantly lower than that of commercially available diamond fast amplifier. The amplifiers have power consumption two order of magnitude higher than TIA. The TIA has wide dynamic range. It performs linear gain to input signal up to ±40 fC. The Spectre simulation shows that TIA is a fast amplifier with a 3-dB bandwidth of 2.7 GHz. The evaluation of TIA evaluation board confirms the TIA has an excellent transimpedance-gain and excellent maximum conversion-gain of 79.6 dBΩ and 8.4 mV/fC, respectively.

APPENDIES

APPENDIX A: Workflow of TCAD Simulation

The workflow of SentaurusTCAD simulation for evaluation of diamond detector is shown in figure A-1. The simulation is divided to three parts. First is Sentaurus Structure Editor (SDE) that requires information about the material used in the simulation and geometry of the device. Second is the first Sentaurus Device (Sdevice) that requires information of evaluation result from the geometry defined in SDE step. The first Sdevice calculate the physical models involved in device simulation by a set mathematical model included in the command file. In this phase, the simulator calculates the value and distribution of all required parameters in a certain bias voltage. The third is simulation of second Sdevice. In this step, simulator conducts a transient simulation as function of time based on value and distribution resulted in the first Sdevice simulation.
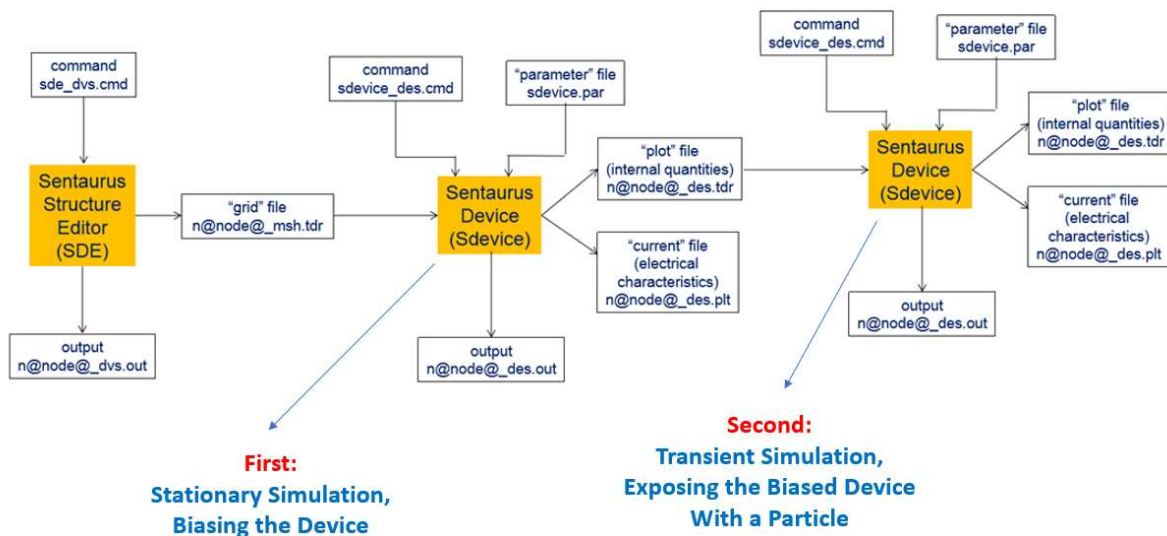

Figure A-1. The workflow of TCAD simulation for evaluating diamond detector

In this work, the comprehensive model of diamond detector is developed and evaluated with the TCAD simulation. A definition of diamond material is added to the simulation due to its absent in Sentaurus TCAD Library. To start the simulation, some prior steps should be completed. Those are:

1. Creating a file that contains required information about additional material. In this case the file name is "diamond.par".

2. Write a detail definition of material, geometry and position of contact of the device in the command file of SDE. The definition of meshes is also included in the command file. By default, the name of the command file is "sde_dvs.cmd".

3. Write all physical and mathematical model that are required for run the stationary simulation in the first Sdevice command file. Beside that, the type of contact and the value of bias voltage also defines in this file. To run the simulation, the physical model written in the command file should be relevant to physical model used by material. Additionally, the parameters that need to be evaluated should be written in plot section. Otherwise the parameters do not show up after the simulation fnish.

4. Write the command file for the second Sdevice. The information written in the second is generally similar with that written in the first Sdevice except, the simulation is a function of time. Therefore, all value related to voltage bias is obtained from the first Sdevice simulation result.

APPENDIX B: Parameter of Diamond Material

Diamond is a new material. Therefore, the parameter of this material is not provided in the Sentaurus TCAD Library. Diamond is defined as a new material by insert a file with a name "diamond.par". The complete characteristics of diamond are defined as follow:

Material = "Diamond" {

Epsilon

{   * Ratio of the permittivities of material and vacuum

         * epsilonO = epsilon

               epsilon = 5.7 # [1]

}

RefractiveIndex

{   * Optical Refractive Index

* refractiveindexO = refractiveindex * (1 + ablpha * (T-Tpar))

      refractiveindex = 2.684 #[1]

      alpha = 4.04e-06 #[1/K]

      Tpar = 3.0000e+02 #[K]

}

KaPpa

{   * Lattice thermal conductivity

      * Formula = 1:

      * kappa() = kappa + kappa_b * T + kappa_c * T^2

      kappa = 20 #[W/(K cm)]

      kappa_b = 0.0000e+00 #[W/(K^2 cm)]

      kappa_c = 0.0000e+00 #[W/(K^3 cm)]

}

Ionization

{

      E_As_0 = 0.1 # [eV]

      alpha_As = 3.1000e-08 #[eV cm]

      g_As =2 #[1]

      Xsec_As = 1.0000e-12 #[cm^2/sec]

      E_P_0 = 0.57 #[eV]

      alpha_P = 0.0000e+00 #[eV cm]

      g_P =2 #[1]

      Xsec_P = 1.0000e-12 # [cm^2/sec]

      E_Sb_0 = 0.1 #[eV]

      alpha_Sb = 3.1000e-08 #[eV cm]

      g_Sb =2 #[1]

      Xsec_Sb = 1.0000e-12 #[cm^2/sec]

E_B_0 = 0.38 #[eV]

alpha_B = 4.7877e-08 #[eV cm]

g_B =4 #[1]

Xsec_B = 1.0000e-12 # [cm^2/sec]

E_In_0 = 0.2 #[eV]

alpha_In = 3.1000e-08 #[eV cm]

g_In =4 # [1]

Xsec_In = 1.0000e-12 # [cm^2/sec]

E_N_0 = 0.1 #[eV]

alpha_N = 3.1000e-08 #[eV cm]

g_N = 2# [1]

Xsec_N = 1.0000e-12 # [cm^2/sec]

E_NDopant_0 = 0.1 #[eV]

alpha_NDopant = 3.1000e-08 #[eV cm]

g_NDopant = 2 #[1]

Xsec_NDopant = 1.0000e-12 # [cm^2/sec]

E_PDopant_0 = 0.2 #[eV]

alpha_PDopant = 3.1000e-08 #[eV cm]

g_PDopant = 4 #[1]

Xsec_PDopant = 1.0000e-12 #[cm^2/sec]

NdCrit = 1.0000e+20 #[cm-3] edited 2016/12/29 A. Morozzi

NaCrit = 3.1000e+19 #[cm-3] edited 2016/12/29 A. Morozzi

}

Bandgap

{ * Eg = Eg0 + dEg0 + alpha Tpar^2 / (beta + Tpar) - alpha T^2 / (beta+T)

* dEg0(<bgn_model_name>) is a band gap cOlTection term. It is llsed together with

* an appropriate BGN model, if this BGN model is chosen in Physics section

* Parameter 'Tpar' specifies the value of lattice

* temperature, at which parameters below are defined

* ChiO is electron affinity.

       Chi0 = 1.3 #[eV]

       Bgn2Chi = 0.5 #[1]

       Eg0 = 5.47 #[eV]

       dEg0(Bennett) = 0.0000e+00 #[eV]

       dEg0(Slotboom) = 0.0000e+00 #[e V]

       dEg0(OldSlotboom) = 0.0000e+00 #[e V]

       dEg0(delAlamo) = 0.0000e+00 #[eV]

       alpha = 0 # [eV K"-l]

       beta = 0.0000e+00 #[K]

       Tpar = 0.0000e+00 #[K]

}

Scharfetter*relation and trap level for SRH recombination:

 {*tau = taumin + (taumax-taumin)/(1 + (NlNref)^gamma)

 tau(T) = tau((T/300)^Talpha) (TempDep)

 *tau(T) = tau*exp(Tcoeff*((T/300)-1)) (ExpTempDep)

       taumin= 0.0000e+00, 0.0000e+00 #[s]

       taumax= 170.0000e-09 , 490.0000e-09 #[s]

       Nref = 1.0000e+16, 1.0000e+16 #[cm^(-3)]

       gamma= 1, 1 #[1]

       Talpha = -1.5000e+00, -1.5000e+00 #[1]

       Tcoeff = 2.55 , 2.55 # [1]

       Etrap = 0.0000e+00 # [eV]

}

OldSlotboom

{ *eltaEg = dEg0 + Ebgn (ln(N/Nref) + [(ln(N/Nref))^2 + 0.5]^1/2)

 *dEgO is defined in BandGap section

    Ebgn = 9.0000e-03 #[eV]

    Nref = 1.0000e+17 #[cm^-3]

}

Slotboom

{ * deltaEg = dEg0 + Ebgn (ln(N/Nref) + [ln(N/Nref))^2 + 0.5]^ 1/2)

 * dEg0 is defined in BandGap section

    Ebgn = 6.9200e-03 #[eV]

    Nref = 1.3000e+17 # [cm^-3]

}

delAlamo

{ * deltaEg = dEg0 + Ebgn ln(N/Nref)

 * dE g0 is defined in BandGap section

    Ebgn = 0.0187 #[eV]

    Nref = 7.0000e+17 #[cm^-3]

}

Bennett

{ * deltaEg = dEg0 + Ebgn (ln(N/Nref))^2

 * dEg0 is defined in BandGap section

    Ebgn = 6.8400e-03 #[eV]

    Nref = 3.1620e+18 # [cm^-3]

}

eDOSMass

{

* For effective mass specificatition Formula 1 (me approximation):

* or Formula2 (Nc300) can be used:

      Formula = 2 #[1]

* Formulal:

* me/m0 = [(6*mt)^2 * ml)1^(1/3) + mm

* mt = a[Eg(0)/Eg(T)]

* Nc(T) = 2(2pi*kB/h_Planck^2*me*T)^3/2 = 2.540e19 ((me/m0)*(T/300))^3/2

      Nc300 =5e+18 #[2]

}

hDOSMass

{

* For effective mass specificatition Formula1 (mh approximation):

* or Formula2 (Nv300) can be used:

      Formula = 2 #[1]

* Formula1 :

* mh = m0*{[(a+bT+cT^2+dT^3+eT^4)/(1+fT+gT^2+hT^3+iT^4))^(2/3) + mm}

* Nv(T) = 2(2pi*kB/h_Planck^2*mh*T)^3/2 = 2.540e19 ((mh/m0)*(T/300))^3/2

      Nv300 = 1.8e+19 #[2]

}

ConstantMobility:

{ * mu_const == mumax (T/T0)^(-Exponent)

      mumax = 2205, 2559 # e, h [cm^2/(Vs)]

      Exponent = 1.55 , 1.55 #[1]

}

DopingDependence:

{

* For doping dependent mobility model three formulas

* can be used. Formula1 is based on Masetti et al. approximation.

* Formula2 uses approximation, suggested by Arora.

      formula = 1 , 1 #[1]

* If formula=1, model suggested by Masetti et al. is used:

* mu_dop = mumin1 exp(-Pc/N) + (mu_const - mumin2)/(1+(N/Cr)^alpha)

*   -mul/(1 +(Cs/N)^beta)

* with mu_const from ConstantMobility

      mumin1 = 0.0000e+00, 105 #[cm^2/Vs]

      mumin2 = 0.0000e+00, 105 #[cm^2/Vs]

      mu1 = 0.0000e+00, 50 #[cm^2/Vs]

      Pc = 0.0000e+00, 0.0000e+00 #[cm^3]

      Cr = 9.9000e+16, 1.0000e+14 #[cm^3]

      Cs = 3.4300e+20, 1.0000e+14 # [cm^3]

      alpha = 0.564 , 0.61 #[1]

      beta = 2, 5.0 #[1]   }

HighFieldDependence:

{ * Caughey-Thomas model:

 * mu_highfield = mu_lowfield/(1+(mu_lowfield E/vsat)^beta)^1/beta

 * beta = beta0 (T/TO)^betaexp.

      beta0 = 1, 1 #[1]

      betaexp = 0.0000e+00, 0.0000e+00 # [1]

      *mu_lowfield = 1.7140e+03, 2.0640e+03

* Smoothing parameter for HydroHighField Caughey-Thomas model:

* if Tl<Tc<(1+K_dT)*Tl, then smoothing between low field mobility

* and HydroHighField mobility is used.

      K_dT = 0.2 , 0.2 #[1]

* TransfelTed-Electron Effect:

* mu_highfield = (mu_lowfield+(vsat/E)*(E/E0_TrEf)^4)/(1 +(E/E0_TrEf)^4)

      E0_TrEf = 4.0000e+03 ,4.0000e+03 #[1]

      Ksmooth_TrEf = 1, 1 # [1]

* For vsat either Formula1 or Formula2 can be used .

    Vsat_Formula = 1 , 1 #[1]

* Formula1 for saturation velocity:

*   vsat = vsat0 (T/T0)^(-Vsatexp)

*(Parameter Vsat_Formula has to be not equal to 2):

    vsat0 = 7.60000e+06, 1.350000e+07 # [1]

    vsatexp = 0.5 , 0.5 # [1]

}

PooleFrenkel

{ * TrapXsection = Xsec0*(1+Gpf)

 * Gpf = (1+(a-1)*exp(a))/a^2-0.5

* where

*   a=(1/kT)*(q^3 *F/pi/e0/epsPF)^0.5,

* F is the electric field.

epsPF = 5.7 , 5.7 # [1]

}

vanOverstraetendeMan * Impact Ionization:

{ * G_impact = alpha_n n v_drift_n + alpha_p p v_drift_p

 * with alpha = gamma a exp(-b gamma/E) for E<EO (low) and E>EO (high)

 * with gamma = tanh(hbarOmega/(2kT0))/tanh(hbarOmega/(2kT))

    a(low) = 1.89e+05, 5.48e+06 #[l/cm]

    a(high) = 1.89e+05, 5.48e+06 #[l/cm]

    b(low) = 1.7e+07 , 1.42e+07 #[V/cm]

    b(high) = 1.7e+07 , 1.42e+07 #[V/cm]

    E0 = 4.0000e+05 , 4.0000e+05 # [V/cm]

    hbarOmega = 1.0000e+03 , 1.0000e+03 # [eV]}

AlphaParticle

```
{
Ep=13
}


HeavyIon
{
s_hi=5.0e-10
}}
```

APPENDIX C: Structure of MIM Diamond Detector
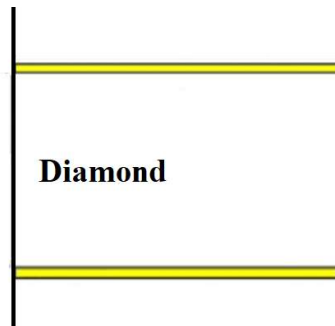
Figure C-1. Two-dimension geometry of diamond detector.

The structure of diamond detector is defined in Sentaurus Structure Editor. The structure is defined in two-dimension as shown in figure B-1. The geometry is written halfway from center as the center of detector shown in vertical thick black line. Due to the symmetry and less computational power, the option to simulation is preferable. The metal contact is simply defined as a line with certain Schottky Barrier value. The detail definition is shown below.

(sde:clear)

```
;**************
; X axis
;**************
(define Xmin 0)


;Sensor
(define RCont            @RCont@)          ; Radius of of upper contact
(define Exc         10)                    ; Excess crystal around contact
(define Xmax   @RSub@)
(define RBCont          (/ RCont 1) )      ; Radius of of back contact



;****************
; Y axis
;****************
(define Ymin    0)


;Sensor
(define tSub    @tSub@)       ; Thickness of the crystal
(define XMIP          @XMIP@)
(define Ymax   tSub)


;****************
; Dose concentration
;****************
(define Dop_PSub      @Dop@)        ;


;=============================================
;***** Contact and Crystal dimension *****
;=============================================
```

92

```
;*** Diamond Crystal ****


(define XPmin Xmin)

(define XPmax Xmax)


(define YPmin Xmin)

(define YPmax tSub)
```

```
;================================================
;**** Drawing structures (Diamond  crystal and the Electrode) ****
;================================================


;-----------------------------------------------
(sdegeo:set-default-boolean "ABA")
;-----------------------------------------------


;=============================
;*** Crystal creation (SUB) ***
;=============================


(sdegeo:create-rectangle (position XPmin YPmin 0) (position XPmax YPmax 0) "Diamond" "PSUB")


;=============================
;*** Contact definitions ***
;=============================
```

```
(sdegeo:define-contact-set "ElectrodeCont" 4.0 (color:rgb 1.0 0.0 0.0) "##")
(sdegeo:define-contact-set "ElectrodeBC" 4.0 (color:rgb 0.0 0.0 1.0) "##")


;*** Upper Electrode ****
(sdegeo:insert-vertex (position Xmin Ymin 0))
(sdegeo:insert-vertex (position RCont Ymin 0))
(define XC (+ Xmin (/ RCont 2)))
(sdegeo:set-current-contact-set "ElectrodeCont")
(define C0 (find-edge-id (position XC Ymin 0)))
(sdegeo:set-contact-edges C0)



;*** Back Electrode ****
(sdegeo:insert-vertex (position Xmin Ymax 0))
(sdegeo:insert-vertex (position RBCont Ymax 0))
(define XB  (+ Xmin (/ RBCont 2)))
(sdegeo:set-current-contact-set "ElectrodeBC")
(define CB (find-edge-id (position XB Ymax 0)))
(sdegeo:set-contact-edges CB)


;============================
;DOPING REGIONS DEFINITIONS
;============================


;*** Crystal: Doping constant ****
(sdepe:doping-constant-placement "Dop_PSub" "BoronActiveConcentration" Dop_PSub
"PSUB")
(sdepe:doping-constant-placement "Dop_Comp" "PhosphorusActiveConcentration"
Dop_Comp "PSUB")


;----------------------------------------------------------------------
```

;Meshing Strategy

;--

(define DXmesh (* 8 factor))

(define DXmesh0 (* 36 factor))

(define DXmesh1 (* 3 factor))

(define DXmesh3 (* 6 factor))

(define DXmesh4 (* 14 factor))

(define DXmesh5 (* 1 factor))

;Meshing Refinament For All Area

(sdedr:define-refeval-window "RFW" "Rectangle" (position Xmin Ymin 0) (position Xmax Ymax 0))

(sdedr:define-refinement-size "RFS" (/ Xmax 100) (/ Ymax 20) (/ Xmax 3000) (/ Ymax 700))

(sdedr:define-refinement-placement "RFP" "RFS" "RFW")

; Meshing Refinement around Contacts

(sdedr:define-refeval-window "RFW_C" "Rectangle" (position Xmin (- Ymin 0.4) 0) (position RCont (+ Ymin 2) 0))

(sdedr:define-multibox-size "RFS_C" 8 8 2 02 0.1 2)

(sdedr:define-multibox-placement "RFP_C" "RFS_C" "RFW_C")

(sdedr:define-refeval-window "RFW_C2" "Rectangle" (position Xmin (- Ymax 2) 0) (position RCont (+ Ymax 0.5) 0))

(sdedr:define-multibox-size "RFS_C2" 10 10 2 1.5 0.1 2)

(sdedr:define-multibox-placement "RFP_C2" "RFS_C2" "RFW_C2")

; MIP at XMIP (denser mesh around position of incoming particle)

(sdedr:define-refeval-window "RFW_MIP0" "Rectangle" (position XMIP Ymin 0) (position (- XMIP DXmesh0) Ymax 0))

(sdedr:define-multibox-size "RFS_MIP0" 5 5 1 1 -2 1)

```
(sdedr:define-multibox-placement "RFP_MIP0" "RFS_MIP0" "RFW_MIP0" )
```

```
(sdedr:define-refeval-window "RFW_MIP1" "Rectangle" (position XMIP Ymin 0) (position (+
XMIP DXmesh0) Ymax 0))
```

```
(sdedr:define-multibox-size "RFS_MIP1" 5 5 1 1  2 1)
```

```
(sdedr:define-multibox-placement "RFP_MIP1" "RFS_MIP1" "RFW_MIP1" )
```

```
; Saving BND file
```

```
(sdeio:save-tdr-bnd (get-body-list) "@tdrboundary/o@")
```

```
;Saving CMD file
```

```
(sdedr:write-cmd-file "@commands/o@")
```

```
;Build Mesh
```

```
(sde:build-mesh "snmesh" " " "n@node@_msh")
```

APPENDIX D: The Physical and Mathematical Model for Sdvice Stationary Simulation

In the simulation, TCAD simulation provides multiple physical model to be applied in a device. The TCAD simulation also gives option for mathematical model to calculate the physics formula. The selected physical and mathematical model needs to be written in command file of Sdevice as shown below:

```
File {
        grid    = "@tdr@"
        Output = "@log@"
        parameter = "Diamond.par"
```

```
        plot    = "@tdrdat@"

        current = "@plot@"

}


Electrode {

{name = "ElectrodeCont"        voltage = 0.0 Schottky Barrier=4.35}

{name = "ElectrodeBC"          voltage = 0.0 Schottky Barrier=4.35}

}




Physics {

        Mobility(        -ConstantMobility

                        DopingDependenc

                        HighFieldSaturation(Eparallel)

                        Enormal

         )


        Recombination(        SRH(DopingDependence)

                        Avalanche

         )


        EffectiveIntrinsicDensity( OldSlotboom )

        Temperature=298

        Hydrodynamic

        }


Plot {

        Current/Vector

        eCurrent/Vector

        hCurrent

        eDensity
```

```
        hDensity

        ElectricField/Vector

        Potential

        DopingConcentration

        SpaceCharge

        srhRecombination

        AvalancheGeneration

        TotalRecombination

        eMobility

        hMobility

        ValenceBandEnergy

        ConductionBandEnergy

}


Math {

        NumberOfThreads = maximum      *use all cpu available

        Digits = 5                     *accuracy of solution

        Iterations = 20                *max iteration

        RelErrControl                  *more physically meaningful error parameter

        Method=Pardiso

        Stacksize = 200000000

        Extrapolate

        Derivatives

        AvalDerivatives

        Notdamped=100

        Cylindrical


    BreakCriteria {

      Current (Contact = "ElectrodeCont" maxval = 1e-10)

      Current (Contact = "ElectrodeBC" maxval = 1e-10)

            }
```

```
        NoAutomaticCircuitContact

        ExtendedPrecision(80)

}


Solve {

        Poisson

        Coupled(Iterations= 100 LineSearchDamping= 1e-4)

        { Poisson }

        Coupled {Poisson}

        Coupled {Hole Poisson}

        Coupled {Electron Hole Poisson}


 QuasiStationary (

        InitialStep = 1e-5

        MaxStep = 0.025

        MinStep = 1e-6

        Goal { Name= "ElectrodeCont" Voltage=@Vop@}


        Plot { Range=(0 1) Intervals=1 }

        ) { Coupled { Hole Electron Poisson Circuit} }

        Save (FilePrefix = "IV_@Vop@_@tSub@_@RCont@")

}
```

APPENDIX E: The Physical and Mathematical Model for Sdevice Transient Simulation

Similar to the command file for stationary simulation, the command file in a transient simulation also contains the mathematical and physical model. The difference is the calculation is a function of time. The command file for transient Sdevice is shown below:

```
Electrode {

        {name = "ElectrodeCont"          voltage = 0.0 Schottky Barrier=4.35}

        {name = "ElectrodeBC"            voltage = 0.0  Schottky Barrier=4.35}


}


File {

        Grid   =  "@tdr@"

        Parameter = "Diamond.par"

        Parameter = "NewSRHRecombination.par"

        Current =   "alp_des_@XMIP@.plt"

        plot   =  "alp_des_@XMIP@.tdr"

        Output  =  "alp_des_@XMIP@.log"

        }


Physics {

        Mobility(        -ConstantMobility

                          DopingDependence

                          HighFieldSaturation(Eparallel)

                          Enormal

                      )


        Recombination(  SRH(DopingDependence)

                          Avalanche

                )


        EffectiveIntrinsicDensity( OldSlotboom )
```

********************* Definition of Alpha Particle -start-*********************

        HeavyIon (

                Direction=(0, -1)

                Location=(@XMIP@, 500.0)

                Time= 2.0e-9

                Length = [0   500]

                LET_f = [57.67e-7 57.67e-7]

                Wt_hi = [1.0   1.0   ]

                Picocoulumb)

********************* Definition of Alpha Particle -endt-*********************

        Temperature=298

        Hydrodynamic

}

Plot {

        totalCurrent/Vector

        hCurrent/Vector

        eCurrent/Vector

        hCurrent

        eDensity

        hDensity

        ElectricField/Vector

        Potential

        Doping

        DonorConcentration

        AcceptorConcentration

        SpaceCharge

        srhRecombination

        AugerRecombination

```
			AvalancheGeneration

			TotalRecombination

			eMobility

			hMobility

			HeavyIonChargeDensity

			HeavyIonGeneration

	}


Math {

			Digits=7

			Iterations=1000

			Method=Pardiso

			Number_of_threads = 4

			Stacksize = 200000000

			Extrapolate

			Derivatives

			RelErrControl

			Avalderivatives

			RecBoxIntegr(1e-4 100 10000)

			Transient=BE

			Cylindrical

	}


Solve {

	Load(FilePrefix="IV_@Vop@_@tSub@_@RCont@")
	NewCurrentPrefix="transient_IV_@Vop@_@tSub@_@RCont@"



	Transient (

			InitialTime = -1.0e-10
```

FinalTime = 2.1e-8

InitialStep = 5e-15

MaxStep = 3e-11

MinStep = 1e-17

Increment =1.2

)

{ Coupled (iterations=8, notdamped=15) {Poisson Electron Hole}

 Plot (FilePrefix="Trans_IV_@Vop@_@tSub@_@RCont@_1_" Time= (1e-10; 1e-9; 1.5e-9; 2.0e-9; 2.5e-9; 3.0e-9; 3.5e-9; 4.0e-9; 4.5e-9; 5.0e-9; 6.0e-9; 7.0e-9; 8e-9; 9.0e-9; 10e-9; 12.0e-9; 14.0e-9; 16.0e-9; 18.0e-9; 20.0e-9; 25.0e-9; 30.0e-9; 50.0e-9) NoOverwrite)

}}

REFERENCES

[Aki16] Y. Akimoto *et al.*, *Nucl. Instrum. Meth. A* 557, 2006.

[Art13] M. Artuso *et al.*, Planning Study: Snowmass 2013.

[Bec10] J. Becker. Universität Hamburg. Dissertation 2010.

[Bre07] M. Brezeanu *et al.*, *IET Circuits Devices Syst.*, 2007.

[Bre07-2] M. Brezeanu. Cambridge University. Dissertation 2007.

[Bru07] M. Bruzzi *et al.*, *Nucl. Instrum. Meth. A* 579 (2007).

[Cau67] D. Caughey *et al.*, *Proceedings of the IEEE* 55, 12, 1967.

[Chy58] A. G. Chynoweth. *Phys. Rev.* 109, 1537, 1958.

[Eva09] D. A. Evans *et al.*, *J. Phys. Condens. Matter* 21, 2009.

[Gab08] M. Gabrysch *et al.*, *Phys. stat. sol. (a)* 205, 9, 2008.

[Gab10] M. Gabrysch. Uppsala University. Dissertation 2010.

[Isb02] J. Isberg *et al.*, Vol. 297 *Science*, 2002.

[Isb06] J Isberg *et al., Semicond. Sci. Technol.* 21 2006.

[Har18] A. Hara. Master thesis SOKENDAI, Japan 2018.

[Hat99] A. Hatta *et al.*, *Diam. Relat. Mater.* 8, 1470, 1999.

[Kas16] F. Kassel *et al.*, *Phys. Status Solidi A* 213, 10, 2016.

[Kas17] F. Kassel. Karlsruhe Institute of Technology. Dissertation 2017.

[Kno93] G. F. Knoll and D. S. McGregor. *Proc. Material Research Society* 1993

[Kno00] G. F. Knoll. Wiley. 2000.

[Lan93] M. I. Landstrass *et al.*, *Diamond Relat. Mater.* 2, 1033, 1993.

[Liu09] F. B. Liu *et al.*, *Chinese Phys. B* 18, 2041, 2009.

[Lut10] G. Lutz *et al.*, *Nucl. Instrum. Meth. A* 624, 2010.

[Mar14] A. Maréchal *et al.*, *Diam. Relat. Mater.* 43, 2014.

[Mas83] G. Masetti *et al.*, *IEEE Trans. Electron. Devices*, ED-30 (7), 764, 1983.

[Mck54] K. G. McKay. *Phys. Rev.* 94, 877, 1954.

[Mor16] A. Morozzi *et al.*, Proc.18th IWORID 2016.

[Mos05] F. Moscatelli *et al.*, *Nucl. Instrum. Meth. A* 546, 2005.

[Mus17] M. Muškinja *et al.*, *Nucl. Instrum. Meth. A* 841, 2017.

[Nav08] F Nava *et al.*, *Meas. Sci. Technol.* 19, 2008.

[Naw13] A. Nawawi *et al.*, *Diam. Relat. Mater.* 35, 2013.

[Neb06] C. E. Nebel *et al.*, phys. stat. sol. (a) 203, 2006.

[Nes08] M. Nesladek *et al.*, *Diam. Relat. Mater.* 17, 2008.

[Oh13] A. Oh *et al.*, *Diam. Relat. Mater.* 38, 2013.

[Per05] H. Pernegger e*t al.*, *J. Appl. Phys.* 97, 073704, 2005

[Per10] J. Pernot *et al.*, *Phys. Rev. B* 81, 2010.

[Pom05] M. Pomorski *et al.*, *phys. stat. sol*. (a) 202, 11, 2005.

[Pom08] M. Pomorski. Johann Wolfgang Goethe Universitat. Dissertation 2008.

[Pon16] A. F. Ponchet e*t al.*, *Proc. SBCCI-IEEE*, 2016.

[Ram39] S. Ramo. *Proc. IRE*. 27 (9)1939

[Ras06] S.J. Rashid *et al.*, *Diam. Relat. Mater.* 15, 2006.

[Ras08] S. J. Rashid. *IEEE T. Electron Dev.* 55, 10, 2008.

[San15] J. Sangirov *et al.*, *Comput. Electron.* 14, 3, 2015.

[Shi18] T. Shimaoka *et al.*, *Appl. Phys. Lett.* 113, 093504, 2018.

[Sku16] N. Skukan *et al.*, *Appl. Phys. Lett.* 109, 043502, 2016.

[Sze07] S. M. Sze and K. N. Kwok. John Wiley & Sons 2007

[Tac92] T. Tachibana *et al.*, *Phys. Rev. B* 45, 20, 1992

[Tag15] M. H. Taghavi *et al.*, *IEEE T. Circuits- I* 62, 8, 2015.

[Tan06] Y. Tang *et al.*, *Diam. Relat. Mater.* 15, 2006.

[Ter06] T. Teraji *et al.*, *Diam. Relat. Mater*. 15, 602, 2006.

[Tsu16] N. Tsubouchi, Y. Mokuno. *J. Cryst. Growth* 455, 2016.

[Vel08] J.J. Velthuis *et al.*, *Nucl. Instrum. Meth. A* 591, 2008.

[Wan00] Y. Wang *et al.*, *Surf. Interface Anal.* 29, 2000.

[Wan05] Y. Wang and R. Raut. *IEEE* 2005

[Wil04] O. A. Williams and R. A. Jackman, *Diam. Relat. Mater.* 13, 166, 2004.

[Wor08] Chris J. H. Wort and Richard S. Balmer. *Materialstoday* 1-2, 11, 2008.

[Zey06] S. Zeyrek et al. *Appl. Surf. Sci.* 252, 2006.

[Asn] D.M. Asner (PNNL), E. Dart (ESnet), T. Hara (KEK). Belle II Experiment Network and Computing excerpts from Belle II. Experiment Network Requirements Workshop Report.

[Ben] Mathieu Benoit. Simulation of Silicon detectors using TCAD and Monte-Carlo methods. Universite de Geneve.

[Civi] https://cividec.at/electronics-C2-TCT.html.

[El6] The ElementSix CVD Diamond Handbook 2019.
https://e6cvd.com/media/wysiwyg/pdf/E6_CVD_Diamond_Handbook_A5_v10X.pdf .

[Mas] Konstantinos Masselos. Basic MOS Theory, SPICE Simulation, CMOS Fabrication. Department of Electrical & Electronic Engineering, Imperial College London.

[Mini] https://ww3.minicircuits.com/pdfs/GALI-52+.pdf.

[Mor] A. Morozzi and D. Passeri. Numerical Modelling of sCVD and pCVD Diamond with Sentaurus TCAD Tools. Presentation.

[Naj12]   F. Najmabadi. Differential Amplifiers ECE 102, Fall 2012,